The Dissertation Committee for Seungbum Koo
certifies that this is the approved version of the following dissertation:

Subsurface elastic wave energy focusing based on a time reversal concept

Committee:

Loukas F. Kallivokas, Supervisor

Leszek F. Demkowicz

Sergey B. Fomel

Omar Ghattas

Kenneth H. Stokoe II

John L. Tassoulas

Subsurface elastic wave energy focusing based on a time reversal concept

by

Seungbum Koo, B.S.; M.S.C.ENVIRON.E.

DISSERTATION

Presented to the Faculty of the Graduate School of

The University of Texas at Austin

in Partial Fulfillment

of the Requirements

for the Degree of

DOCTOR OF PHILOSOPHY

THE UNIVERSITY OF TEXAS AT AUSTIN

May 2017

전문가는 자신이 무엇을 모르는지 아는 사람이다.

Experts are people who know what they do not know.

Acknowledgments

I wish to thank the multitude of people who helped me throughout my doctoral study. My supervisor, professor Loukas F. Kallivokas, has provided me an excellent support and guidance to my research, and also showed an endless patience to my slow progress. I would not be able to mark the final period in this dissertation without his support and insightful suggestions as well as valuable discussions which cannot be altered by anything else. Professor Demkowicz trained me hard through his teaching, and I am proud to announce that I survived in his jungle and received A, although he always asks me who I am when I visit his office for some favors and advice. Professor Fomel gave me a chance to expose myself to the people in the industry and lent me an opportunity to introduce my research to those people by allowing me to present in the Texas Consortium for Computational Seismology's biannual meeting. I would like to convey my deepest gratitude to him. I also want to deliver acknowledgment to professors Ghattas, Stokoe, and Tassoulas for serving as my dissertation committee members. Their invaluable suggestions during my comprehensive examination (proposal presentation) strengthened the grounds of my research and reinforced my dissertation.

A part of the financial support was provided by an Academic Alliance Excellence grant between the King Abdullah University of Science and Tech-

nology in Saudi Arabia and the University of Texas at Austin. This support is gratefully acknowledged.

I want to thank my former and current office mates, Dr. Chanseok Jeong, Dr. Arash Fathi, Dr. Pranav Karve, Dr. Babak Poursartip, Hamidreza Mashayekh, Heedong Goh, Dr. Jinkyoo Park, and Dr. Jae Sang Moon for the joyful office life, fruitful discussions, and whining.

There are also friends who shared the time with me at the outside of research and study. My life in Austin has been fun and enjoyable because of these people. Dr. Seonpil Jang, Dongkeun Lee, Jongkwon Choi, Dr. Changhyuk Kim, Dr. Ki Yeon Kwon, Dr. Jinhan Kwon, Boram Lim, Kwangjin Lee, Hajeung Oh, Dr. Jung Su Lee, Dr. Sungyeob Shin, Namho Kim and with many others, I could fill my years in Austin with pleasant memories.

The heartiest thank goes to my family, who has been an essential and indispensable source of love and support. My wife, Eun Deok, this dissertation is dedicated to you, as you have always stood by me. I offer my regards to all of those who supported me in any respect during the completion of my Ph.D. degree.

Subsurface elastic wave energy focusing based on a time reversal concept

Seungbum Koo, Ph.D.
The University of Texas at Austin, 2017

Supervisor: Loukas F. Kallivokas

In the context of wave propagation, time-reversal refers to the invariance of the wave equation when the direction of traversing the time line is reversed. To date, there have been several applications rooted in the time-reversal concept, primarily in acoustics and in electromagnetics, and in settings that typically involve closed, finite, domains. In recent times, the concept has been predominantly used for steering and focusing wave energy in medical therapeutics.

The extension of the time-reversal concept to elastodynamics, particularly in unbounded domains, entails challenges: the presence of two velocities and two body wave types, the presence of surface waves, the unboundness of the host domain, and aperture constraints, all conspire to limit or weaken wave focusing. This dissertation concentrates on a computational study for assessing

the feasibility of focusing elastic waves to one or multiple subsurface targets, based on the time-reversal concept. Of particular interest is the focusing of wave energy to subterranean geologic formations, embedded within heterogeneous hosts. The motivation stems from potential applications to wave-based enhanced oil recovery, though other applications also stand to benefit.

We report on a study that systematically assesses each and every limitation that is present when a small number of surface motion records are time-reversed and broadcast back into a heterogenous halfspace, aimed at the illumination of subsurface targets. We report the results of numerical experiments in two and three dimensions, and the impact of the limitations on the focusing resolution. All in all, despite the difficulties imposed by the physical setting, we conclude that focusing of elastic wave energy is feasible and competitive when compared against inverse source methods with similar targeting or focusing goals.

Table of Contents

List of Tables

List of Figures

Chapter 1

Introduction

1.1 On wave focusing

Stimulation of a target embedded in an arbitrarily heterogeneous medium by focusing wave energy to it can be a potent, non-invasive, recourse for bringing about desired changes in the mechanical behavior of the target. Key applications of wave stimulation include collapse of underground cavities/tunnels/mines/sink holes, wave-based enhanced oil recovery (EOR), controlled/forced detonation of unexploded ordnances, removal of contaminant particles from aquifers or from the pores/interstices of geological formations, and others. Medical therapeutic applications are also among notable applications of wave focusing: for example, lithotripsy (breaking of kidney stones) has been the archetypical application of wave focusing in medical applications, and similarly motivating applications concentrate on cancer treatment.

The typical – and most-researched to date – setting of wave focusing involves a target embedded in a closed cavity or finite domain occupied by an acoustic fluid. The target is surrounded by receivers/emitters that can record a signal originating from the target (Fig. 1.1a), and the emitters can redirect/focus energy to the target (Fig. 1.1b). By contrast, here we are inter-

ested in elastic wave focusing on targets embedded within the subsurface, i.e., hosted by a semi-infinite heterogeneous domain, without the benefit of having the target surrounded with receivers and emitters.

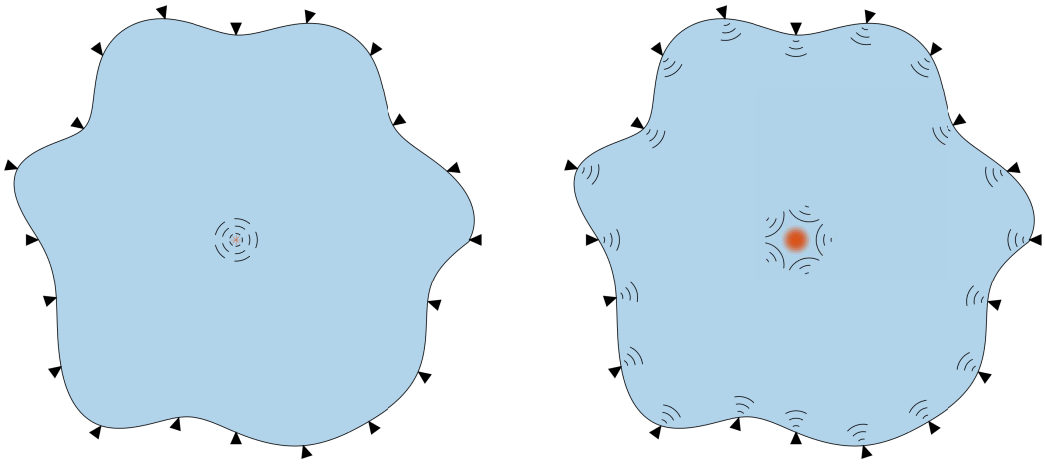

(a) A source surrounded by a receiver/emitter array on the boundary of a closed cavity - the source emits waves - the receivers record

(b) The emitters on the boundary of the closed cavity broadcast the time-reversed recordings - the emitted waves refocus on the target/source

Figure 1.1: Time-reversal conceptual setting

The application is motivated by EOR needs: there is interest in facilitating the mobility of oil ganglia in reservoir subregions typically bypassed by primary modes of recovery, especially in low permeability zones. The central hypothesis is that focusing wave energy to a target zone may induce sufficiently large matrix accelerations to overcome the capillary forces holding the ganglia in the pore space, thus setting the stage for conventional oil extraction methods to sweep the thus mobilized ganglia. Laboratory studies [9], field applications [10, 51], and numerical studies [29–32, 34, 35, 37, 50] support the

hypothesis.

Though motivated by EOR needs, the applicability of elastic wave time-reversal is wider, from health monitoring to geophysical probing and to military applications, including chorochronic event localization: not only can the time-reversal concept be used to focus energy, but it could also be used to identify the onset of a crack or of a seismic fault rupture, both in space and time.

The discussion of the methodology presented herein seeks to identify the factors that contribute to the loss or worsening of focusing resolution owing to many physical constraints that force the less-than-ideal implementation of the time-reversal concept in practice. The approach draws, wherever possible, from theoretical results, but, for the most part, rests on computational evidence.

1.2 The time-reversal method - background

To set the stage for the utility of the time-reversal concept, we discuss first a motivating application (EOR), where there is need to focus wave energy at a specific subterranean target. The target is typically an inclusion of rather limited and finite extent compared to its surroundings (Fig. 1.1a). To focus elastic wave energy to the target, sources capable of initiating stress waves are used, placed either on the surface or at depth. Surface sources capable of delivering elastic waves to the target include Vibroseis trucks (Fig. 1.2), whereas at-depth sources include wellbore hydraulic pumps, or other electromechanically activated loads. The waves generated by any single one of these sources are typically omni-directional. The waves, as they travel through the medium

Figure 1.2: A typical Vibroseis truck

hosting the target, will lose energy due to three principal forms of attenuation: due to radiation damping because of expanding geometric fronts, due to intrinsic attenuation or material damping because of internal friction, and due to apparent attenuation because of scattering at grain or other material interfaces. Since there is no practical way of reducing or controlling the aforementioned sources of energy loss, focusing wave energy on a target requires that multiple sources are used, and, in fact, that they operate synergistically to, ideally, maximize the energy delivery to the target. In short, when operating multiple sources, conditions of constructive interference must be created at the target. To design a scheme that would allow all the waveform crests to arrive at the target synchronously is fairly challenging even in the case of a homogeneous host, let alone in the case of an arbitrarily heterogeneous host, which is the typical setting in our application.

We are, thus, interested in devising a methodology that would, somehow, allow for the systematic illumination of the target, irrespective of the host's complexity and of the number of available sources. One such possible

path is offered by a partial-differential-constrained optimization methodology [31–34]: accordingly, one can define a functional describing the sought outcome at the target (e.g., maximization of fluid pressure, or of kinetic energy, or of a pressure gradient, etc), and treat the source signals (or even their locations in space) as design parameters, which, upon convergence, would lead to wave sources that would have the desired effect on the target. In other words, one seeks to optimize the sources, with a particular outcome in mind, subject to the underlying physics of the problem at hand: this is the very setting of an *inverse source* problem [31–34]. As an inverse problem, its resolution is plagued by the usual difficulties associated with all inverse problems, including solution multiplicity and ill-conditioning. But, more importantly, the solution of the inverse source problem requires that the properties of the host and of the target be known *a priori*. In fact, the quality of the focusing is only as good as the information of the material properties of the host and the target [35], or, said differently, the focusing resolution depends on the certainty by which the properties are known. In well-characterized subsurface formations, the properties may be *a priori* known with reasonable certainty, but never accurately, whereas in most other situations, the properties must be estimated prior to seeking to optimize the wave sources for purposes of focusing energy to a target. The property estimation calls, in effect, for resolution of another inverse problem, this time of an inverse medium problem. Thus, the source optimizer route, though feasible, depends greatly on knowing the properties, which is, in general, hindered by physical realities.

Given the difficulty with the material properties when an inverse-source approach is used for focusing, it is of practical interest to explore alternatives that do not rely on the *a priori* knowledge of the material distribution. Such an alternate route to focusing, and indeed the path followed herein, is based on the exploitation of the time-reversal (TR) concept.

It is the objective of this dissertation to provide evidence of the ability of the time-reversal method to focus wave energy to one, or multiple, subsurface targets, in the context of elastic wave physics, and especially when the host medium is heterogeneous and semi-infinite in extent.

The time-reversal idea rests on the invariance of the wave equation with respect to time. We illustrate, using the acoustic wave equation as an example:

$$\frac{\partial^2 u}{\partial t^2}(\mathbf{x},t) - c^2 \Delta u(\mathbf{x},t) = f(\mathbf{x},t), \quad \mathbf{x} \in \Omega, \quad 0 < t \leqslant T \tag{1.1}$$

where $u(\mathbf{x},t)$ is the acoustic pressure field, c is the (constant) wave speed of the acoustic fluid, and Ω is the domain occupied by the acoustic fluid. If t in (1.1) is replaced by $\tau = T - t$, the equation reads:

$$\frac{\partial^2 u}{\partial \tau^2}(\mathbf{x},\tau) - c^2 \Delta u(\mathbf{x},\tau) = f(\mathbf{x},\tau), \quad \mathbf{x} \in \Omega, \quad 0 < \tau \leqslant T. \tag{1.2}$$

Though (1.2) appears identical to (1.1), the variable change has forced the backwards traversal of the timeline, i.e., from $\tau = T(t = 0)$ to $\tau = 0(t = T)$. All applications of the TR concept stem from the above observation. For example: let us assume that a source broadcasts a finite-duration signal, which is then recorded at a set of receivers, and then the receivers rebroadcast the recorded

signals, albeit backwards played. Then, loosely stated[1], the rebroadcast signals will converge to the original source point. A similar phenomenon, referred to as reciprocal time-reversal, arises when the rebroadcast signals are played back from the source point, in which case, owing to the receiver-source reciprocity, the broadcast signal will refocus on the receiver.

The first reported experiments on time-reversal are probably due to Parvulescu and Clay, and were conducted at Columbia University in the early 1960s. The first field experiment was conducted in 1965 in the Tongue of Ocean, also by Parvulescu and Clay [45]; strictly speaking, it was a reciprocal time-reversal experiment, rather than a "straight" time-reversal experiment.

Recent advances in acoustic time-reversal can be found in a series of articles by Fink and his collaborators, starting from the early 1990s [13, 24, 26, 56]. In these articles, the authors developed and proved the validity of the time-reversal concept for closed cavities, both theoretically and experimentally and in the presence of heterogeneity, by using a time-reversal mirror (TRM), i.e., an array of acoustic transducers that surrounds the closed cavity and can record and broadcast acoustic pressure signals.

As described, the application of the time-reversal concept requires two distinct steps in order to guide waves to the target: the forward step and the TR step. During the forward step, a source (or sources) is placed at the target location. The source emits a signal into the domain (Fig. 1.3.) An array

[1]The lack of rigor in this statement is due to considerations regarding the number of receivers, the boundary conditions, etc.

of receivers (the time-reversal mirror, TRM) is deployed on either the entire boundary of Ω or on part of it. The TRM receivers record the waveforms due to the source's emission. During the TR step, the recorded signals are time-reversed, and broadcast back into the domain. The rebroadcast waveforms will focus at the source location. The forward and TR steps are governed by the

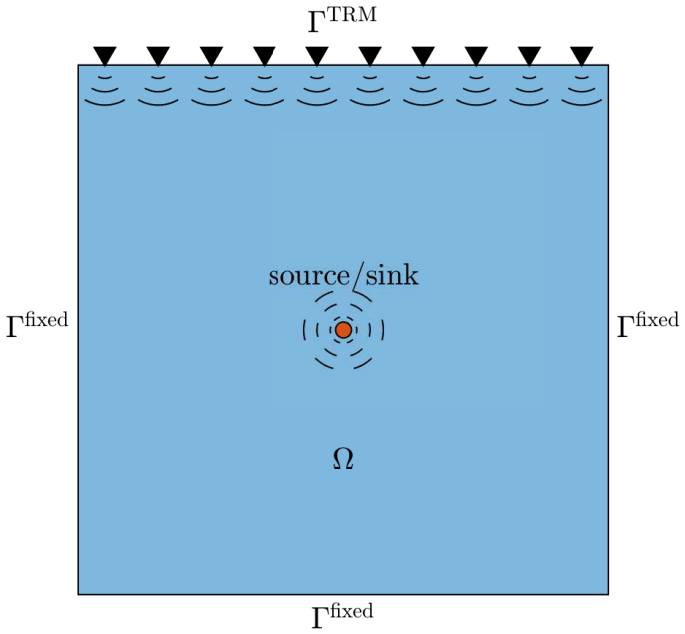

Figure 1.3: A closed cavity problem in elastodynamics; the source emits signals that are subsequently recorded at the TR mirror

wave equation, (1.1) and (1.2), respectively. The differences in the solution stem from the treatment of the source, of the initial, and of the boundary conditions. We review next the two steps, in the context of the closed cavity problem.

Forward step: In the forward step, a source is placed at the target location within the domain. The domain is initially at rest. The TRM is installed on part of the boundary, shown as Γ^{TRM} in Fig. 1.3; the rest of the boundary Γ^{fixed} is fixed (sound-soft condition with vanishing pressure). Accordingly:

$$u(\mathbf{x}, t) = 0, \quad \mathbf{x} \in \Gamma^{\text{fixed}} \tag{1.3a}$$

$$\frac{\partial u}{\partial n}(\mathbf{x}, t) = 0, \quad \mathbf{x} \in \Gamma^{\text{TRM}} \tag{1.3b}$$

$$u(\mathbf{x}, 0) = 0, \quad \mathbf{x} \in \Omega \tag{1.3c}$$

$$\dot{u}(\mathbf{x}, 0) = 0, \quad \mathbf{x} \in \Omega \tag{1.3d}$$

where $\mathbf{n}$ is the outward normal on the boundary. The source is triggered, and the receiver array records the signals that reach the TRM for up to a T total duration.

TR step: Once the recording at the TRM has completed, the recorded $u(\mathbf{x}, t)$ at the TRM ($\mathbf{x} \in \Gamma^{\text{TRM}}$) is first reversed in time. Next, the TRM acts as an array of sources injecting the time-reversed signals $u(\mathbf{x}, T - t)$, $\mathbf{x} \in \Gamma^{\text{TRM}}$, back into the domain. We remark that the boundary where the TRM is installed acts as a sound-hard surface (zero pressure gradient) during the forward step, and as a sound-soft surface during the TR step. We also require that the pressure vanishes on Γ^{fixed} during both steps.

Let us denote the pressure wavefield generated during the TR step as $v(\mathbf{x}, t)$. Then, the governing equation becomes:

$$\frac{\partial^2 v}{\partial t^2}(\mathbf{x}, t) - c^2 \Delta v(\mathbf{x}, t) = f(\mathbf{x}, T - t) \tag{1.4}$$

subject to the following initial and boundary conditions:

$$v(\mathbf{x},t) = \quad 0, \qquad\qquad \mathbf{x} \in \Gamma^{\text{fixed}} \tag{1.5a}$$

$$v(\mathbf{x},t) = \quad u(\mathbf{x},T-t), \quad \mathbf{x} \in \Gamma^{\text{TRM}} \tag{1.5b}$$

$$v(\mathbf{x},0) = \quad u(\mathbf{x},T), \qquad \mathbf{x} \in \Omega \tag{1.5c}$$

$$\dot{v}(\mathbf{x},0) = -\dot{u}(\mathbf{x},T), \qquad \mathbf{x} \in \Omega. \tag{1.5d}$$

Notice that the initial conditions of the TR step are, in effect, the final conditions of the forward step, owing to the reversal of the timeline. Moreover, notice that in (1.4) the source has also been time-reversed; henceforth, we will be referring to the time-reversed source as a *sink*. We remark that the TRM has not recorded the evanescent wavefield that is local to the source, since such a field does not propagate to the TRM. The sink, in effect, accounts for the lack of the evanescent information in the time-reversed TRM signals.

For the time-reversal to be perfect, one needs to solve equation (1.4) with the initial and boundary conditions (1.5). Figure 1.4 depicts snapshots of the pressure field u at various instances during the forward step for the prototype closed cavity shown in Fig. 1.3. Here, the total duration is $T = 1.3$s in steps of 0.005s; the wave speed c is 70.7107 m/s, and the cavity is a square 50 m $\times$ 50 m. Similarly, Fig. 1.5 shows snapshots of the time-reversed pressure wavefield v. We note the perfect refocusing at the source location; notice also the forward and reversed wavefield similarities.

We further remark that this simulation is an ideal implementation of the acoustic time-reversal method, where the TRM covers the entire Γ^{TRM},

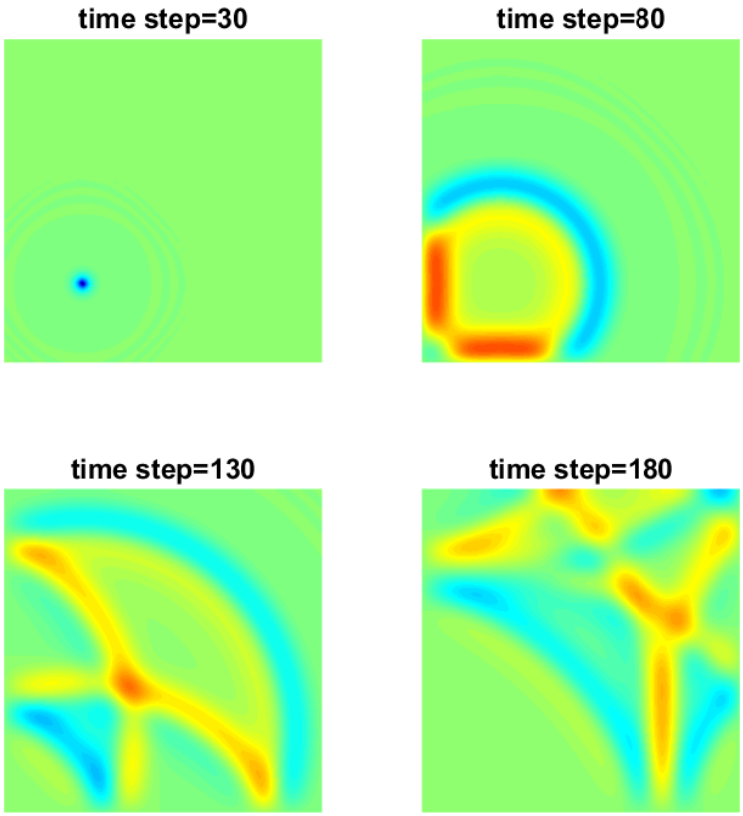

Figure 1.4: Snapshots of the pressure wavefield u during the forward step

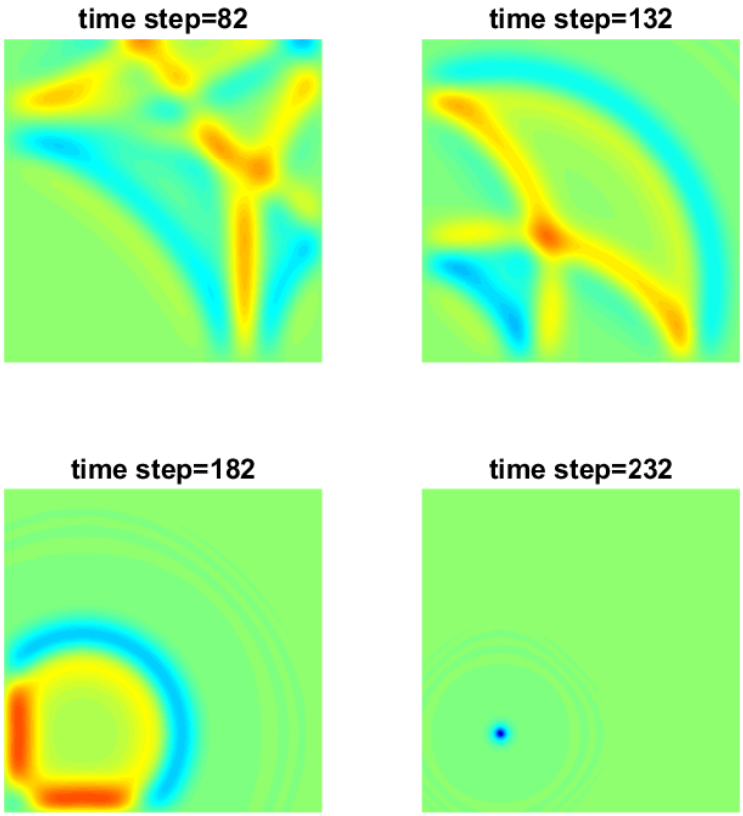

Figure 1.5: Snapshots of the pressure wavefield v during the time-reversal step

and the initial conditions (1.5c) and (1.5d) for the time-reversal step are also assumed to be known for the entire domain. These *ideal* conditions, are hard or impossible to achieve in practice, and any departure from these conditions will affect the quality of the focusing.

Remarks

1. We note that the heterogeneity of the medium does not hinder, but rather enhances the quality of the refocus due to the elongation of the wave path caused by steering and reflection [56]. If one records the waves arriving at the TRM for a sufficiently long time, then the recorded waveforms would carry rich information about the medium's heterogeneity owing to multiple reflections off of the medium's material interfaces. In such cases, the quality of the refocus is enhanced [2, 56]. This phenomenon is often referred to as super resolution [2, 17]. Thus, one can view the time-reversal method as a self-adaptive method that accounts for the heterogeneity of the medium [14, 24, 25].

2. The TRM does not necessarily have to occupy the boundary completely, as it can also be seen from the simulation depicted in Figs. 1.4 and 1.5. If a domain is closed, waves generated from the domain sources will reside inside the domain and ultimately will be captured by the TRM due to multiple scattering and reflection even though the TRM is only partially covering the boundary, assuming a sufficient exposure time.

1.3 Research questions and objectives

In this dissertation, we propose the TR method as an alternate approach to inverse-source methods for wave focusing. To justify the proposition, we seek to numerically validate the TR in two- and three-dimensional elastic, heterogeneous, semi-infinite domains. We remark that, if and when successful, the application of the TR concept does not require that the medium's material distribution is *a priori* known. The method though does require that a source be installed at the target location to initiate the process. The latter requirement, depending on the application, may be less onerous than the uncertainty associated with the material properties.

Although the time-reversal method has been studied extensively in acoustics, its application in elastic media is on its early developmental stages. There are several issues associated with the application of the TR concept to elastodynamics, and in particular, to targets embedded within semi-infinite hosts. Moreover, the mathematical setting that led to the perfect refocusing described in the previous section was predicated upon conditions (boundary, initial, force, etc) that may not be physically realizable. Thus, it is of interest to understand how relaxing (or violating) these conditions will affect the refocusing. We outline next the main questions.

1. **Unbounded versus finite domain:** In the prototype acoustic case highlighted earlier, the domain of interest was finite and the side and bottom boundaries were terminated by Dirichlet (sound-soft) conditions.

In the elastic case of interest herein, the domain is semi-infinite in extent, and thus unbounded. This has three major implications: a. the bottom and sides of the physical domain are typically inaccessible and, thus, one cannot deploy a receiver/source array. Consequently, it is only the top surface that is available for the TRM deployment. b. When the TRM rebroadcasts the time-reversed signals back into the physical domain, the generated waves will be outgoing, without the benefit of reflecting off of a sound-soft boundary, as in the closed-cavity problem. Since a Dirichlet boundary acts as a secondary source, enhancing the focusing, its lack is expected to weaken the focusing, and affect its resolution. c. The computational assessment of the TR concept in unbounded elastic domains would require the rather challenging negotiation of the infinite extent through the introduction of appropriate truncation conditions that are capable of mimicking the physical setting.

2. **Source versus sink:** The ideal time-reversal implementation requires that the source be time-reversed, thus giving rise to the sink term of (1.4). A field implementation of the sink term would require a probe, acting as a source in the forward step, to be inserted at the location of the target. During the TR step, the probe's signal should be time-reversed, thus creating the sink. However, for a higher energy yield at the target, the TRM data are amplified, which means that to maintain problem coherency, the probe/source, now acting as a sink, must also be amplified. Typically, the probe/source does not have amplitude agility

to accommodate amplification as in the TRM. In other words, one cannot drive/install a strong motion actuator in an often deeply situated underground target region. Therefore, in the context of the problem at hand, the physical realization of the sink is impossible.

3. **Silent versus non-silent initial conditions:** The ideal time-reversal conditions require the implementation of non-zero initial conditions over the *entire* domain of interest, as suggested by (1.5c) and (1.5d) in the acoustic cavity case. This is clearly impossible to physically realize, and the ramifications should be assessed.

4. **Source signal and type:** Thus far, we have used the term *source* abstractly, without explicitly defining *what* source is being used. Obviously, the time-reversal method does not depend on how $f(\mathbf{x}, t)$ looks like in space and time. No matter what kind of source signal we use, the time-reversal method will focus the waves on the target, when ideal conditions are met. However, if the wave focusing is considered as a recourse for bringing about desired changes in the mechanical behavior of the target, it is worth studying the effect a particular choice of time signal may have on the refocused waves. Moreover, in the elastic case, owing to the vector character of either the displacements (Dirichlet condition) or the tractions (Neumann condition), a particular source direction (vertical or horizontal) may have a greater or a lesser effect on the intensity or the quality of focusing.

5. **Dirichlet versus Neumann TRM conditions:** In the acoustic time-reversal case, the pressures are recorded and time-reversed as pressures, i.e., the Dirichlet data are time-reversed as Dirichlet data. In the elastic case, however, recorded displacements (Dirichlet data) at the TRM cannot be time-reversed as displacements (Dirichlet data), due to equipment limitations. Instead, tractions (Neumann data) can be applied during the TR step, in lieu of displacements. This flipping of the boundary-applied data during the TR step is bound to affect the focusing, and the resolution. In theory, there are four pairs of possible data-matching between the forward and TR steps, abbreviated as: (D-to-D), (D-to-N), (N-to-D), and (N-to-N), where the first term of the abbreviation refers to the TRM-recorded data during the forward step, and the second refers to the TRM-rebroadcast data during the TR step. The D-to-N case, which is driven by physical constraints present in field implementations of the time-reversal method, worsens the refocusing quality [14, 19]. Herein, we also report on the implications of the D-to-N case.

6. **TRM density effects:** In an ideal time-reversal implementation, the TRM is infinite-dimensional, that is, there is an infinite number of sensors deployed along the TRM boundary. In practice, this is clearly infeasible: even in its finite-dimensional version (discrete), the number of sensors required at every node of a spatial discretization of the TRM boundary, is too large. There are, therefore, three issues that arise: a. what is the effect of the density of the TRM sensors on the focusing? b. what is the

effect of a limited coverage of the TRM boundary by sensors (limited aperture problem)? c. in the D-to-N case, the recording phase (forward step) requires displacement (or velocity/acceleration) recording sensors, whereas the TR phase requires the deployment of actuators along the TRM boundary. The density of the sensors and that of the actuators can be different. What is the effect on the focusing of this difference?

7. **Wave energy intensity control:** The refocus intensity is affected not only by the number and strength of actuators on Γ^{TRM}, but also by the material properties of the target, the contrast of the target's properties to those of the host, the distance from the TRM to the targets, the number of targets, etc. From an application perspective, it is of interest to be able to deliver comparable levels of energy to multiple subsurface targets even when at distance from each other, or even when the property contrast for each of the targets in the proximal area is different. We explore strategies to achieve comparable energy levels in such cases.

8. **Host heterogeneity effect:** Subsurface formations are heterogeneous. Most acoustic experiments (physical or numerical) to date focus on homogeneous hosts. We explore the effect of heterogeneity on the focusing, via suitable numerical experiments.

1.4 Dissertation outline

This dissertation is organized as follows:

In Chapter 2 we discuss the TR method for 2D elastic media. The development is incremental, starting from the ideal TR case in a homogeneous closed cavity, and proceeding with the TR case in an unbounded heterogeneous semi-infinite domain. For the latter, we study, one-by-one, the effect that the physically unrealizable conditions have on the quality of the refocusing. We also report on the effect other TR parameters (not physically constrained), such as the loading direction, or the type of source signal, have on the refocusing. We close with an application of the TR method to EOR, implicating a target embedded in a heterogeneous host.

In Chapter 3 we discuss in detail the ramifications associated with the change of the character of the TRM conditions between the forward (recording) and the TR steps, namely, of the D-to-N condition flipping. The development is incremental here as well, starting from the 1D scalar wave case, to 3D, and finally, we discuss a filter capable of restoring focusing resolution in certain applications.

In Chapter 4, we extend the previous developments to the all important 3D elastic case, involving multiple targets embedded in arbitrarily heterogeneous semi-infinite elastic media. We report numerical experiments involving TR mirrors of variable densities, and discuss strategies to control the energy intensity.

In Chapter 5 we offer conclusions and suggest future directions for related research.

Technical details pertinent to the numerical implementation are described in the Appendices.

Chapter 2

Time-reversal for wave energy focusing in 2D elastic media

The typical time-reversal setup for a finite domain is fairly simple and worth repeating: a wave source is placed at a location where it is of interest to have waves focused; the source is activated and emits waves, which are subsequently recorded on the TRM boundary –a receiver array occupying a portion of the domain's boundary; when the recorded motion at the TRM boundary is time-reversed and rebroadcast back into the domain, the waves will focus at the very location where the source was placed. The concept has been first used in acoustics. In this chapter, we extend the time-reversal concept to the elastic case, and study its ability to focus waves to targets embedded in heterogeneous semi-infinite hosts, while relaxing a number of physically unrealizable mathematical conditions.[1]

First, we study the closed-cavity elastic case, and then proceed with the unbounded host case, while relaxing the physically unrealizable conditions.

[1] A part of this chapter has been published as: S. Koo, P. M. Karve, and L. F. Kallivokas. A comparison of time-reversal and inverse-source methods for the optimal delivery of wave energy to subsurface targets, *Wave Motion*, 67:121-140, 2016, [37]. The author of this dissertation formulated the underlying mathematical problem and wrote a computer program to resolve it.

At the end, we will state the problem statement that best describes the most realistic situation and seek to confirm that the time-reversal method is capable of focusing wave energy.

2.1 TR in a finite domain – the ideal case

The ideal elastic TR case for a closed cavity is schematically depicted in Fig 2.1. Accordingly, Γ^{fixed} is a fixed boundary where the displacements vanish,

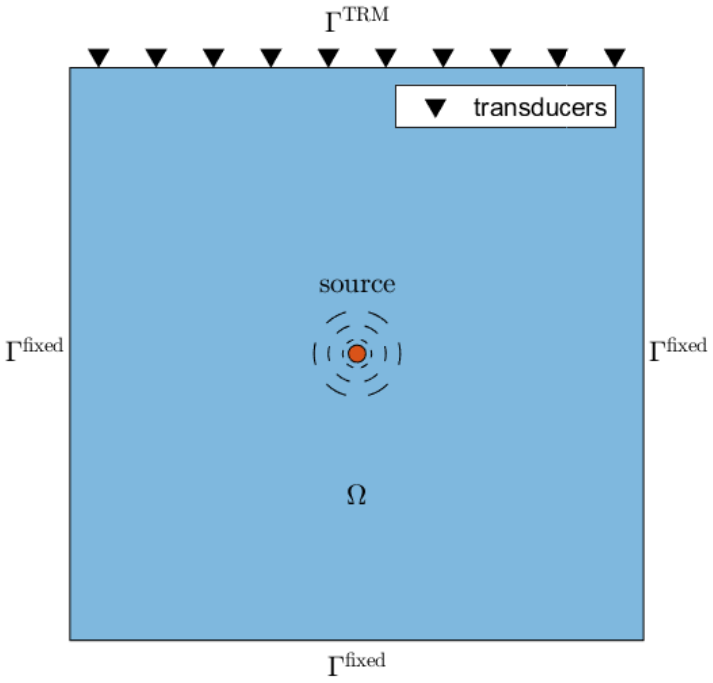

Figure 2.1: Forward step in a finite domain – the source is activated

and Γ^{TRM} is a traction-free boundary where the TRM is deployed. The TRM boundary is traction-free during the forward recording step, but during the

TR phase, it will revert to a broadcasting boundary.

The wave motion in an elastic medium is governed by Navier's equation [46]:

$$\rho\,\ddot{\mathbf{u}} - \nabla\cdot\left[\mu\left\{\nabla\mathbf{u} + (\nabla\mathbf{u})^{\intercal}\right\} + \lambda\,(\nabla\cdot\mathbf{u})\,\mathbf{I}\right] = \mathbf{f} \tag{2.1}$$

where $\mathbf{u}$ and $\mathbf{f}$ are functions of $\mathbf{x}\in\Omega$ and $0 < t \leqslant T$, ρ is mass density, μ and λ are Lamé parameters, $\mathbf{I}$ is the second-order identity tensor, and $\ddot{(\cdot)}$ indicates second-order partial derivative with respect to time.

2.1.1 The forward step

We install the TRM (the upside-down triangles in Fig 2.1) on $\Gamma^{\mathrm{TRM}} \subset \partial\Omega$, and fix the displacements on the rest of the boundary $\Gamma^{\mathrm{fixed}} = \partial\Omega\backslash\Gamma^{\mathrm{TRM}}$. Thus, the boundary conditions for the forward step read:

$$\mathbf{t}(\mathbf{x},t) = \mathbf{0}, \quad \mathbf{x}\in\Gamma^{\mathrm{TRM}}, \quad 0 < t \leqslant T \tag{2.2a}$$

$$\mathbf{u}(\mathbf{x},t) = \mathbf{0}, \quad \mathbf{x}\in\Gamma^{\mathrm{fixed}}, \quad 0 < t \leqslant T \tag{2.2b}$$

where $\mathbf{t}(\mathbf{x},t)$ is the traction vector. We assume silent initial conditions:

$$\mathbf{u}(\mathbf{x},0) = \mathbf{0}, \quad \mathbf{x}\in\Omega \tag{2.3a}$$

$$\dot{\mathbf{u}}(\mathbf{x},0) = \mathbf{0}, \quad \mathbf{x}\in\Omega. \tag{2.3b}$$

We solve equation (2.1), driven by a prescribed source $\mathbf{f}(\mathbf{x},t)$, subject to boundary conditions (2.2), and initial conditions (2.3) to obtain the displacement field $\mathbf{u}(\mathbf{x},t)$ in Ω. We record $\mathbf{u}(\mathbf{x},t)$ on Γ^{TRM} to prepare for the TR step.

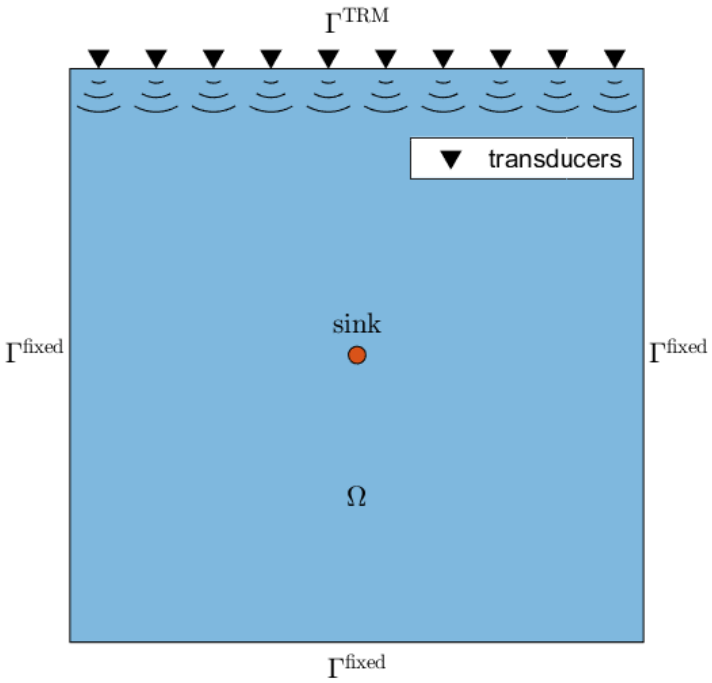

Figure 2.2: TR step in a finite domain – the TRM is activated

2.1.2 The time-reversal step

We seek next to determine the wavefield generated when the TRM is broadcasting the time-reversed recordings of the forward step. To distinguish the solutions between the forward and TR steps, we denote the displacement field of the TR step by $\mathbf{v}$. We assume that the TRM recorded the displacements during the forward step up to time $t = T$. Then the equations describing the TR step take the following form:

$$\rho\ddot{\mathbf{v}} - \nabla \cdot \left[\mu \left\{\nabla\mathbf{v} + (\nabla\mathbf{v})^{\intercal}\right\} + \lambda \left(\nabla \cdot \mathbf{v}\right)\mathbf{I}\right] = \mathbf{f}(\mathbf{x}, T - t), \quad \mathbf{x} \in \Omega. \tag{2.4}$$

We note that the wave source $\mathbf{f}$ of the forward step is time-reversed in equation (2.4) (now, it becomes the sink). The sink provides the evanescent wave information, which was not captured by the TRM due to the distance between the source/sink and the mirror. During the TR step, the sink absorbs the incoming waves and ensures a silent displacement field for $t > T$, which is consistent with the forward step's initial (silent) conditions (2.3). In the absence of the sink, the waves will refocus rather imperfectly, pass through the focal point (source/sink location), and eventually continue to travel inside the domain.

During the TR step the Dirichlet condition on Γ^{fixed} remains the same as in the forward step, whereas the boundary condition on Γ^{TRM} is driven by the time-reversed data:

$$\mathbf{v}(\mathbf{x}, t) = \mathbf{u}(\mathbf{x}, T - t), \quad \mathbf{x} \in \Gamma^{\text{TRM}} \tag{2.5a}$$

$$\mathbf{v}(\mathbf{x}, t) = \mathbf{0}, \qquad \mathbf{x} \in \Gamma^{\text{fixed}} \tag{2.5b}$$

where $\mathbf{u}(\mathbf{x}, T-t)$ represents the time-reversed forward TRM record. Moreover, at the end of the forward step ($t = T$), there exists a nonzero displacement field $\mathbf{u}(\mathbf{x}, T)$ in Ω. This field becomes the initial condition in the TR step, i.e.,

$$\mathbf{v}(\mathbf{x}, 0) = \quad \mathbf{u}(\mathbf{x}, T), \quad \mathbf{x} \in \Omega, \tag{2.6a}$$

$$\dot{\mathbf{v}}(\mathbf{x}, 0) = -\dot{\mathbf{u}}(\mathbf{x}, T), \quad \mathbf{x} \in \Omega. \tag{2.6b}$$

We seek to solve (2.4) subject to boundary conditions (2.5) and initial conditions (2.6).

2.1.3 Numerical implementation - Spatial discretization

In this section, we briefly describe the numerical solution of the forward and TR steps, following a classic Galerkin line. Accordingly, it can be shown that the weak form of equation (2.1) is:

$$\begin{aligned} &\int_{\Omega} \mathbf{w} \cdot \rho \ddot{\mathbf{u}} \, d\mathbf{x} \\ &+ \int_{\Omega} \nabla \mathbf{w} : \left[\mu \left\{ \nabla \mathbf{u} + (\nabla \mathbf{u})^{\intercal} \right\} + \lambda \left(\nabla \cdot \mathbf{u} \right) \mathbf{I} \right] \, d\mathbf{x} \\ &= \int_{\Omega} \mathbf{w} \cdot \mathbf{f} \, d\mathbf{x}, \quad \mathbf{x} \in \Omega, \end{aligned} \tag{2.7}$$

where $\mathbf{w}(\mathbf{x})$ is an admissible test function. Next, we introduce finite-dimensional subspaces $\mathbf{H^1(\Omega)}$ with basis functions $\mathbf{\Phi}(\mathbf{x})$ and approximate $\mathbf{u}(\mathbf{x}, t)$ and $\mathbf{w}(\mathbf{x})$ such that:

$$\mathbf{u}(\mathbf{x}, t) \approx \mathbf{u}_h(\mathbf{x}, t) = \begin{bmatrix} \mathbf{\Phi}^{\intercal}(\mathbf{x}) \, \mathbf{u}_x(t) \\ \mathbf{\Phi}^{\intercal}(\mathbf{x}) \, \mathbf{u}_y(t) \end{bmatrix} \tag{2.8a}$$

$$\mathbf{w}(\mathbf{x}) \approx \mathbf{w}_h(\mathbf{x}) = \begin{bmatrix} \boldsymbol{\Phi}^{\mathsf{T}}(\mathbf{x})\, \mathbf{w}_x \\ \boldsymbol{\Phi}^{\mathsf{T}}(\mathbf{x})\, \mathbf{w}_y \end{bmatrix}, \tag{2.8b}$$

where $\mathbf{u}_x(t)$ and $\mathbf{u}_y(t)$ are vectors of unknown nodal displacements in the global x and y directions, respectively. Upon introduction of the approximants (2.8) in the weak form (2.7), there results:

$$\mathbf{M}\ddot{\mathbf{u}}(t) + \mathbf{K}\mathbf{u}(t) = \mathbf{f}(t). \tag{2.9}$$

$\mathbf{M}$ and $\mathbf{K}$ are $n \times n$ mass and stiffness matrices, respectively, where n is the number of degrees of freedom in the finite element mesh; similarly, $\mathbf{u}$ is the vector of nodal displacement histories. Details on the explicit form of $\mathbf{M}$ and $\mathbf{K}$ can be found in Appendix A.1.1.

The semi-discrete form (2.9) can be used to simulate either the forward or the TR step. When (2.9) is used for the forward step, the wave propagation is driven by the source term, and thus $\mathbf{u}$ encompasses all nodes in $\Omega \setminus \Gamma^{\text{fixed}}$. By contrast, when (2.9) is used to model the TR step, the wave propagation is driven by the Dirichlet data on Γ^{TRM} and the domain sink term. In this case, the vector of the unknown nodal displacement histories $\mathbf{u}$ is reduced to account for all nodes in $\Omega \setminus (\Gamma^{\text{fixed}} \cup \Gamma^{\text{TRM}})$. Consequently, the semi-discrete form (2.9) is partitioned to read:

$$\begin{bmatrix} \mathbf{M}_{\text{TRM TRM}} & \mathbf{M}_{\text{TRM Int}} \\ \mathbf{M}_{\text{Int TRM}} & \mathbf{M}_{\text{Int Int}} \end{bmatrix} \begin{bmatrix} \ddot{\mathbf{u}}_{\text{TRM}} \\ \ddot{\mathbf{u}}_{\text{Int}} \end{bmatrix} + \begin{bmatrix} \mathbf{K}_{\text{TRM TRM}} & \mathbf{K}_{\text{TRM Int}} \\ \mathbf{K}_{\text{Int TRM}} & \mathbf{K}_{\text{Int Int}} \end{bmatrix} \begin{bmatrix} \mathbf{u}_{\text{TRM}} \\ \mathbf{u}_{\text{Int}} \end{bmatrix} = \begin{bmatrix} \mathbf{0} \\ \mathbf{f}_{\text{Int}} \end{bmatrix}, \tag{2.10}$$

where subscript TRM refers to the TRM boundary, and subscript Int refers to the interior domain. We use Gauss-Lobatto integration, which forces the off-diagonal block mass matrices to vanish [38, 55]. Thus, the second equation of the semi-discrete form (2.10) reduces to:

$$\mathbf{M}_{\text{Int Int}}\ddot{\mathbf{u}}_{\text{Int}} + \mathbf{K}_{\text{Int Int}}\mathbf{u}_{\text{Int}} = \mathbf{f}_{\text{Int}} - \mathbf{K}_{\text{Int TRM}}\mathbf{u}_{\text{TRM}}, \tag{2.11}$$

where, $\mathbf{f}_{\text{Int}}$ includes the sink information and $\mathbf{K}_{\text{Int TRM}}\mathbf{u}_{\text{TRM}}$ provide the time-reversed Dirichlet data, per (2.5).

2.1.4 Numerical implementation - Time integration

Either of the semi-discrete forms (2.9) and (2.11) can be converted into a system of first-order differential equations through the introduction of auxiliary variables, as in:

$$\mathbf{x}_1(t) = \mathbf{u}(t), \qquad \mathbf{x}_2(t) = \dot{\mathbf{u}}(t),$$

which lead to (using, for example (2.9)):

$$\begin{bmatrix} \dot{\mathbf{x}}_1 \\ \dot{\mathbf{x}}_2 \end{bmatrix} = \begin{bmatrix} \mathbf{0} & \mathbf{I} \\ -\mathbf{M}^{-1}\,\mathbf{K} & \mathbf{0} \end{bmatrix} \begin{bmatrix} \mathbf{x}_1 \\ \mathbf{x}_2 \end{bmatrix} + \begin{bmatrix} \mathbf{0} \\ \mathbf{M}^{-1}\,\mathbf{f} \end{bmatrix}. \tag{2.12}$$

We remark that $\mathbf{M}$ is diagonal, by virtue of the use of a Gauss-Lobatto quadrature, and thus it is trivially invertible. Similarly, equation (2.11) can be recast as:

$$\begin{bmatrix} \dot{\mathbf{x}}_1 \\ \dot{\mathbf{x}}_2 \end{bmatrix} = \begin{bmatrix} \mathbf{0} & \mathbf{I} \\ -\mathbf{M}^{-1}_{\text{int int}}\,\mathbf{K}_{\text{int int}} & \mathbf{0} \end{bmatrix} \begin{bmatrix} \mathbf{x}_1 \\ \mathbf{x}_2 \end{bmatrix} + \tag{2.13}$$

$$\begin{bmatrix} \mathbf{0} \\ \mathbf{M}_{\text{int int}}^{-1} \ (\mathbf{f}_{\text{int}} - \mathbf{K}_{\text{int TRM}} \mathbf{u}_{\text{TRM}}) \end{bmatrix}$$

Equations (2.12) and (2.13) can be solved using any time integration scheme; herein, we use an explicit fourth-order Runge-Kutta method (RK4), whose details are discussed in Appendix B.

2.1.5 Numerical results – TR for a closed-cavity

We use the prototype problem depicted in Figures 2.1 and 2.2 for the closed-cavity simulation: the model is a square 50 m by 50 m, with wave source/sink placed at its center. The domain is homogeneous, with a compressional wave speed $c_p = 369.2745$ m/s and a shear wave speed of $c_s = 213.2007$ m/s. We use 9-node quadrilateral elements for the finite element mesh, and a time step of $\Delta t = 0.001$s. The total simulation duration is $T = 0.425$s. The

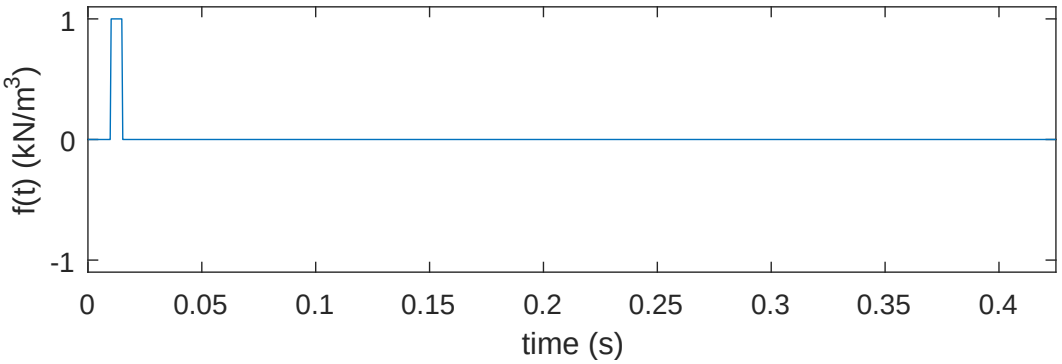

Figure 2.3: Wave source time signal for the forward step

source is defined as:

$$\mathbf{f}(\mathbf{x}, t) = \delta(\mathbf{x} - \mathbf{x}_0) \begin{cases} 1, & 0.010 \text{ s} \leqslant t \leqslant 0.015 \text{ s} \\ 0, & \text{otherwise} \end{cases}$$

Figure 2.3 depicts the time signal, with $\mathbf{x}_0 = (25,\ 25)$ m. The source is designed to ramp up to full amplitude 0.01 seconds after the onset of the simulation. The 0.01 seconds of initial silence is introduced to allow for the visualization of the sink effect. As mentioned earlier, the sink, during the TR step, will provide the evanescent information, which is not accounted for in the TRM recordings. Later, in section 2.2.2, we study the ramifications of having the sink removed, and to this end, the initial 0.01 seconds of silence are necessary.

Snapshots of the displacement field during the forward and the TR steps are plotted in Figs. 2.4 and 2.5, respectively. In the forward step, the wave source was activated only along the x-direction (horizontal direction), whereas in the TR step, the TRM time-reversed displacement were applied along both the x- and y-directions. We note that the y displacement components are fairly small due to the horizontal direction of the source, and have been normalized for graphing purposes.

As it can be seen from Fig. 2.5, the waves refocus perfectly, and silent final conditions are achieved, as expected.

2.2 TR in a semi-infinite domain - Unrealizable conditions and ramifications

In the previous section, we saw that, under ideal conditions, the implementation of the time-reversal concept would yield perfect focusing at the source location, in the case of an elastic closed-cavity. Here, we start by peeling away one-by-one the various conditions that are unrealizable in a physical

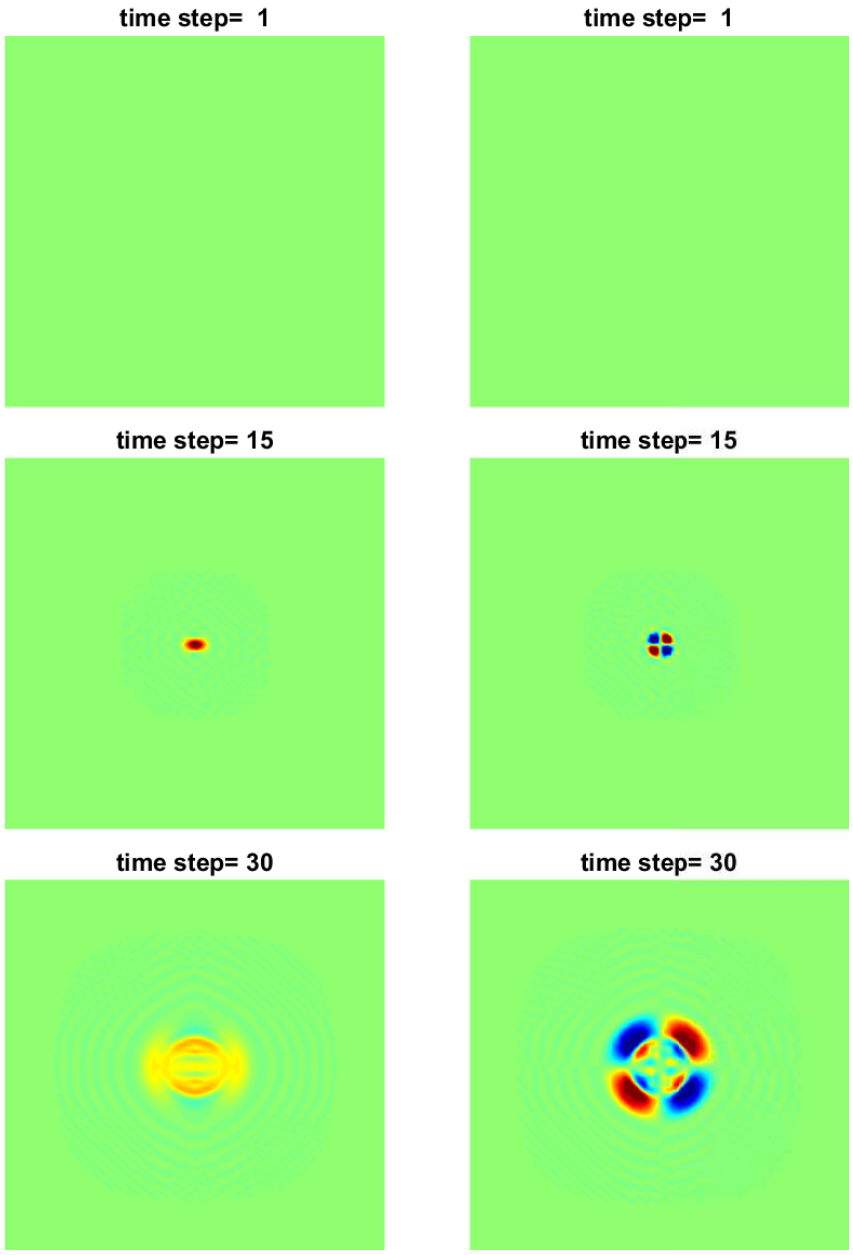

Figure 2.4: Forward wave propagation; x-direction displacement (left); y-direction displacement (right)

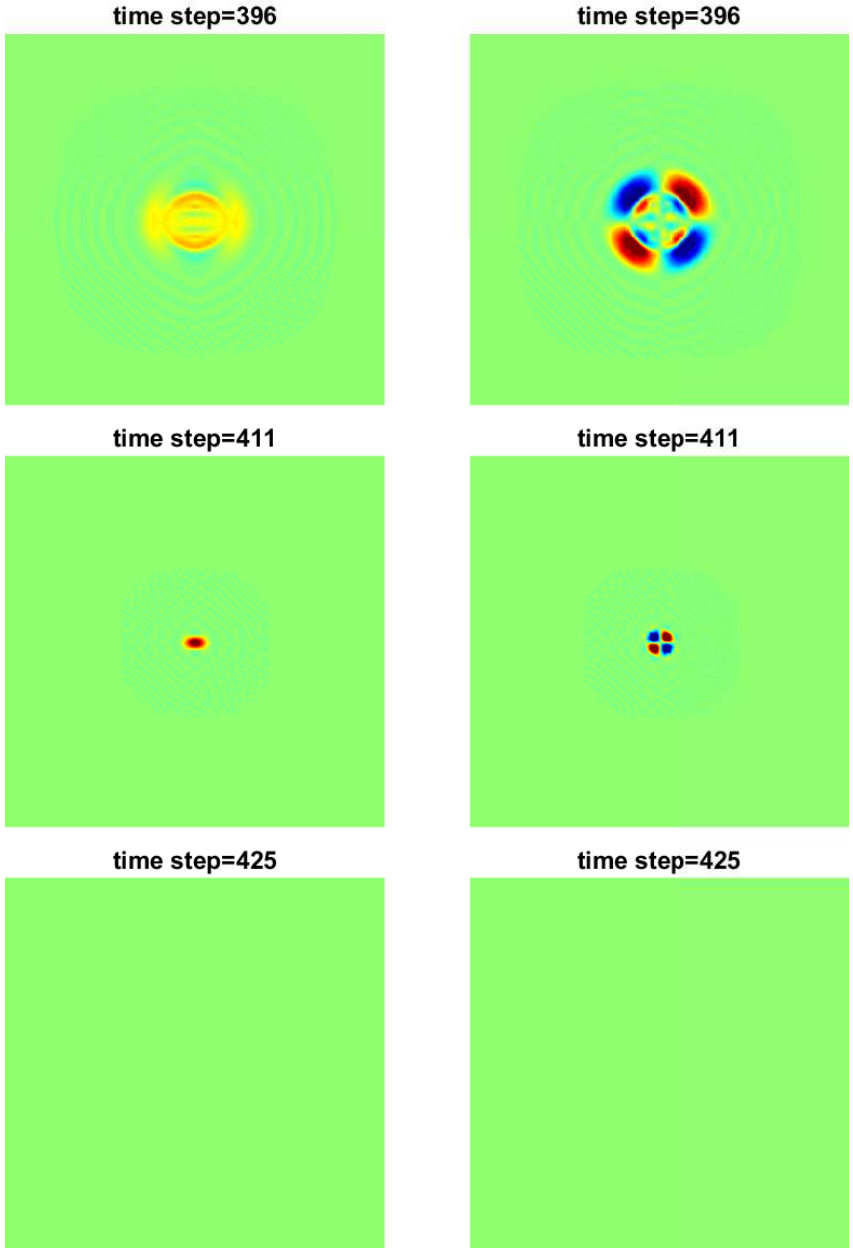

Figure 2.5: TR wavefield; x-direction displacement (left); y-direction displacement (right)

setting involving subsurface targets embedded in a semi-infinite host, to test numerically whether focusing is still possible, and to assess its resolution. At the end of the section, we apply the time-reversal concept to a realistic prototype case involving a shallow target reservoir, with an eye towards enhanced oil recovery.

2.2.1 Effect of initial conditions

As was mentioned earlier, one cannot introduce nonzero initial conditions during the TR step over the entire domain, as was suggested by (2.6). We, therefore, replace (2.6) by silent initial conditions. Accordingly, (2.6) now reads:

$$\begin{aligned} \mathbf{v}(\mathbf{x}, 0) &= \mathbf{0}, \quad \mathbf{x} \in \Omega \\ \dot{\mathbf{v}}(\mathbf{x}, 0) &= \mathbf{0}, \quad \mathbf{x} \in \Omega. \end{aligned} \tag{2.14}$$

Figure 2.6 depicts the TR wave field when silent conditions are used: it should be compared against Fig. 2.5. Notice that, by contrast to the ideal case, silence at the end of the simulation duration has not been achieved. Moreover, even though the waves have still refocused at the source, the refocus has lost its original sharpness. Overall, the resolution has deteriorated, there is more residual motion in the domain, but the refocus remains quite acceptable.

2.2.2 Effect of sink

A field implementation of the sink term requires that the wave source be again activated during the TR step, albeit with the time-reversed source

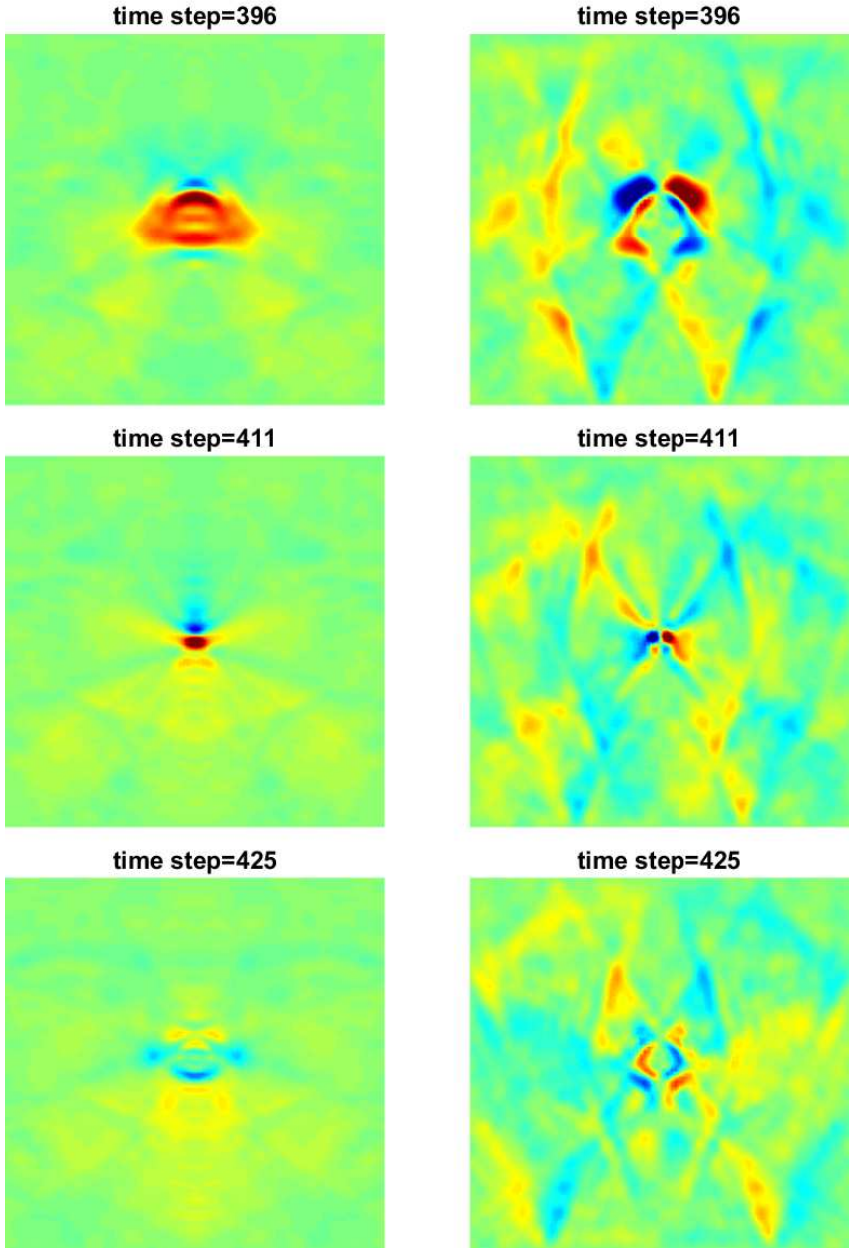

Figure 2.6: TR wavefield; silent initial conditions; x-direction displacement (left); y-direction displacement (right)

signal. However, to yield higher energy at the target, the TRM data would be amplified, and in order to maintain problem coherency, the sink signal must be amplified too. Therein lies the physical limitation: typical probes, used as wave sources within the target, do not have the kind of amplitude agility that will be required to match the amplification of the time-reversed TRM signals. For this reason, we omit the sink term from our numerical simulation (in addition to the nonzero initial values of the preceding section), and assess the effect of the sink's omission computationally. This omission will not allow for silent final conditions during the TR step. But, since we are interested in delivering wave energy to the target, rather than localizing or detecting the source, a sharply localized refocus with silent pre- and post-focus behavior is not a necessity. In fact, the nonzero final displacements (velocities or accelerations) may add more energy to the target, which could be beneficial to the application.

To remove the sink, equation (2.11) is reduced to:

$$\mathbf{M}_{\text{int int}}\ddot{\mathbf{u}}_{\text{int}} + \mathbf{K}_{\text{int int}}\mathbf{u}_{\text{int}} = -\mathbf{K}_{\text{int TRM}}\mathbf{u}_{\text{TRM}} \tag{2.15}$$

and the corresponding first-order system is modified to read:

$$\begin{bmatrix} \dot{\mathbf{x}}_1 \\ \dot{\mathbf{x}}_2 \end{bmatrix} = \begin{bmatrix} \mathbf{0} & \mathbf{I} \\ -\mathbf{M}^{-1}_{\text{int int}}\,\mathbf{K}_{\text{int int}} & \mathbf{0} \end{bmatrix} \begin{bmatrix} \mathbf{x}_1 \\ \mathbf{x}_2 \end{bmatrix} + \begin{bmatrix} \mathbf{0} \\ -\mathbf{M}^{-1}_{\text{int int}}\,\mathbf{K}_{\text{int TRM}}\,\mathbf{u}_{\text{TRM}} \end{bmatrix}. \tag{2.16}$$

The resulting wavefield during the TR step is shown in Fig. 2.7. Refocus is still achieved both in the x- and y-directions (time step 411); the ripples, following the refocus are stronger than those observed in the preceding section's case when the sink was not removed.

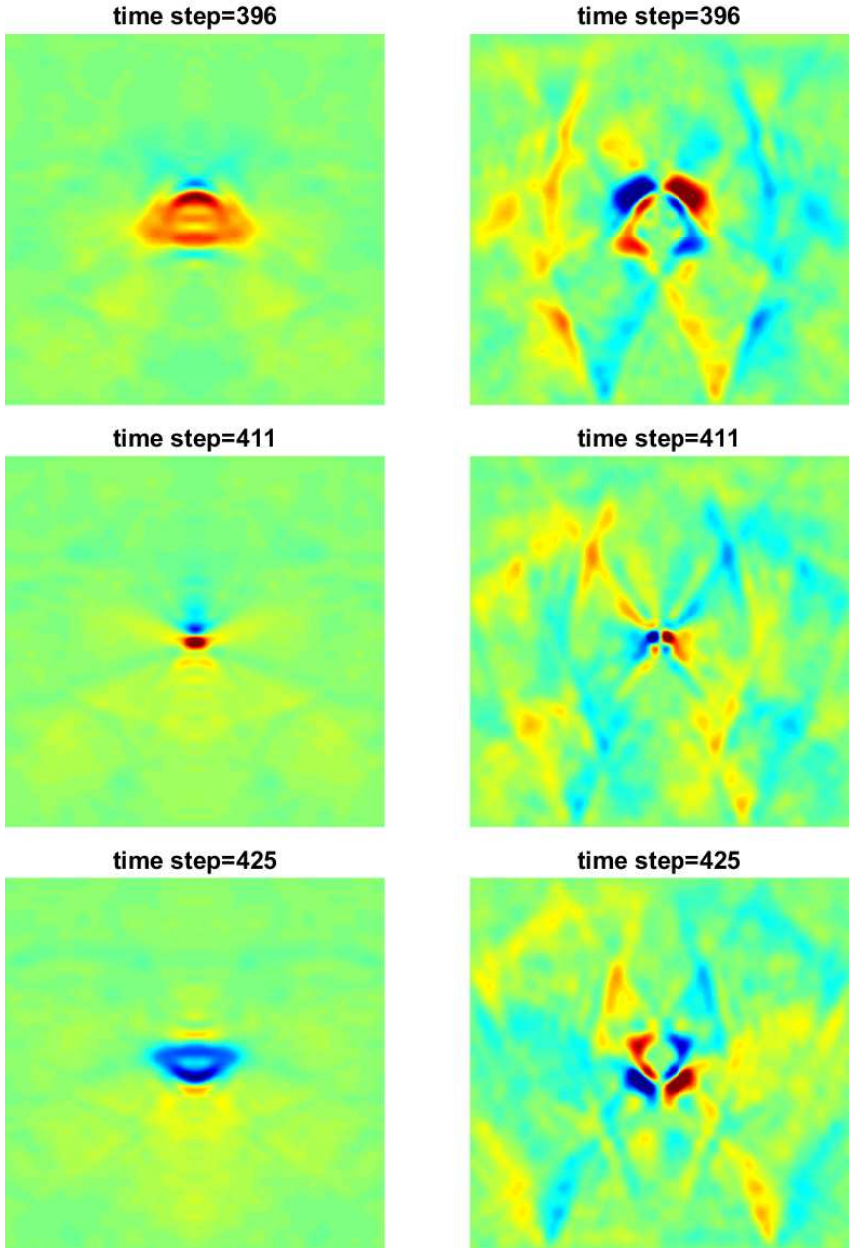

Figure 2.7: TR wavefield; silent initial conditions; sink term removed; x-direction displacement (left); y-direction displacement (right)

2.2.3 Effect of loading direction

In the elasticity case, there are either two (in 2D) or three displacement components (in 3D) recorded at the TRM. In the preceding sections, when the recordings at the TRM were time-reversed, both displacement components were rebroadcast back in the domain, i.e., both the horizontal and the vertical components were applied on the TRM boundary. However, in field implementations, it would be impossible to simultaneously apply excitations in both directions. In fact, as it will be discussed in the next section, there is not even the ability to apply Dirichlet data on the TRM, and as it will be shown, we opt for applying tractions (Neumann data), fed by the time-reversed traces of the displacement records (Dirichlet data). The issue of limited directionality choice (horizontal or vertical, but not both) arises equally whether one uses Dirichlet or Neumann data. Since, excluding one loading direction undermines the mathematical coherency of the TR step, in this section we assess computationally the impact of the loading direction choice in the focusing. To this end, only the x- or y TRM-recorded displacement component is time-reversed during the TR step. The corresponding wavefields are shown in Figs. 2.8 and 2.9.

Both simulations, for either loading direction, show that the horizontal (x) component of the motion is successfully refocusing at time step 411. The vertical (y) motion component's refocus is not obvious when the TR step is fueled by the horizontal TRM motion: note the fuzziness of the wavefield depicted in the right column of Fig. 2.8.

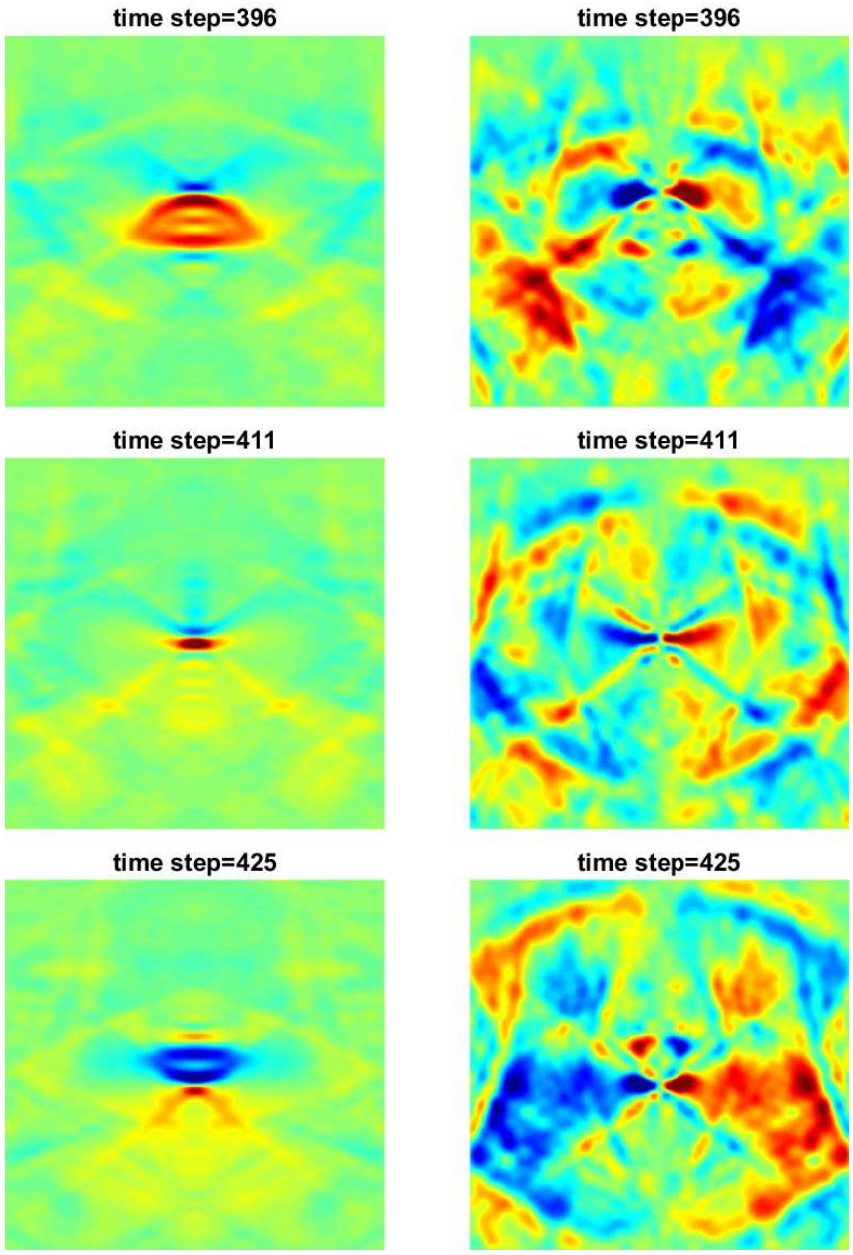

Figure 2.8: TR wavefield; x-direction displacement (left); y-direction displacement (right); silent initial conditions; sink term removed; TRM Dirichlet boundary condition in x-direction (horizontal) only

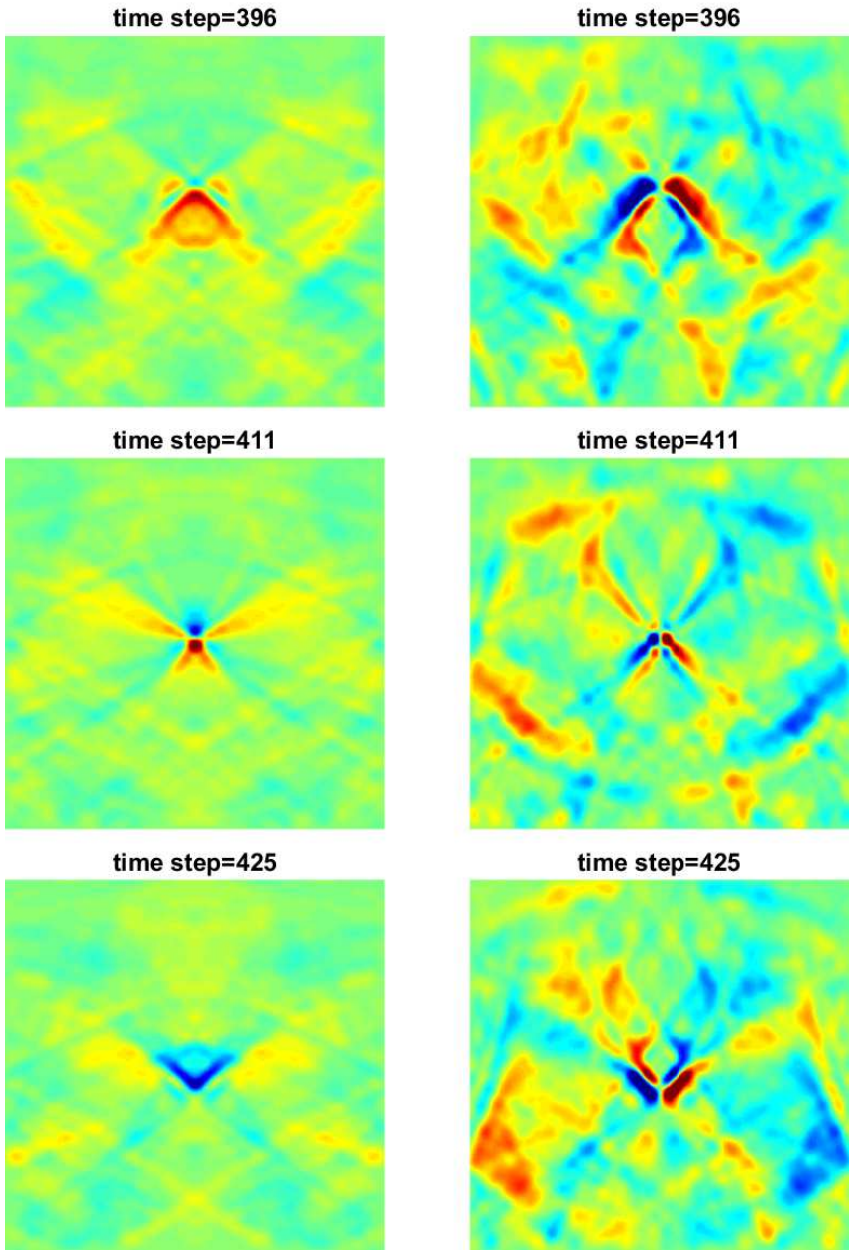

Figure 2.9: TR wavefield; x-direction displacement (left); y-direction displacement (right); silent initial conditions; sink term removed; TRM Dirichlet boundary condition in y-direction (vertical) only

We also observe that the horizontal component refocus is somewhat more dispersed in space in the x-direction-driven TR case, versus the y-direction-driven TR case (compare the left columns of Figs. 2.8 and 2.9).

However, these observations do not imply that the y-direction loading has a greater effect on the refocus than the x-direction loading. On the contrary, when we look at the refocused wave amplitudes, the refocus has greater amplitude when the x-direction loading is used. This can be seen more clearly from the time traces at the target, depicted in Fig. 2.10c. The amplitude of the blue line is higher than the red line, which indicates that what actually induces stronger wave motion is the x-direction load.

2.2.4 D-to-N boundary condition flipping

Thus far, the condition driving the TR step in the series of numerical experiments discussed in the previous sections was of the Dirichlet type (applied time-reversed displacement components). However, due to equipment limitations, as mentioned earlier in section 2.2.1, it is impossible to apply a time-variant Dirichlet type boundary condition on the ground surface. This fact necessitates the use of a traction boundary condition in the TR step. Accordingly, we drive the TR step with:

$$\mathbf{t}(\mathbf{x}, t) = \mathbf{u}(\mathbf{x}, T - t) \tag{2.17}$$

instead of

$$\mathbf{v}(\mathbf{x}, t) = \mathbf{u}(\mathbf{x}, T - t)$$

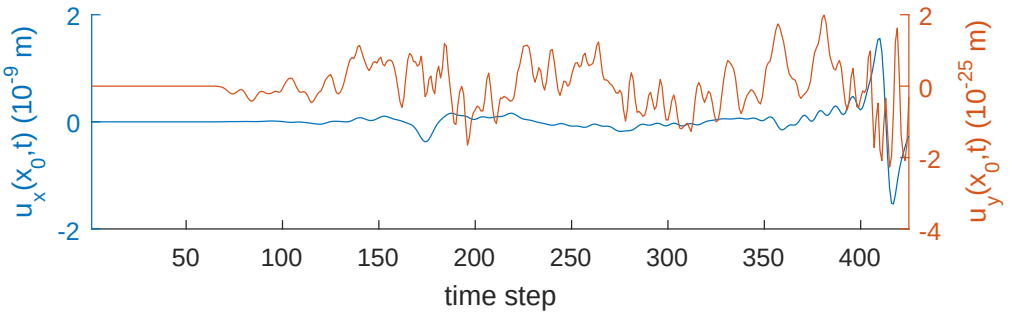

(a) Displacement time histories at the target ($\mathbf{x}_0$) when the TR is driven by the x-direction TRM data; x displacement component shown in blue; y displacement component shown in red; y component is 16 orders of magnitude less than x component

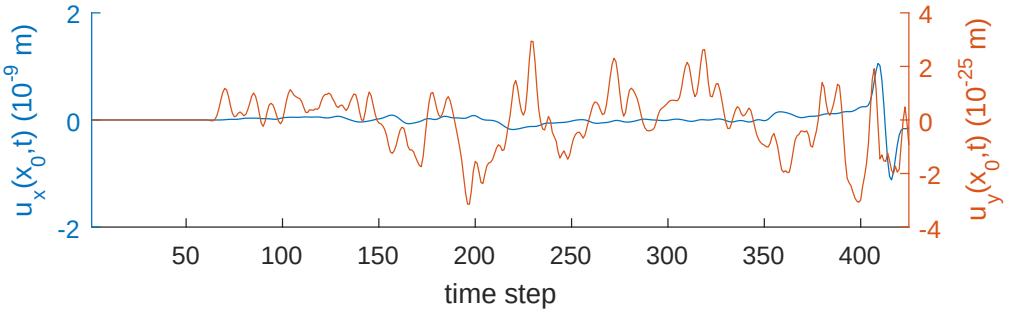

(b) Displacement time histories at the target ($\mathbf{x}_0$) when the TR is driven by the y-direction TRM data; x displacement component shown in blue; y displacement component shown in red; y component is 16 orders of magnitude less than x component

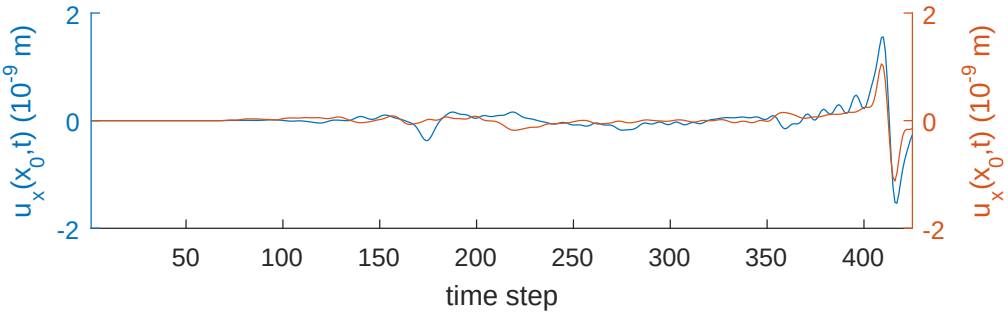

(c) Horizontal component displacement time histories at the target ($\mathbf{x}_0$); trace shown in blue when the TR is driven by the x-direction TRM data; trace shown in red when the TR is driven by the y-direction TRM data

Figure 2.10: Displacement time histories at the target $\mathbf{x}_0$

on Γ^{TRM}. Equation 2.17 implies that the time-domain trace of the displacements is used to apply tractions with, however, a suitable adjustment to the amplitude and units. We refer to this change in the boundary condition as *D-to-N flipping*. Fink et al. [14] and Fannjiang [19] studied the effect of applying a Dirichlet datum as a Neumann boundary condition in acoustics, and their analysis showed that refocus can still be achieved with, however, degraded resolution.

Figure 2.11 depicts the wavefield due to *D-to-N flipping*, when tractions are applied only along the horizontal direction. We remark that there is refocus at the target (step 411), albeit the energy has been spatially dispersed in the vicinity of the target, implying significant resolution loss.

2.2.5 TR in semi-infinite heterogeneous host - Application to EOR

In this section, we combine all previously discussed relaxations of the ideal TR conditions, extend the methodology to a semi-infinite host, introduce heterogeneity, and apply the TR concept to a prototype reservoir model for the purpose of enhancing oil mobility.

To this end, we consider a synthetically created, two-dimensional, layered, elastic, isotropic geological formation model (Figure 2.12). The formation model consists of four layers, with an elliptic inclusion sandwiched between the third and fourth layers. The major and minor semi-axes of the elliptic inclusion are, respectively, 15 m and 7.5 m long. The top boundary ($y = 0$) represents the ground surface, where we apply loads and record displacements (the TR

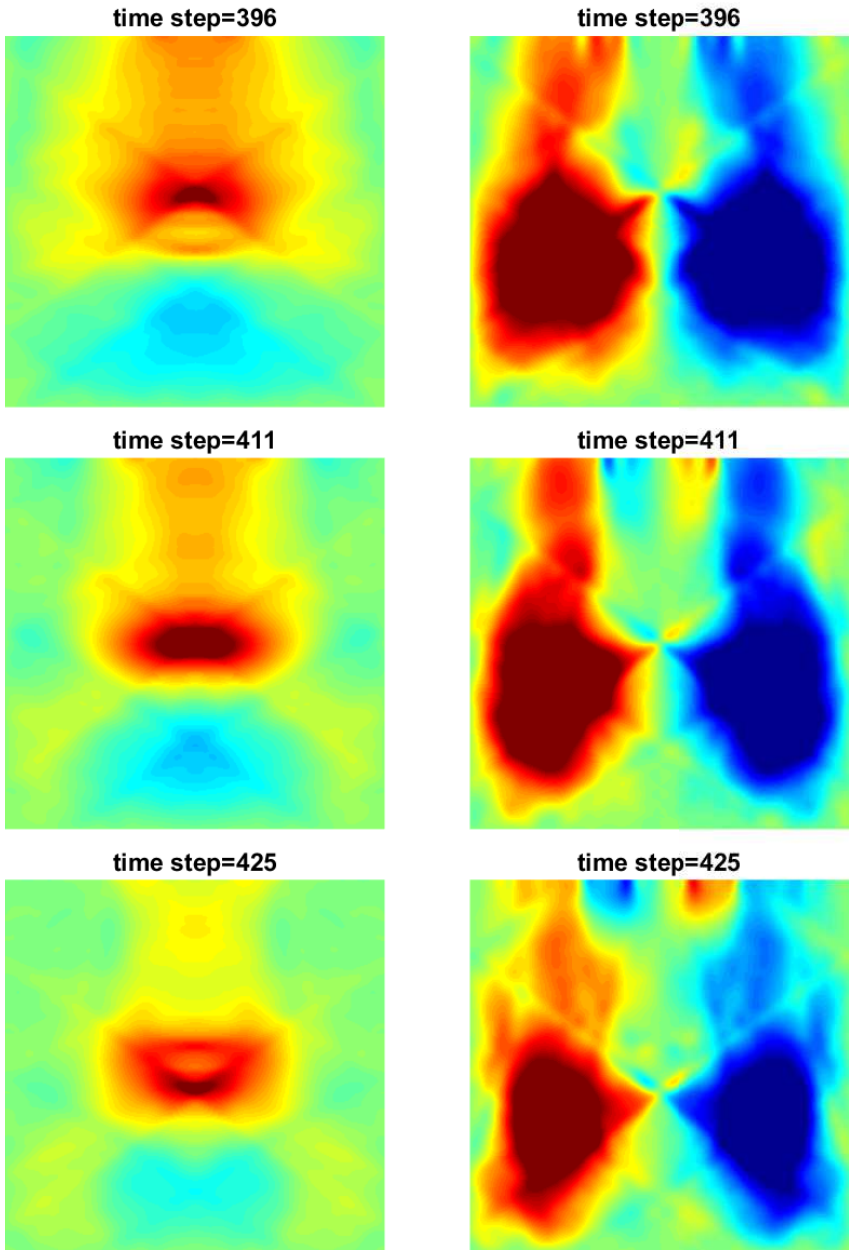

Figure 2.11: TR wavefield; x-direction displacement (left); y-direction displacement (right); silent initial conditions; sink term removed; D-to-N flipping; load applied as horizontal tractions only at the TRM

Table 2.1: Material properties of the layers and inclusion in the geophysical formation model

	ρ (kg/m^3)	ν	E (GPa)	c_p (m/s)	c_s (m/s)
Layer 1	2,200	0.2	1.5	870.4	533.0
Layer 2	2,200	0.2	2.5	1,123.7	688.1
Layer 3	2,200	0.2	3.5	1,329.5	814.2
Layer 4	2,200	0.2	4.5	1,507.6	923.2
Inclusion	2,200	0.2	1.0	710.7	435.2

mirror). Material properties of the layers are summarized in Table 2.1. Note that in Table 2.1, ρ, ν and E are mass density, Poisson's ratio and Young's modulus, respectively. c_p and c_s are the primary and the secondary wave speeds which are calculated as:

$$c_p = \sqrt{\frac{\lambda + 2\mu}{\rho}}, \quad c_s = \sqrt{\frac{\mu}{\rho}},$$

where λ and μ are the Lamé parameters which can be obtained by [53]

$$\lambda = \frac{\nu E}{(1+\nu)(1-2\nu)}, \quad \mu = \frac{E}{2(1+\nu)}.$$

We begin our numerical experimentation by considering two important aspects of time-reversal for geophysical applications in semi-infinite media: (a) the number of sources used for TR, and (b) the time signal (frequency content) used in the forward step. In practice, it is not feasible to cover the ground surface by sensors and motion actuators. Thus, it is important to evaluate the effect the number of sensors/sources has on the quality and intensity of the refocus. In this experiment, we vary the number of the uniformly distributed

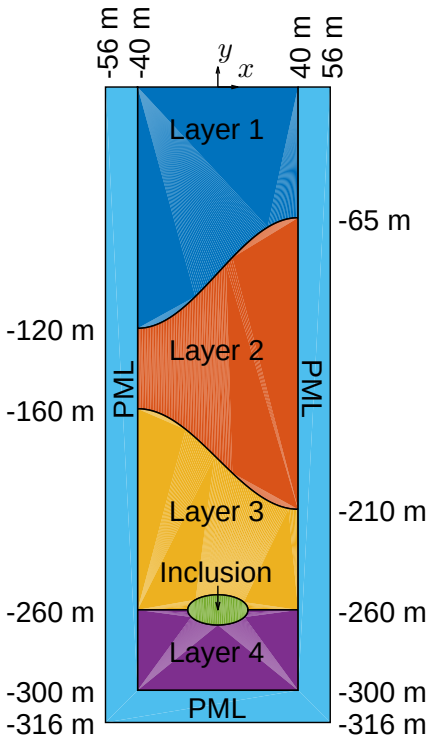

Figure 2.12: Geophysical formation model

sensors installed on the (80 m-wide) top boundary ($y = 0$) of the geological formation model, and study the effect of mirror density on refocusing. Specifically, we place adjacent sensors (and sources) either 0.5 m apart (full mirror), or 2.0 m apart (quarter density mirror). Thus, although the full and quarter density mirrors use different sensor spacing, they cover the entire 80 m-wide top boundary, i.e., the size of the mirror remains the same for both cases. Another key aspect of the TR method is the choice of the time signal used in the forward step. Although the governing physics allows refocus irrespective of the frequency content of the forward step signal, the amount of energy delivered to the target may be significantly different for different forward step signals. Presumably, the most efficient energy delivery is expected when the source signal in the forward step contains the amplification frequency of the model, which is, however, unknown unless the formation has been previously well characterized. Here, we experiment with two types of signals in the forward step: (a) a series of rectangular pulses forming a comb-like signal (continuous wavelike signal with narrow frequency support); and (b) a modified Ricker pulse (a pulse-like signal with wide frequency support). Thus, in this numerical experiment, for each of the forward step signals mentioned above, we evaluate the effect of the mirror density, and report on the quality and intensity of wave energy focusing.

2.2.5.1 Domain truncation - PML

To numerically simulate the propagation of waves in the semi-infinite domain of interest, the domain must be truncated to render a finite computational domain. To this end, we introduce Perfectly-Matched-Layers (PMLs) on the truncation surfaces. The PML is a buffer zone within which the outgoing waves are forced to decay rapidly. The PML concept was introduced by Bérenger for electromagnetic waves [8] in 1994. The PML for elastodynamics used in this dissertation was developed by Kucukcoban et al. [39, 40] and Fathi et al. [21–23]. Other applications of the same PML developed can be also found in [46–48].

In the PML, the balance of linear momentum, and the combined constitutive and kinematic equation take the following form, respectively:

$$\nabla \cdot \left(\dot{\mathbf{S}}^{\intercal} \mathbf{\Lambda}_e + \mathbf{S}^{\intercal} \mathbf{\Lambda}_p \right) = \rho \left(\mathsf{a} \ddot{\mathbf{v}} + \mathsf{b} \dot{\mathbf{v}} + \mathsf{c} \mathbf{v} \right), \quad \mathbf{x} \in \Omega_{\mathrm{PML}} \tag{2.18a}$$

$$\begin{aligned} \mathsf{a} \ddot{\mathbf{S}} + \mathsf{b} \dot{\mathbf{S}} + \mathsf{c} \mathbf{S} = & \mu \left(\left(\nabla \dot{\mathbf{v}} \right) \mathbf{\Lambda}_e + \mathbf{\Lambda}_e \left(\nabla \dot{\mathbf{v}} \right)^{\intercal} + \left(\nabla \mathbf{v} \right) \mathbf{\Lambda}_p + \mathbf{\Lambda}_p \left(\nabla \mathbf{v} \right)^{\intercal} \right) + \\ & \lambda \left(\nabla \cdot \left(\mathbf{\Lambda}_e \dot{\mathbf{v}} \right) + \nabla \cdot \left(\mathbf{\Lambda}_p \mathbf{v} \right) \right) \mathbf{I}, \quad \mathbf{x} \in \Omega_{\mathrm{PML}}. \end{aligned} \tag{2.18b}$$

They are subject to the following boundary conditions:

$$\left(\dot{\mathbf{S}}^{\intercal} \mathbf{\Lambda}_e + \mathbf{S}^{\intercal} \mathbf{\Lambda}_p \right) \mathbf{n}_{\mathrm{PML}} = \mathbf{0}, \qquad \mathbf{x} \in \Gamma_{\mathrm{PML}}^{\mathrm{free}} \tag{2.19a}$$

$$\mathbf{v} = \mathbf{0}, \qquad \mathbf{x} \in \Gamma_{\mathrm{PML}}^{\mathrm{fixed}} \tag{2.19b}$$

$$\mathbf{v}_{\mathrm{REG}} = \mathbf{v}_{\mathrm{PML}}, \qquad \mathbf{x} \in \Gamma_{\mathrm{I}} \tag{2.19c}$$

$$\begin{aligned} & \left[\mu \left(\nabla \mathbf{v} + \left(\nabla \mathbf{v} \right)^{\intercal} \right) + \lambda \left(\nabla \cdot \mathbf{v} \right) \mathbf{I} \right] \mathbf{n}_{\mathrm{REG}} \\ & \quad + \left(\dot{\mathbf{S}}^{\intercal} \mathbf{\Lambda}_e + \mathbf{S}^{\intercal} \mathbf{\Lambda}_p \right) \mathbf{n}_{\mathrm{PML}} = \mathbf{0}, \qquad \mathbf{x} \in \Gamma_{\mathrm{I}}. \end{aligned} \tag{2.19d}$$

In the above, Ω_{PML} represents the domain occupied by the PML buffer, $\Gamma^{\text{free}}_{\text{PML}}$ is the traction free portion of the PML, Γ_{I} is the interface between the PML buffer and the regular domain Ω_{REG}, $\Gamma^{\text{fixed}}_{\text{PML}}$ is the outer boundary of the PML buffer where the displacements vanish. Equation (2.19a) indicates that the traction is zero on $\Gamma^{\text{free}}_{\text{PML}}$, equation (2.19b) is the Dirichlet condition on the fixed outer PML boundary $\Gamma^{\text{fixed}}_{\text{PML}}$, equation (2.19c) enforces the continuity of displacements on the interface Γ_{I}, and equation (2.19d) is the continuity of tractions across Γ_{I}. Moreover, $\mathbf{n}_{\text{REG}}$ are the outward normal to the interface Γ_{I}, pointing to the PML buffer, and $\mathbf{n}_{\text{PML}} = -\mathbf{n}_{\text{REG}}$; $\mathbf{S}$ denotes the stress tensor; the definitions for the rest of the parameters can be found in [23, 39, 40].

The equations governing the motion in the regular domain (equations (2.4) and (2.17)), the PML equations (2.18), and the boundary and interface conditions (2.19), form the complete set of equations for the numerical simulation of the TR step within the semi-infinite domain.

The weak form, in the Galerkin sense, of the governing equations becomes [23]:

$$
\begin{aligned}
&\int_{\Omega_{\text{REG}}} \mathbf{w} \cdot \rho \ddot{\mathbf{u}} \, d\mathbf{x} \\
&+ \int_{\Omega_{\text{REG}}} \nabla \mathbf{w} : \left[\mu \left\{ \nabla \mathbf{u} + (\nabla \mathbf{u})^{\intercal} \right\} + \lambda \left(\nabla \cdot \mathbf{u} \right) \mathbf{I} \right] \, d\mathbf{x} \\
&+ \int_{\Omega_{\text{PML}}} \nabla \mathbf{w} : \left(\dot{\mathbf{S}}^{\intercal} \boldsymbol{\Lambda}_e + \mathbf{S}^{\intercal} \boldsymbol{\Lambda}_p \right) \, d\mathbf{x} \\
&+ \int_{\Omega_{\text{PML}}} \mathbf{w} \cdot \left(\mathsf{a} \ddot{\mathbf{u}} + \mathsf{b} \dot{\mathbf{u}} + \mathsf{c} \mathbf{u} \right) \, d\mathbf{x} \\
&= \int_{\Omega_{\text{REG}}} \mathbf{w} \cdot \mathbf{f} \, d\mathbf{x}
\end{aligned}
\tag{2.20}
$$

and

$$\begin{aligned}
&\int_{\Omega_{\mathrm{PML}}} \mathbf{T} : \left(\mathsf{a}\ddot{\mathbf{S}} + \mathsf{b}\dot{\mathbf{S}} + \mathsf{c}\mathbf{S}\right)\, d\mathbf{x} \\
=&\int_{\Omega_{\mathrm{PML}}} \mathbf{T} : \mu\left[(\nabla\dot{\mathbf{u}})\,\boldsymbol{\Lambda}_e + \boldsymbol{\Lambda}_e\,(\nabla\dot{\mathbf{u}})^{\intercal} + (\nabla\mathbf{u})\,\boldsymbol{\Lambda}_p + \boldsymbol{\Lambda}_p\,(\nabla\mathbf{u})^{\intercal}\right]\, d\mathbf{x} \\
+&\int_{\Omega_{\mathrm{PML}}} \mathbf{T} : \lambda\left[\nabla\cdot(\boldsymbol{\Lambda}_e\dot{\mathbf{u}}) + \nabla\cdot(\boldsymbol{\Lambda}_p\mathbf{u})\right]\mathbf{I}\, d\mathbf{x},
\end{aligned} \tag{2.21}$$

where $\mathbf{w}(\mathbf{x})$, and $\mathbf{T}(\mathbf{x})$ are admissible vector-valued and tensor-valued test functions, respectively. In order to solve equations (2.20) and (2.21) numerically, we approximate $\mathbf{u}(\mathbf{x},t)$, $\mathbf{w}(\mathbf{x})$, $\mathbf{S}(\mathbf{x},t)$, and $\mathbf{T}(\mathbf{x})$, per:

$$\mathbf{u}_h(\mathbf{x},t) = \begin{bmatrix} \boldsymbol{\Phi}^{\intercal}(\mathbf{x})\ \mathbf{u}_x(t) \\ \boldsymbol{\Phi}^{\intercal}(\mathbf{x})\ \mathbf{u}_y(t) \end{bmatrix} \tag{2.8a}$$

$$\mathbf{w}_h(\mathbf{x}) = \begin{bmatrix} \boldsymbol{\Phi}^{\intercal}(\mathbf{x})\ \mathbf{w}_x \\ \boldsymbol{\Phi}^{\intercal}(\mathbf{x})\ \mathbf{w}_y \end{bmatrix} \tag{2.8b}$$

$$\mathbf{S}_h(\mathbf{x},t) = \begin{bmatrix} \boldsymbol{\Psi}^{\intercal}(\mathbf{x})\mathbf{S}_{xx}(t) & \boldsymbol{\Psi}^{\intercal}(\mathbf{x})\mathbf{S}_{xy}(t) & \boldsymbol{\Psi}^{\intercal}(\mathbf{x})\mathbf{S}_{xz}(t) \\ \boldsymbol{\Psi}^{\intercal}(\mathbf{x})\mathbf{S}_{yx}(t) & \boldsymbol{\Psi}^{\intercal}(\mathbf{x})\mathbf{S}_{yy}(t) & \boldsymbol{\Psi}^{\intercal}(\mathbf{x})\mathbf{S}_{yz}(t) \\ \boldsymbol{\Psi}^{\intercal}(\mathbf{x})\mathbf{S}_{zx}(t) & \boldsymbol{\Psi}^{\intercal}(\mathbf{x})\mathbf{S}_{zy}(t) & \boldsymbol{\Psi}^{\intercal}(\mathbf{x})\mathbf{S}_{zz}(t) \end{bmatrix} \tag{2.22a}$$

$$\mathbf{T}_h(\mathbf{x}) = \begin{bmatrix} \boldsymbol{\Psi}^{\intercal}(\mathbf{x})\mathbf{T}_{xx} & \boldsymbol{\Psi}^{\intercal}(\mathbf{x})\mathbf{T}_{xy} & \boldsymbol{\Psi}^{\intercal}(\mathbf{x})\mathbf{T}_{xz} \\ \boldsymbol{\Psi}^{\intercal}(\mathbf{x})\mathbf{T}_{yx} & \boldsymbol{\Psi}^{\intercal}(\mathbf{x})\mathbf{T}_{yy} & \boldsymbol{\Psi}^{\intercal}(\mathbf{x})\mathbf{T}_{yz} \\ \boldsymbol{\Psi}^{\intercal}(\mathbf{x})\mathbf{T}_{zx} & \boldsymbol{\Psi}^{\intercal}(\mathbf{x})\mathbf{T}_{zy} & \boldsymbol{\Psi}^{\intercal}(\mathbf{x})\mathbf{T}_{zz} \end{bmatrix} \tag{2.22b}$$

Upon introduction of the above approximants, there results the following semi-discrete equation:

$$\mathbf{M}\ddot{\mathbf{u}}(t) + \mathbf{C}\dot{\mathbf{u}}(t) + \mathbf{K}\mathbf{u}(t) = \mathbf{f}(t). \tag{2.23}$$

The definitions of matrices $\mathbf{M}$, $\mathbf{C}$, $\mathbf{K}$, and vector $\mathbf{f}$ are provided in Appendix

A.1; the time integration is done using the RK4 procedure described in Appendix B.1.

2.2.5.2 Motion metrics for assessing wave focusing

In order to evaluate the quality of the refocus, we use the motion metrics defined in Karve et al. [33] and Koo et al. [37]. We denote the instantaneous kinetic energy in the target inclusion by $\mathrm{KE}_{\mathrm{inc}}(t)$, and the estimated amount of energy expended at the TRM on the ground surface by $\mathrm{E}_{\mathrm{input}}$; they are defined, respectively, as:

$$\mathrm{KE}_{\mathrm{inc}}(t) = \frac{1}{2}\int_{\Omega_{\mathrm{inc}}} \dot{u}(\mathbf{x},t)\rho(\mathbf{x})\dot{u}(\mathbf{x},t)\,d\mathbf{x} = \frac{1}{2}\mathbf{u}^{\intercal}(t)\mathbf{M}_{\mathrm{inc}}\mathbf{u}(t), \tag{2.24}$$

$$\mathrm{E}_{\mathrm{input}} = \int_0^T \int_{\Gamma^{\mathrm{TRM}}} f(\mathbf{x},t)\dot{u}(\mathbf{x},t)\,d\mathbf{x}\,dt = \int_0^T \mathbf{f}^{\intercal}(t)\dot{\mathbf{u}}(t)\,dt, \tag{2.25}$$

where $\mathbf{M}_{\mathrm{inc}}$ is the target's mass matrix.

We define the time-averaged kinetic energy at the target as:

$$\mathrm{KE}_{\mathrm{inc}}^{\mathrm{TA}} = \frac{1}{T_2 - T_1}\int_{T_1}^{T_2} \mathrm{KE}_{\mathrm{inc}}(t)\,dt, \tag{2.26}$$

where T_1 and T_2 correspond to the instant of the first wave arrival at the target and the instant of the last wave packet leaving the target, respectively. Using (2.24), (2.25), and (2.26), we define the ratio of $\mathrm{KE}_{\mathrm{inc}}^{\mathrm{TA}}/\mathrm{E}_{\mathrm{input}}$ to evaluate how much of the input energy from the ground surface is delivered to the target; the latter is a measure of efficiency.

In addition, we define:

$$\mathrm{KE}^{\mathrm{TA}}(\mathbf{x}) = \frac{1}{2T}\int_0^T \mathbf{u}^{\intercal}(\mathbf{x},t)\rho(\mathbf{x})\mathbf{u}(\mathbf{x},t)\,dt \tag{2.27}$$

to assist in the visual assessment of focusing.

2.2.5.3 Experiment 1 - A series of rectangular pulses

A typical wave energy focusing application (e.g., wave-based EOR) calls for a sustained stress wave stimulation of the target zone. Such stimulation can be delivered by designing the wave sources using a series of rectangular pulses in the forward step of the TR method, e.g., the comb-like signal depicted in Figure 2.13a. The frequency spectrum of the comb-like signal is shown in Figure 2.13b. It can be seen in Fig. 2.13b that the comb-like signal has three dominant frequencies – roughly 14Hz, 28Hz and, 43Hz. In the forward step, we apply a horizontal (x-directional) point load, whose magnitude is described by the comb-like signal, at the center of the target inclusion. We terminate the forward step simulation after 1 second ($T = 1$ second). The time-reversal mirror records the waves emitted by the point load; for example, Figure 2.13c shows the horizontal displacement recorded at coordinates (0,0). All the other surface sensors have their own displacement records. Figure 2.13d shows the frequency spectrum of the displacement recorded at (0,0). It can be seen in Figure 2.13d that the heterogeneous elastic domain reduced the participation of two of the dominant frequencies of the input signal. Next, we time-reverse the recorded signals (Figure 2.13c) and apply horizontal point loads, whose temporal description is given by the time-reversed signals, at the respective sensor locations. Note that in the TR step we amplify the amplitude of the point loads so that the maximum amplitude is 50 kN/m. The rebroadcast waves refocus

at the source location in the forward step, and stimulate the target inclusion. In order to allow the passage of waves from the computational domain, we extend the simulation time for the TR step to 1.5 s (as opposed to 1 s for the forward step). That is, the surface loads remain silent after 1s, and we allow extra 0.5s for the waves to evacuate the semi-infinite domain. The displacement histories at the center of the target inclusion for each mirror density case are depicted in Figure 2.14a and 2.14c, and their frequency spectra are shown in Figure 2.14b and 2.14d respectively. The (horizontal) displacement histories differ only in magnitude, and hence, the (normalized) frequency spectra for the full and quarter density mirror cases are identical. Note that the displacement histories have a single dominant frequency of 14 Hz. Fig. 6 shows the plots of $\mathrm{KE}_{\mathrm{inc}}(t)$ for the two mirror densities. Similar to the displacement histories, the histories of $\mathrm{KE}_{\mathrm{inc}}(t)$ are identical in shape – the difference is in their magnitude. The plots of $\mathrm{KE}^{\mathrm{TA}}(\mathbf{x})$ for the entire domain are depicted in Fig. 7. The contrast between $\mathrm{KE}^{\mathrm{TA}}(\mathbf{x})$ values of the inclusion and its surroundings suggests a good quality refocus. The two figures are almost indistinguishable because their respective time-reversal mirrors have the same size. The mirror density affects the intensity of refocus, but not the quality of refocus — the scale bars on the right are different for the two figures.

The values of the various motion metrics for the full and quarter mirror density cases are summarized in Table 2.2. It can be seen that the ratio of time-averaged kinetic energy of the inclusion to the input energy does not depend on mirror density. For the quarter density mirror case, both $\mathrm{KE}_{\mathrm{inc}}^{\mathrm{TA}}$ and $\mathrm{E}_{\mathrm{input}}$

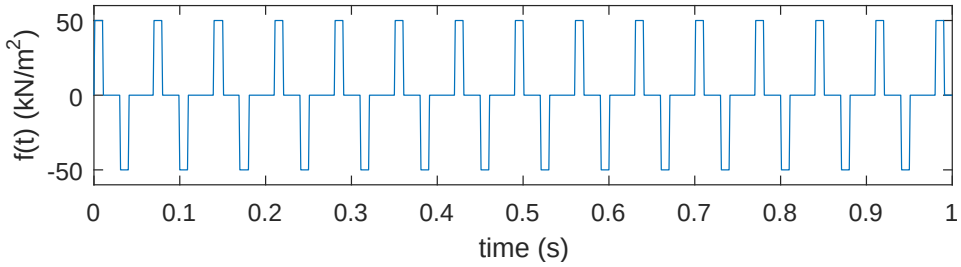

(a) Comb-like source signal

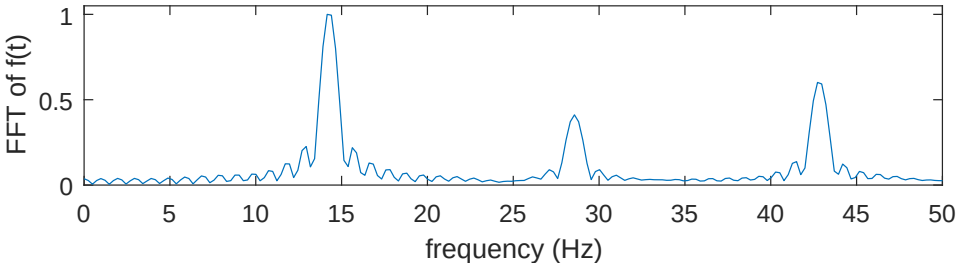

(b) Frequency spectrum of the comb-like signal

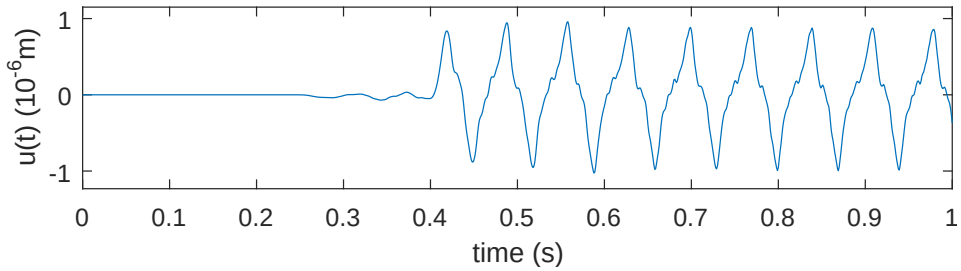

(c) Displacement recorded at (0,0)

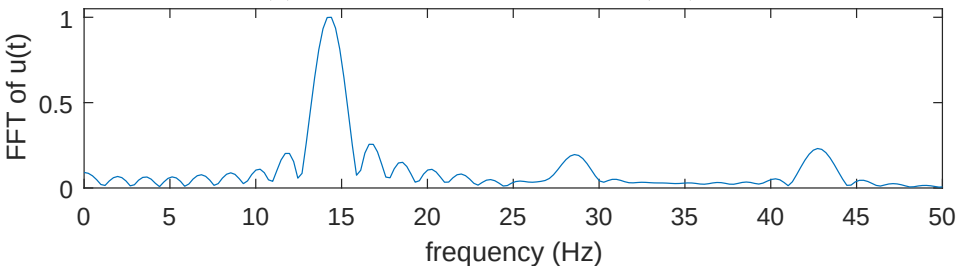

(d) Frequency spectrum of the displacement recorded at (0,0)

Figure 2.13: Time signal of the wave source and displacement recording (forward step) – experiment 1

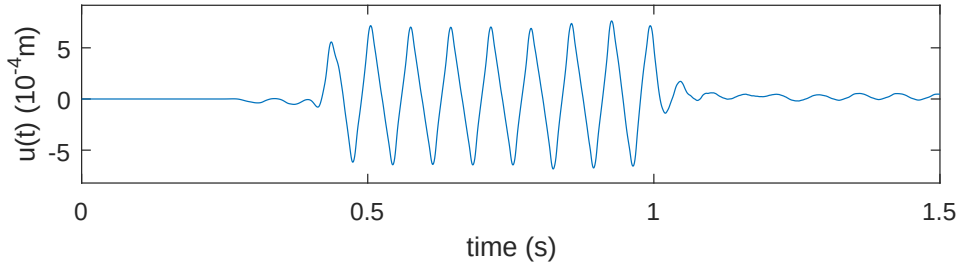

(a) Displacement at target – full mirror

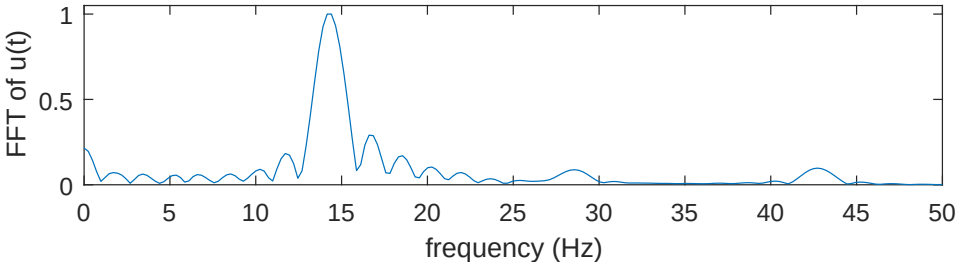

(b) Frequency spectrum of displacement – full mirror

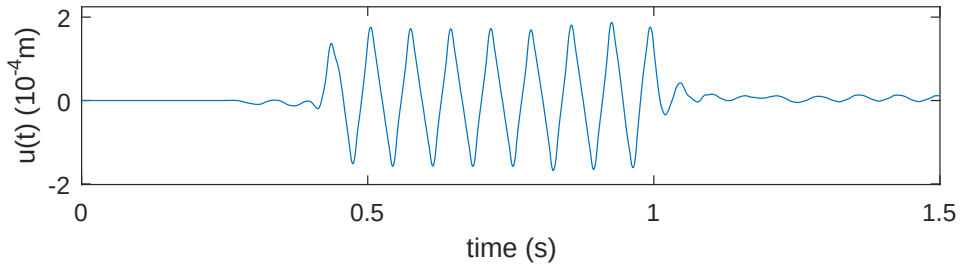

(c) Displacement at target – quarter density mirror

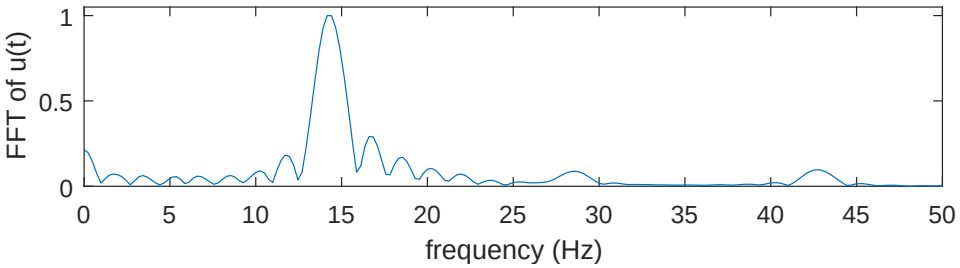

(d) Frequency spectrum of displacement – quarter density mirror

Figure 2.14: Displacements and their frequency spectra of TR step – experiment 1

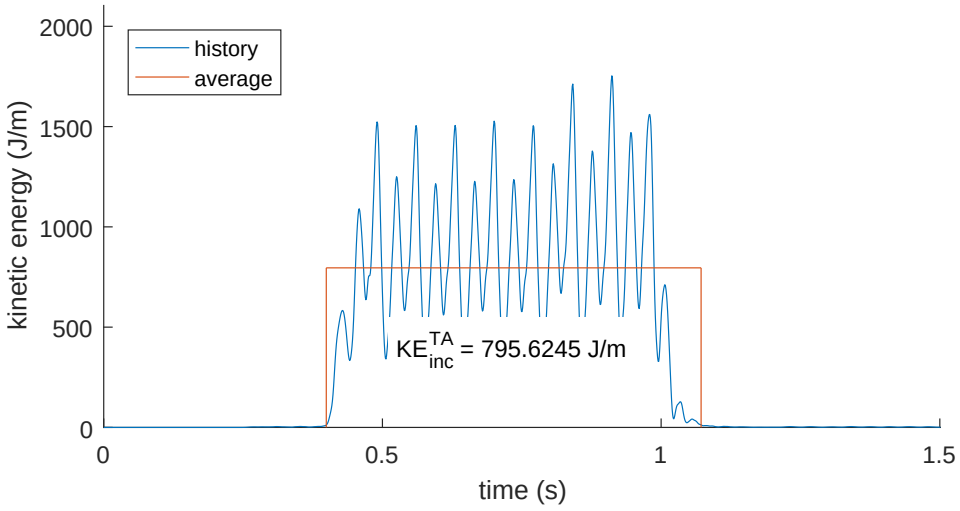

(a) Full mirror

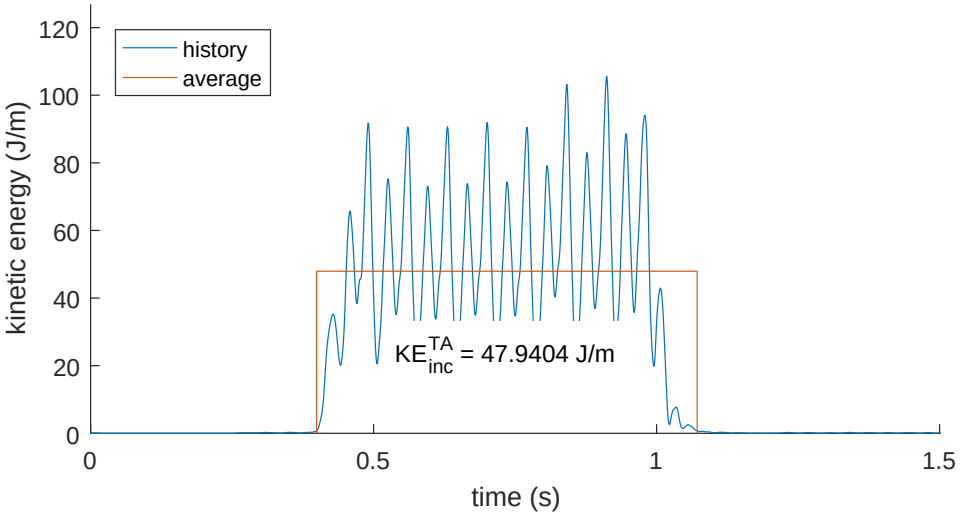

(b) Quarter density mirror

Figure 2.15: Kinetic energy response of inclusion – experiment 1

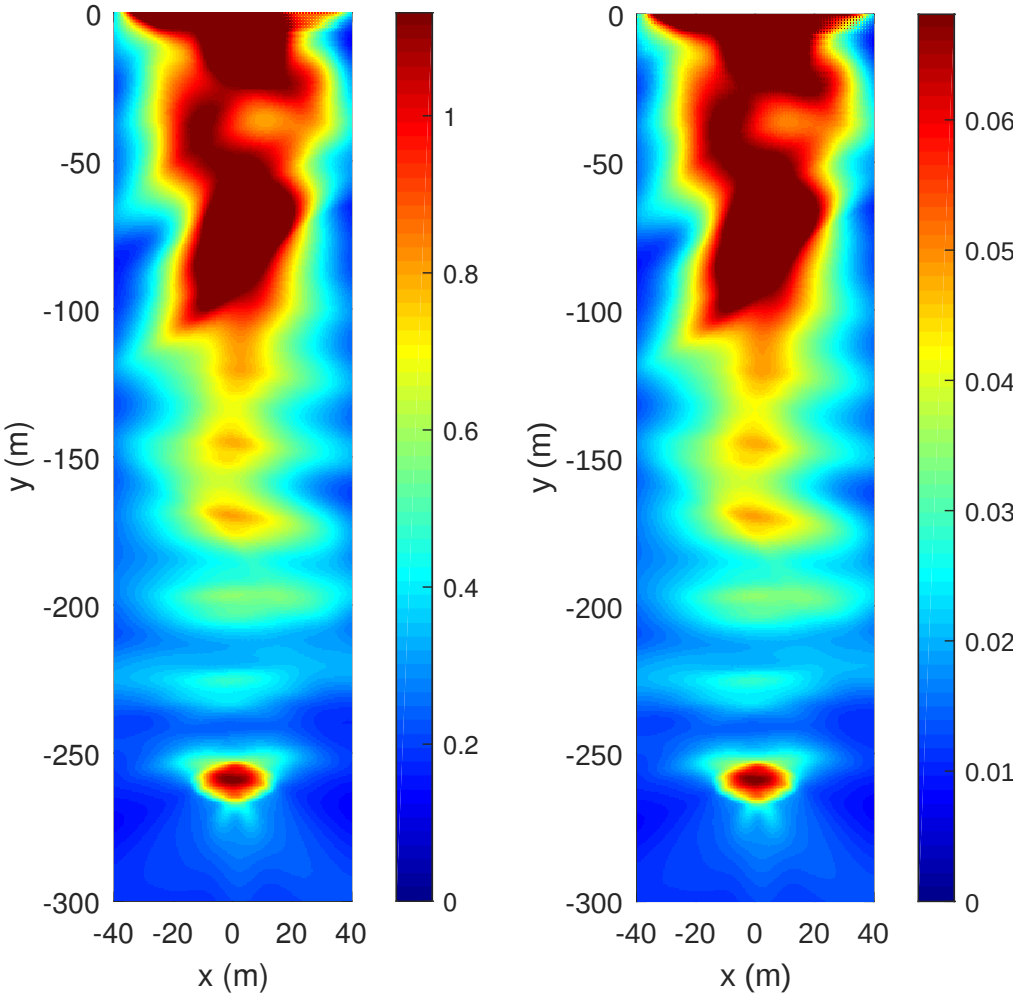

(a) Full mirror (b) Quarter density mirror

Figure 2.16: $\mathrm{KE}^{\mathrm{TA}}(\mathbf{x})$ (J/m^3) after the TR step – experiment 1

Table 2.2: Motion metrics for experiment 1

	Full mirror	Quarter density mirror
$\mathrm{KE}^{\mathrm{TA}}_{\mathrm{inc}}$ (J/m)	4.2197×10^{2}	2.5424×10^{1}
$\mathrm{E}_{\mathrm{input}}$ (J/m)	8.1094×10^{4}	4.9730×10^{3}
$\mathrm{KE}^{\mathrm{TA}}_{\mathrm{inc}}/\mathrm{E}_{\mathrm{input}}$	5.2034×10^{-3}	5.1126×10^{-3}

are reduced by a factor of $\frac{1}{16}$ as compared to those values for the full mirror density case. This observation agrees well with the experiments reported in [3, 42, 57], and provides a validation for our numerical surrogate procedure for the TR method. We conclude that for semi-infinite elastic media, reducing the number of sensors on time-reversal mirror only affects the energy intensity of refocus and not the quality of refocus, as long as the TRM aperture remains the same.

2.2.5.4 Experiment 2 - A modified Ricker pulse

In the preceding experiment, the comb-like source signal used in the forward step (Figure 2.13a) was merely a guess. The comb-like signal had three dominant frequencies (14Hz, 28Hz, and 43Hz) in its spectrum, and the forward step filtered two of them out. In the TR step, we rebroadcast the near-monochromatic signal and achieved a good quality refocus as seen in Figure 2.16. Thus, the forward step acted as a filter and selected the frequencies that help illuminate the target inclusion. It has been reported [30, 33] that the kinetic energy of target elastic inclusions embedded in layered, heterogeneous, semi-infinite elastic domains can be maximized if the sources operate at one of the amplification frequencies of the formation. The amplification frequency can be determined by conducting a frequency sweep.[2] Thus, if the amplification

[2]In a frequency sweep, a numerical model of the governing wave physics is used to compute a predefined motion metric of the target for a range of monochromatic frequencies driving the sources. The frequency corresponding to the maximum value of the motion metric is termed the amplification frequency [30, 33].

frequency of the target is present in the time signal of the forward step, then the displacements recorded by the TR mirror should show a bias. Typically, the amplification frequency of the target is not known *a priori*. Hence, a blindly chosen continuous wave (CW)-like (narrow band) signal may not contain the amplification frequency in its spectrum. This is a key drawback of using CW-like signals in the forward step. Consequently, a broadband signal may be more suitable for use in the forward step. In this experiment, we explore this possibility by using a modified Ricker pulse as a candidate broadband signal. The equation defining the modified Ricker pulse is given by

$$f(t) = \left[1 - 2\pi^2 f_0^2 \left(t-1\right)^2\right] e^{-\pi^2 f_0^2 (t-1)^2}, \tag{2.28}$$

where f_0 is the central frequency of the modified Ricker pulse. Here, we choose $f_0 = 25$ Hz (Figure 2.17a), without knowing the amplification frequency of the model (Figure 2.12) we are dealing with. Karve et al. [33] conducted the frequency sweep for the geological formation model shown in Figure 2.12, and reported that for horizontally polarized surface loads the amplification frequency is (approximately) 18 Hz. It can be seen from Figure 2.17b that the amplification frequency (18 Hz) is present in the spectrum of the forward step signal. We send the modified Ricker signal from the inclusion and record the displacements on the ground surface. A closer look at the frequency spectrum of the input signal (Figure 2.17b) and that of the recorded displacement (Figure 2.17c) reveals that the peak of the spectrum is shifted from 25 Hz to around 18 Hz. We time-reverse the recorded displacements and rebroadcast from their

Table 2.3: Motion metrics for experiments 1 and 2

	Full mirror	Quarter density mirror
KE_{inc}^{TA} (J/m)	2.6517×10^{2}	1.6084×10^{1}
E_{input} (J/m)	9.6943×10^{3}	5.9528×10^{2}
KE_{inc}^{TA}/E_{input} (modified Ricker)	2.7353×10^{-2}	2.7019×10^{-2}
KE_{inc}^{TA}/E_{input} (comb-like)	5.2034×10^{-3}	5.1126×10^{-3}

respective locations in the TR step. Figure 2.17e shows the displacement history at the center of the inclusion in the TR step. It can be seen that the peak of the frequency spectrum of the TR displacement (Figure 2.17f) is further sharpened. The bias towards the amplification frequency is clearly evident. The values of other motion metrics for the modified Ricker pulse as well as the comb-like signal are given in Table 2.3. The ratios of KE_{inc}^{TA} to E_{input} for the case of the modified Ricker pulse are about five times greater than those for the case of the comb-like signal. We conclude that a broadband signal (especially, a signal that contains the amplification frequency in its spectrum) enhances the ability of the TR process and increases the efficiency of wave energy delivery (Figure 2.18).

2.3 Summary

We investigated the validity of the TR method for wave focusing in two-dimensional elastic, heterogeneous, and semi-infinite media, with an eye towards an application in enhanced oil recovery. Beginning from the ideal case of section 2.1 describing the TR concept for a closed cavity, we incremen-

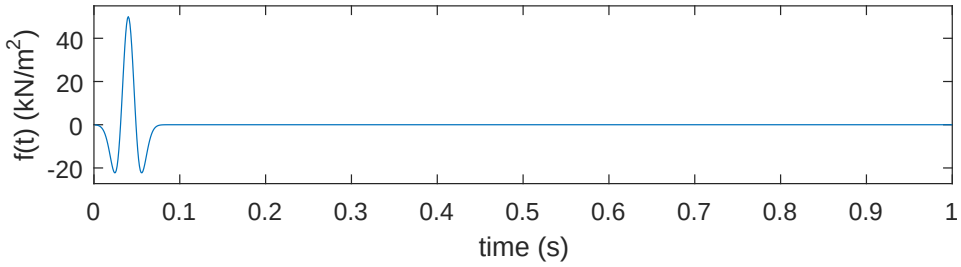

(a) Modified Ricker pulse

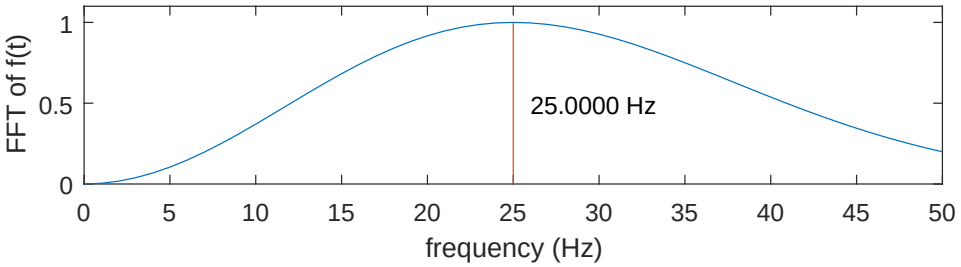

(b) Frequency spectrum of the modified Ricker pulse

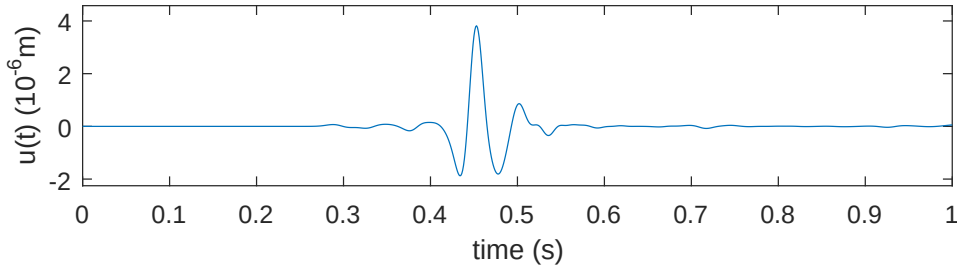

(c) Displacement recorded at (0,0)

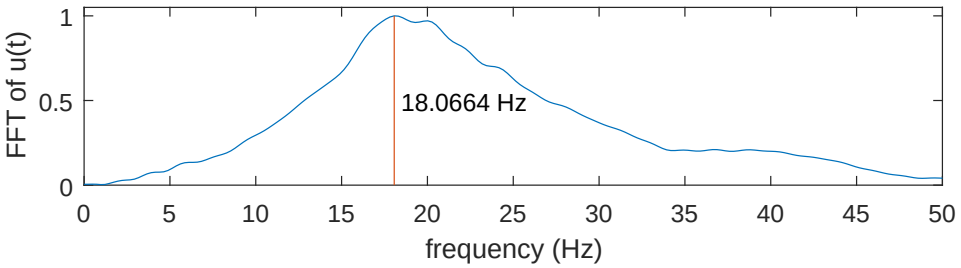

(d) Frequency spectrum of the displacement recorded at (0,0)

Figure 2.17: continued in the next page

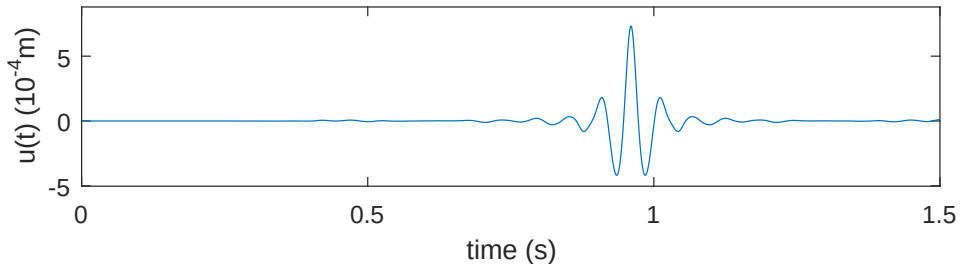

(e) Displacement at the center of the target inclusion

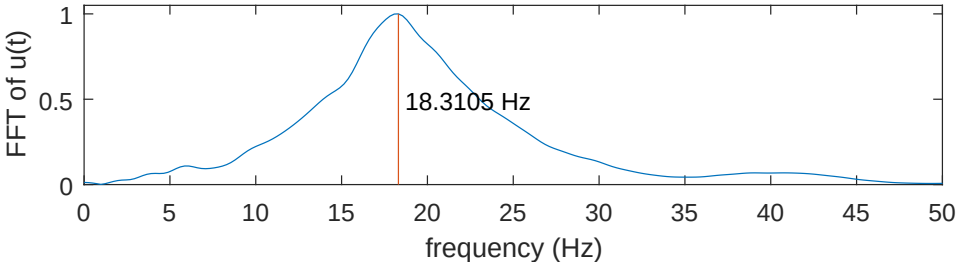

(f) Frequency spectrum of the displacement

Figure 2.17: Time signal of the wave source, the displacement recording of TRM, and the displacement of focused waves – experiment 2

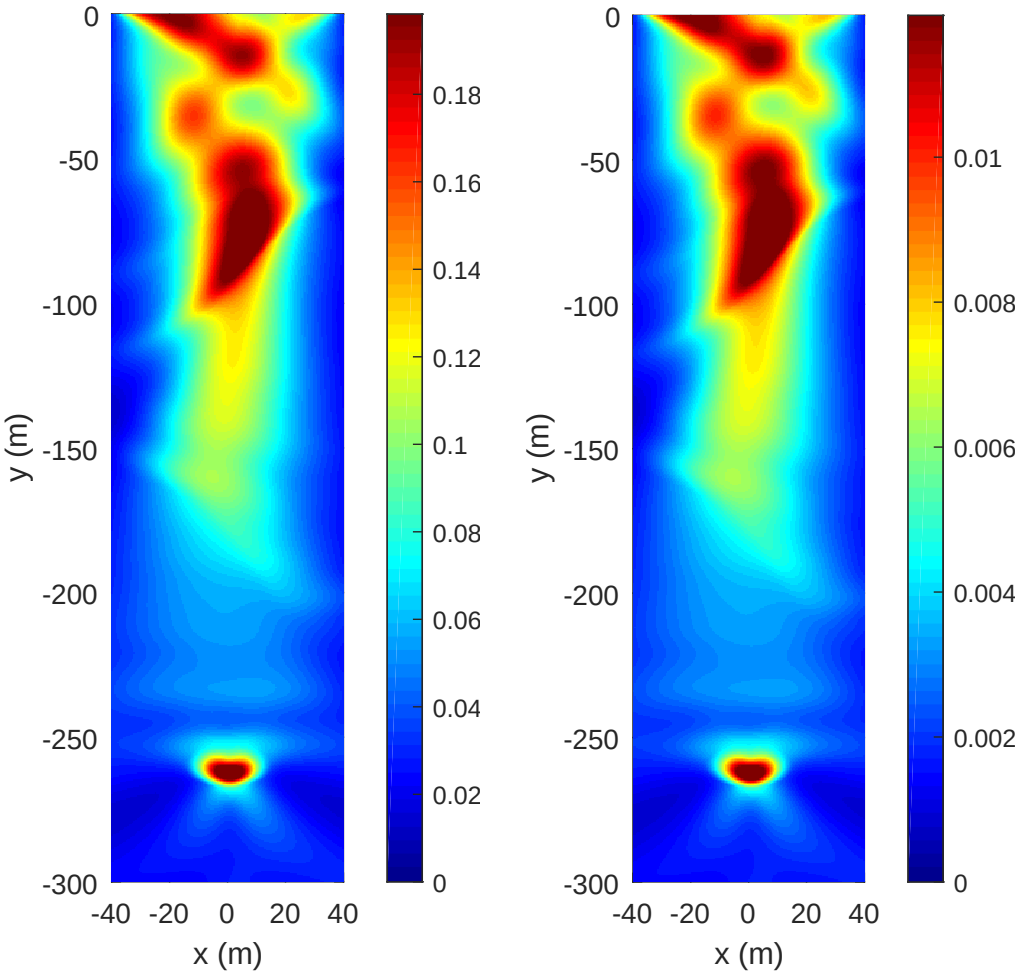

(a) Full mirror (b) Quarter density mirror

Figure 2.18: KE_{TA} (J/m^3) after the TR step – experiment 2

tally relaxed various physically unrealizable conditions, to arrive at the setting mandated by a potential field TR method implementation. From the series of numerical experiments we conducted, we observed that the focus quality degrades, as we depart from the ideal conditions, but, nevertheless, there is still focusing, albeit spatially dispersed. For the driving application, this may be more beneficial than disadvantageous.

Of all effects studied, the greatest degradation of the focusing resolution is due to the D-to-N flipping. We discuss next the reasons for the resolution loss, and seek potential improvements.

Chapter 3

The D-to-N flipping ramifications - Resolution control

In Chapter 2, we identified that, among all of the physically unrealizable conditions for a practical TR field implementation, the one that affects the focusing resolution the most is, what we termed, the D-to-N flipping. The D-to-N flipping had a smearing effect: the focusing loses sharpness, and the high intensity field in the vicinity of the target is spatially extended. In Chapter 2, the D-to-N flipping was shown computationally; here, we provide the mathematical background that explains the loss of resolution. We also offer a filter that can be applied to the TRM data prior to time-reversal, which improves the resolution, and, in fact, restores it to optimal levels. [1] The development is predicated on the scalar wave equation; an extension to the elastodynamic case is not available at this point.

We have already seen that time-reversing the Dirichlet data as Dirichlet (D-to-D) results in perfect focusing, especially in the case of a closed-cavity.

[1] A part of this chapter has been published as: H. Goh, S. Koo and L. F. Kallivokas. Resolution Control in Half-space Time-reversal Wave Focusing, *Proc. The 13th International Conference on Mathematical and Numerical Aspects of Wave Propagation*, 2017, [27]. The authors of the proceedings paper formulated the underlying mathematical problem and wrote a computer program to resolve it.

Thus, our interest is in establishing a relation between the wavefield that results when at the TRM we time-reverse the Dirichlet data and impose them as a Dirichlet condition (D-to-D), and the wavefield that results when at the TRM we time-reverse the Dirichlet data and impose them as a Neumann condition (D-to-N). Henceforth, we denote the D-to-D wavefield as $u_D(x,t)$, and the D-to-N wavefield as $u_N(x,t)$, and we first seek to establish a relation between them.

3.1 D-to-N flipping in 1D

To fix ideas, we consider the one-dimensional domain shown in Fig. 3.1: the domain extends from $x = 0$ to $x = L$, with the left end being free and the right end being terminated by a dashpot. The domain, though truncated, is an exact representation of a semi-infinite domain, owing to the dashpot condition at L. We assume that a source, or a non-vanishing initial condition, has generated a wavefield in the domain, and that the resulting motion - the Dirichlet datum - (e.g., displacement history) has been recorded at $x = 0$. We denote the recording as $p(t)$ (effectively, the TRM is at $x = 0$). We remark that it is without loss of generality that we are indifferent to the specifics of the source that generated the wavefield in the domain.

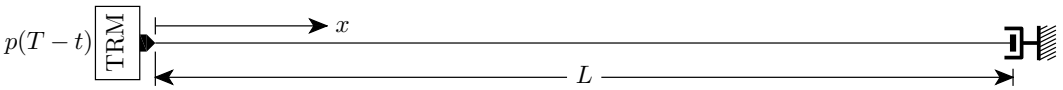

Figure 3.1: 1D semi-infinite domain; TRM is installed at $x = 0$; domain is truncated at $x = L$ with a radiation condition

First, we are interested in obtaining the solution to the D-to-D case when $p(t)$ is time-reversed at $x = 0$, i.e., when the Dirichlet data are time-reversed and imposed as Dirichlet data. The associated initial- and boundary-value problem reads: find $u_D(x,t)$, such that:

Problem 1: D-to-D

$$\begin{aligned}
\frac{\partial^2 u_D}{\partial x^2} - \frac{1}{c^2}\frac{\partial^2 u_D}{\partial t^2} &= 0, && 0 < x < L, \quad 0 < t \leqslant T \\
u_D(0,t) &= p(T-t), && 0 < t \leqslant T \\
\frac{\partial u_D}{\partial x}(x,t) &= -\frac{1}{c}\frac{\partial u_D}{\partial t}(x,t), && x = L, \quad 0 < t \leqslant T \\
u_D(x,0) &= 0, && 0 < x < L \\
\frac{\partial u_D}{\partial t}(x,0) &= 0, && 0 < x < L
\end{aligned} \tag{3.1}$$

We Fourier transform the governing equation (3.1) to obtain:

$$\frac{\partial^2 \hat{u}_D}{\partial x^2} + \frac{\omega^2}{c^2}\hat{u}_D = 0, \qquad 0 < x < L \tag{3.2}$$

The Fourier transform of the TRM boundary condition at $x = 0$ reads:

$$\hat{u}_D(0,\omega) = \hat{p}^*(\omega) \tag{3.3}$$

where an asterisk indicates complex conjugate. The full-space Green's function of the one-dimensional Helmholtz equation is:

$$g(\xi;x) = -\frac{ie^{i\frac{\omega}{c}|\xi - x|}}{2\frac{\omega}{c}} \tag{3.4}$$

When the domain of interest reduces to semi-infinite with a Dirichlet condition at $x = 0$, the corresponding Green's function can be shown to be:

$$g_D(\xi;x) = g(\xi;x) - g(\xi;-x). \tag{3.5}$$

Using (3.5), the solution to the equation (3.2) with the boundary condition (3.3) becomes:

$$\begin{aligned}\hat{u}_D(x,\omega) &= -\left[\frac{\partial g_D}{\partial \xi}(\xi;x)\hat{p}^*(\omega)\right]_{\xi=0} \\ &= -\left[\frac{\partial g}{\partial \xi}(\xi;x) - \frac{\partial g}{\partial \xi}(\xi;-x)\right]\hat{p}^*(\omega)\Big|_{\xi=0} \\ &= -2\frac{\partial g}{\partial \xi}(0;x)\hat{p}^*(\omega), \end{aligned} \tag{3.6}$$

or

$$\hat{u}_D(x,\omega) = -e^{i\frac{\omega}{c}x}\hat{p}^*(\omega). \tag{3.7}$$

Next, we turn our attention to the solution of the D-to-N case when $p(t)$ is time-reversed at $x = 0$ as Neumann data. The associated initial- and boundary-value problem reads: find $u_N(x,t)$, such that:

Problem 2: D-to-N

$$\begin{aligned} \frac{\partial^2 u_N}{\partial x^2} - \frac{1}{c^2}\frac{\partial^2 u_N}{\partial t^2} &= 0, && 0 < x < L, \quad 0 < t \leqslant T \\ \frac{\partial u_N}{\partial t}(0,t) &= p(T-t), && 0 < t \leqslant T \\ \frac{\partial u_n}{\partial x}(x,t) &= -\frac{1}{c}\frac{\partial u_N}{\partial t}(x,t), && x = L, \quad 0 < t \leqslant T \\ u_N(x,0) &= 0, && 0 < x < L \\ \frac{\partial u_N}{\partial t}(x,0) &= 0, && 0 < x < L \end{aligned} \tag{3.8}$$

The solution to the D-to-N problem is obtained in a manner analogous to the D-to-D problem. We Fourier transform the governing equation (3.8) to obtain:

$$\frac{\partial^2 \hat{u}_N}{\partial x^2} + \frac{\omega^2}{c^2}\hat{u}_N = 0, \qquad 0 < x < L. \tag{3.9}$$

The Fourier transform of the TRM boundary condition at $x = 0$ reads:

$$\frac{\partial \hat{u}_N}{\partial x}(0, \omega) = \hat{p}^*(\omega). \tag{3.10}$$

When the semi-infinite domain is subjected to a Neumann condition at $x = 0$, the corresponding Green's function can be shown to be:

$$g_N(\xi; x) = g(\xi; x) + g(\xi; -x). \tag{3.11}$$

Using (3.11), the solution to the equation (3.9) with boundary condition (3.10) becomes:

$$\begin{aligned} \hat{u}_N(x, \omega) &= -\left[g_N(\xi; x)\hat{p}^*(\omega)\right]_{\xi=0} \\ &= -\left[g(\xi; x) + g(\xi; -x)\right]\hat{p}^*(\omega)\big|_{\xi=0} \\ &= -2g(0; x)\hat{p}^*(\omega), \end{aligned} \tag{3.12}$$

or

$$\hat{u}_N(x, \omega) = \frac{ie^{i\frac{\omega}{c}x}}{\frac{\omega}{c}}\hat{p}^*(\omega). \tag{3.13}$$

Thus, the relation in the frequency domain between the two time-reversed wavefields u_D and u_N is easily deduced from (3.7) and (3.13) to be:

$$\hat{u}_D(x, \omega) = \frac{\partial \hat{u}_N}{\partial x}(x, \omega) \tag{3.14}$$

or, in the time-domain:

$$u_D(x, t) = \frac{\partial u_N}{\partial x}(x, t) \tag{3.15}$$

Thus, $u_D(x,t)$ is the derivative of $u_N(x,t)$, or conversely, $u_N(x,t)$ is the integral of the wavefield $u_D(x,t)$. Assuming the TRM data were obtained by a sharp source event, $u_D(x,t)$ will offer sharp resolution, but its integral ($u_N(x,t)$) will result in spatial smearing. This is the reason for the resolution degradation in the D-to-N case.

3.2 D-to-N flipping in 2D and 3D

Next, we extend the 1D ideas to higher dimensions (Fig. 3.2). The corresponding D-to-D and D-to-N problems read:

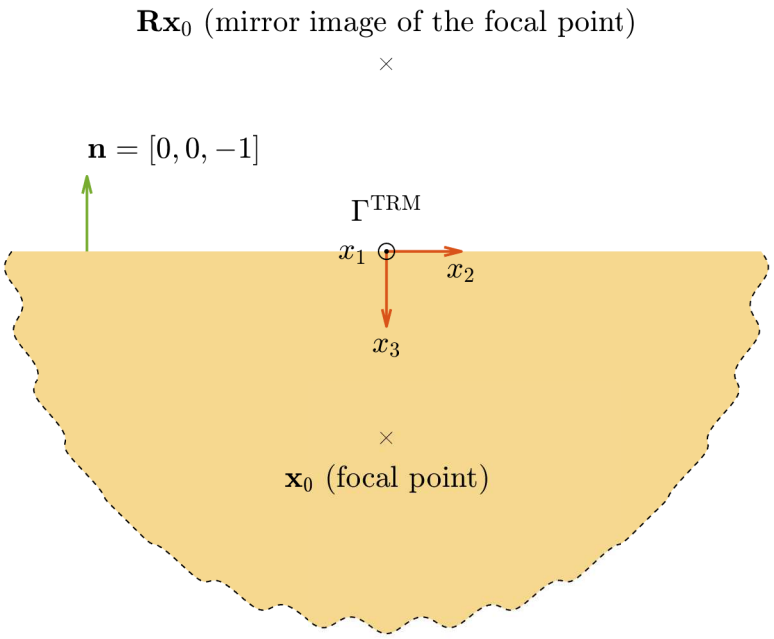

Figure 3.2: 3D semi-infinite domain

Problem 1: D-to-D

$$\begin{aligned}
\Delta u_D - \frac{1}{c^2}\frac{\partial^2 u_D}{\partial t^2} &= 0, && \mathbf{x} \in \Omega,\ 0 < t \leqslant T \\
u_D(\mathbf{x}, t) &= p(\mathbf{x}, T-t), && \mathbf{x} \in \Gamma^{\mathrm{TRM}},\ 0 < t \leqslant T \\
u_D(\mathbf{x}, 0) &= 0, && \mathbf{x} \in \Omega \\
\frac{\partial u_D}{\partial t}(\mathbf{x}, 0) &= 0, && \mathbf{x} \in \Omega,
\end{aligned} \tag{3.16}$$

subject also to the Sommerfeld radiation condition as $|\mathbf{x}| \to \infty$. Similarly:

Problem 2: *D to N*

$$\begin{aligned}
\Delta u_N - \frac{1}{c^2}\frac{\partial^2 u_N}{\partial t^2} &= 0, && \mathbf{x} \in \Omega,\ 0 < t \leqslant T \\
\frac{\partial u_N}{\partial x_3}(\mathbf{x}, t) &= p(\mathbf{x}, T-t), && \mathbf{x} \in \Gamma^{\mathrm{TRM}},\ 0 < t \leqslant T \\
u_N(\mathbf{x}, 0) &= 0, && \mathbf{x} \in \Omega \\
\frac{\partial u_N}{\partial t}(\mathbf{x}, 0) &= 0, && \mathbf{x} \in \Omega,
\end{aligned} \tag{3.17}$$

subject also to the Sommerfeld radiation condition as $|\mathbf{x}| \to \infty$.

In the above $\mathbf{x} = (x_1, x_2, x_3)$ per Fig. 3.2. By taking Fourier transforms on (3.16) with respect to t, x_1, and x_2, the equation reduces to the one-dimensional Helmholtz equation:

$$\frac{\partial^2 \hat{u}_D}{\partial x_3^2} + \left(\frac{\omega^2}{c^2} - k_1^2 - k_2^2\right)\hat{u}_D = 0, \qquad x_3 > 0$$

or, by introducing α as:

$$\alpha^2 = \frac{\omega^2}{c^2} - k_1^2 - k_2^2,$$

(3.2) can be further simplified to:

$$\frac{\partial^2 \hat{u}_D}{\partial x_3^2} + \alpha^2 \hat{u}_D = 0, \qquad x_3 > 0 \tag{3.18}$$

With the aid of the one-dimensional solution of the preceding section, the solution to the D-to-D case (3.16) is analogous to (3.6), i.e.:

$$\begin{aligned}\hat{u}_D(x_3,\alpha) &= -\left.\frac{\partial g_D}{\partial \xi}(\xi;x_3)\hat{p}^*(x_3,\alpha)\right|_{\xi=0} \\ &= -\left[2\frac{\partial g}{\partial \xi}(\xi,x_3)\hat{p}^*(x_3,\alpha)\right]_{\xi=0} \\ &= -e^{i\alpha x_3}\hat{p}^*(x_3,\alpha). \end{aligned} \tag{3.19}$$

Similarly, the solution to the D-to-N case (3.17) becomes:

$$\begin{aligned}\hat{u}_N(x_3,\alpha) &= -\left[g_N(\xi,x_3)\hat{p}^*(x_3,\alpha)\right]_{\xi=0} \\ &= -\left[2g(\xi,x_3)\hat{p}^*(x_3,\alpha)\right]_{\xi=0} \qquad (3.20) \\ &= \frac{ie^{i\alpha x_3}}{\alpha}\hat{p}^*(x_3,\alpha). \qquad (3.21)\end{aligned}$$

Thus, again, the relation between the D-to-D and the D-to-N wavefields is shown to be the same as that of the 1D case, albeit the spatial derivative is taken with respect to the depth coordinate, i.e.:

$$\hat{u}_D(x_3,\alpha) = \frac{\partial \hat{u}_N}{\partial x_3}(x_3,\alpha). \tag{3.22}$$

3.3 Resolution control - filter design

We are interested in restoring, if possible, the resolution of the D-to-N case to the resolution quality attained by the D-to-D case. We are thus concerned with the design of a filter, which, if applied to the TRM data *prior* to time-reversal, it will not lead to the resolution deterioration expected of

the D-to-N case. To design such a filter, we return to the D-to-D and D-to-N wavefields, and express them in terms of integral equations over the TRM boundary. Accordingly:

$$\begin{aligned}\hat{u}_D(\mathbf{x}) = &\int_{\Gamma^{\mathrm{TRM}}} -\frac{\partial g_D}{\partial \xi}(\boldsymbol{\xi},\mathbf{x})\hat{p}^*(\boldsymbol{\xi})\,d\boldsymbol{\xi}\\ \hat{u}_N(\mathbf{x}) = &-\int_{\Gamma^{\mathrm{TRM}}} g_N(\boldsymbol{\xi},\mathbf{x})\hat{p}^*(\boldsymbol{\xi})\,d\boldsymbol{\xi}.\end{aligned}$$

We recall that the diffraction limit of a closed-cavity problem is $\lambda/2$, where λ denotes wavelength. The resolution in the context of the focusing problems at hand is defined as the wavefield support above half-maximum strength. Using the integral equation for $\hat{u}_D$ the wavefield strength for the D-to-D case and for a source located at $\mathbf{x}_0$ is shown in Fig. 3.3a. It can be seen that the resolution is approximately 1.2λ. As it can also be see in Fig. 3.3b, the resolution of the D-to-N case is fairly poor, roughly amounting to 3.8λ.

We would like for the u_N field (D-to-N) to have the resolution of the u_D field (D-to-D), i.e., a λ-level resolution quality. Therefore, we require that:

$$-\int_{\Gamma^{\mathrm{TRM}}} g_N(\boldsymbol{\xi},\mathbf{x})\mathscr{F}\left(p^*(\boldsymbol{\xi})\right)\,d\boldsymbol{\xi} = \int_{\Gamma^{\mathrm{TRM}}} -\frac{\partial g_D}{\partial \xi}(\boldsymbol{\xi},\mathbf{x})p^*(\boldsymbol{\xi})\,d\boldsymbol{\xi} = \hat{u}_D(\mathbf{x})$$

where $\mathscr{F}(\,\cdot\,)$ is the sought filter to be applied on the Dirichlet data prior to being time-reversed as Neumann data. Using the equivalence between $\dfrac{\partial}{\partial x_3}$ and $i\alpha$ in Fourier transform, and (3.22), it can be shown that:

$$\begin{aligned}\hat{u}_D &= \left[2\frac{\partial g}{\partial x_3}(\xi,x_3)\hat{p}^*(x_3,\alpha)\right]_{\xi=0}\\ &= \left[2i\alpha g(x_3,\xi)\hat{p}^*(x_3,\alpha)\right]_{\xi=0}\end{aligned} \tag{3.20}$$

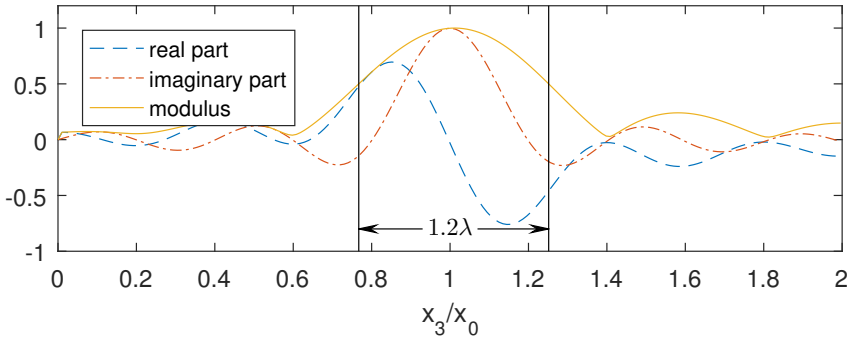

(a) Resolution of u_D (D-to-D)

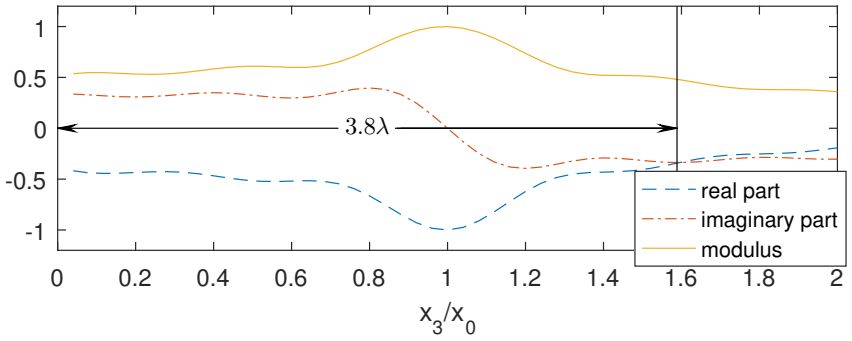

(b) Resolution of u_N (D-to-N)

Figure 3.3: Resolutions of two wavefields along the depth direction for cases D-to-D and D-to-N; $\lambda = 0.4$, $x_1 = x_2 = 0$

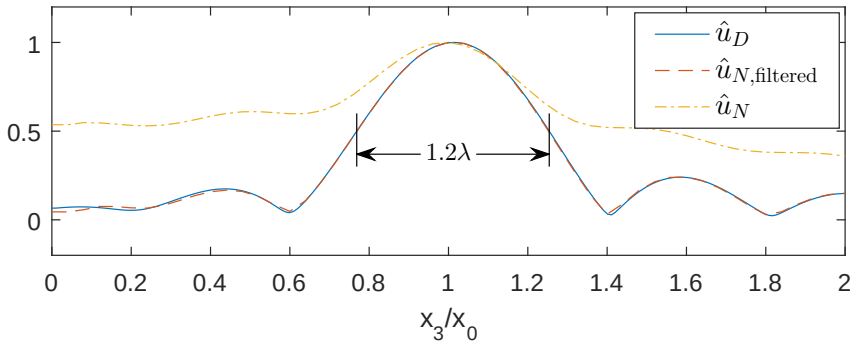

Figure 3.4: Resolution of $\hat{u}_N$ with and without filter $\mathscr{F}(\,\cdot\,)$; $\lambda = 0.4$, $x_1 = x_2 = 0$; $\hat{u}_D$(blue solid) and filtered $\hat{u}_N$(yellow dash-dot)

$$= \left[2g(x_3,\xi)\,(i\alpha\hat{p}^*(x_3,\alpha))\right]_{\xi=0}$$

$$\Rightarrow \mathscr{F}\,(p^*) = \mathcal{F}_{x_1}^{-1}\mathcal{F}_{x_2}^{-1}\left[i\alpha\mathcal{F}_{x_1}\mathcal{F}_{x_2}p^*\right]. \tag{3.23}$$

The filter's (3.23) effect, when applied to the D-to-N case, is shown in Fig. 3.4 where $\hat{u}_D$ and the $\hat{u}_N$ practically overlap with each other. We note that the developed filter addresses a particular case with homogeneous hosts. It serves as an indication that it is possible to improve the resolution of the D-to-N case by suitably filtering the TRM data prior to time-reversing them. A suitable filter for the general elastodynamic case will be the subject of future work.

3.4 Summary

In Chapter 2 we observed computationally the deterioration of the resolution in the D-to-N flipping case. In this Chapter, we offered mathematical evidence for the spatial smearing effect and the loss of resolution. We also designed a resolution-improving filter that can be applied in certain time-reversal

wave focusing applications; the filter is capable of restoring the resolution.

Chapter 4

Time-reversal for wave energy focusing in 3D elastic media

In this Chapter, we report numerical results on the simultaneous energy focusing to multiple subsurface targets embedded in heterogeneous three-dimensional semi-infinite elastic hosts. [1] We use the motion metrics developed in section 2.2.5.2 to assess numerically and visually the efficacy of the TR method to illuminate the targets.

In the following sections, we address first the mathematical formulation and numerical implementation for the three-dimensional TR wave propagation problem at hand. The development follows closely that of Chapter 2 for two-dimensional hosts; however, there are differences stemming from the use of the PMLs at the truncation surfaces that lead to a modified formulation that merits description. Subsequent to the mathematical and numerical treatment, we discuss a series of numerical experiments that provide insight to the requirements for practical field implementation of the TR approach.

[1] A part of this chapter has been published as: S. Koo and L. F. Kallivokas. Wave energy delivery to multiple subsurface targets using time-reversal method, *Proc. The 13th International Conference on Mathematical and Numerical Aspects of Wave Propagation*, 2017, [36]. The author of this dissertation formulated the underlying mathematical problem and wrote a computer program to resolve it.

4.1 Mathematical formulation - TR in 3D

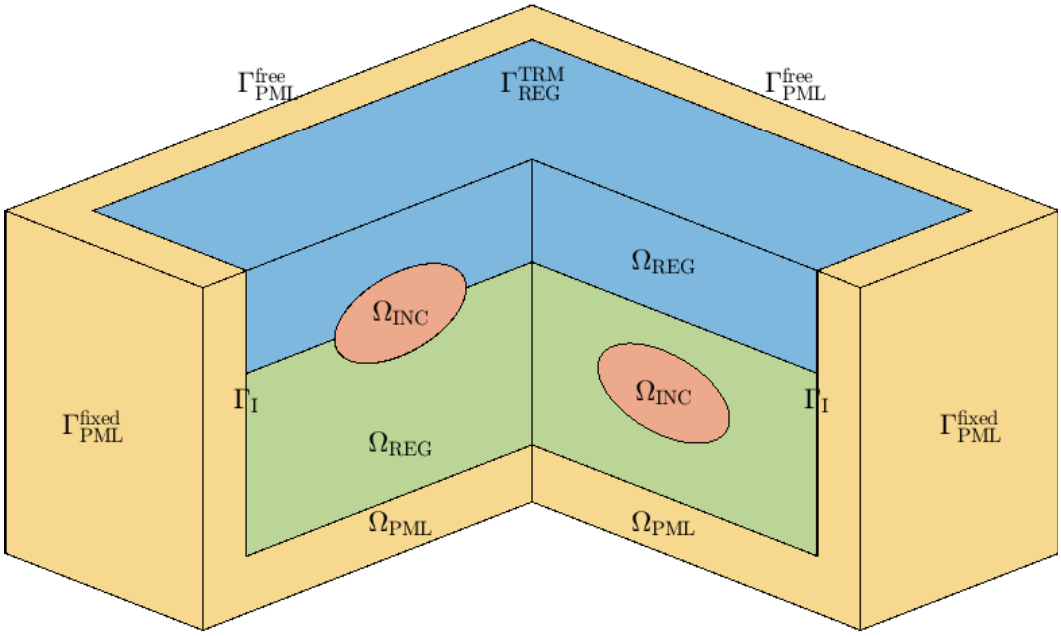

Figure 4.1: Illustration of semi-infinite, heterogeneous, isotropic, and elastic domain having two targets

In this section, we provide the mathematical statement for the TR step in the 3D case. We remark that we relax the same set of conditions that we had relaxed in the 2D case as well: the sink term is eliminated, the TR step is subject to silent initial conditions, and the problem is driven by the D-to-N flipped condition at the TRM. As a result, we expect that the 3D TR case would also suffer from resolution loss, as did the 2D TR case.

The TR wave propagation within the 3D host and the embedded targets, i.e., within Ω_{REG} (Fig. 4.1) is governed by Navier's equation of motion:

$$\rho\, \ddot{\mathbf{v}} - \nabla \cdot [\mu\, \{\nabla \mathbf{v} + (\nabla \mathbf{v})^{\intercal}\} + \lambda\, (\nabla \cdot \mathbf{v})\, \mathbf{I}] = \mathbf{0}, \tag{4.1}$$

where $\mathbf{v}$ denotes the TR wavefield. Similarly, the motion within the PML buffer zone Ω_{PML} is governed by the following equations [23]:

$$\nabla \cdot \left(\ddot{\mathbf{S}}^{\mathsf{T}} \boldsymbol{\Lambda}_e + \dot{\mathbf{S}}^{\mathsf{T}} \boldsymbol{\Lambda}_p + \mathbf{S}^{\mathsf{T}} \boldsymbol{\Lambda}_w \right) = \rho \left(\mathsf{a} \dddot{\mathbf{v}} + \mathsf{b} \ddot{\mathbf{v}} + \mathsf{c} \dot{\mathbf{v}} + \mathsf{d} \mathbf{v} \right), \quad \mathbf{x} \in \Omega_{\text{PML}} \tag{4.2a}$$

$$\begin{aligned} \mathsf{a} \dddot{\mathbf{S}} + \mathsf{b} \ddot{\mathbf{S}} + \mathsf{c} \dot{\mathbf{S}} + \mathsf{d} \mathbf{S} = & \mu \begin{pmatrix} (\nabla \ddot{\mathbf{v}}) \, \boldsymbol{\Lambda}_e + \boldsymbol{\Lambda}_e \, (\nabla \ddot{\mathbf{v}})^{\mathsf{T}} \\ + (\nabla \dot{\mathbf{v}}) \, \boldsymbol{\Lambda}_p + \boldsymbol{\Lambda}_p \, (\nabla \dot{\mathbf{v}})^{\mathsf{T}} \\ + (\nabla \mathbf{v}) \, \boldsymbol{\Lambda}_w + \boldsymbol{\Lambda}_w \, (\nabla \mathbf{v})^{\mathsf{T}} \end{pmatrix} \\ & + \lambda \begin{pmatrix} \nabla \cdot (\boldsymbol{\Lambda}_e \ddot{\mathbf{v}}) \\ + \nabla \cdot (\boldsymbol{\Lambda}_p \dot{\mathbf{v}}) \\ + \nabla \cdot (\boldsymbol{\Lambda}_w \mathbf{v}) \end{pmatrix} \mathbf{I}, \quad \mathbf{x} \in \Omega_{\text{PML}}, \end{aligned} \tag{4.2b}$$

where (4.2a) represents balance of linear momentum, and (4.2b) is the combined constitutive and kinematic equation. Equations (4.1) and (4.2) are also subject to the following boundary and interface conditions:

$$\left(\ddot{\mathbf{S}}^{\mathsf{T}} \boldsymbol{\Lambda}_e + \dot{\mathbf{S}}^{\mathsf{T}} \boldsymbol{\Lambda}_p + \mathbf{S}^{\mathsf{T}} \boldsymbol{\Lambda}_w \right) \mathbf{n}_{\text{PML}} = \mathbf{0}, \qquad \mathbf{x} \in \Gamma_{\text{PML}}^{\text{free}} \tag{4.3a}$$

$$\mathbf{v} = \mathbf{0}, \qquad \mathbf{x} \in \Gamma_{\text{PML}}^{\text{fixed}} \tag{4.3b}$$

$$\mathbf{v}_{\text{REG}} = \mathbf{v}_{\text{PML}}, \qquad \mathbf{x} \in \Gamma_{\text{I}} \tag{4.3c}$$

$$\begin{aligned} & \left[\mu \left(\nabla \dot{\mathbf{v}} + (\nabla \dot{\mathbf{v}})^{\mathsf{T}} \right) + \lambda \left(\nabla \cdot \dot{\mathbf{v}} \right) \mathbf{I} \right] \mathbf{n}_{\text{REG}} \\ & \quad + \left(\ddot{\mathbf{S}}^{\mathsf{T}} \boldsymbol{\Lambda}_e + \dot{\mathbf{S}}^{\mathsf{T}} \boldsymbol{\Lambda}_p + \mathbf{S}^{\mathsf{T}} \boldsymbol{\Lambda}_w \right) \mathbf{n}_{\text{PML}} = \mathbf{0}, \qquad \mathbf{x} \in \Gamma_{\text{I}}. \end{aligned} \tag{4.3d}$$

In addition to the above conditions, the TR step is driven by:

$$\mathbf{t}(\mathbf{x}, t) = \mathbf{u} \left(\mathbf{x}, T - t \right), \quad \mathbf{x} \in \Gamma_{\text{REG}}^{\text{TRM}}, \tag{4.4}$$

where $\mathbf{t}$ is the TRM traction of the TR step, and $\mathbf{u}$ is the TRM-recorded displacement histories during the forward step. In other words, (4.4) is the

D-to-N flipped boundary condition, where the TRM-recorded Dirichlet data of the forward step are imposed as Neumann condition during the TR step.

4.2 Numerical implementation - TR in 3D

Following steps similar to [23], the weak form corresponding for the motion in both Ω_{REG} and Ω_{PML} is written as:

$$\begin{aligned}
&\int_{\Omega_{\text{REG}}} \mathbf{w} \cdot \rho \ddot{\mathbf{v}}\, d\mathbf{x} \\
&+ \int_{\Omega_{\text{REG}}} \nabla \mathbf{w} : \left[\mu \left\{\nabla \dot{\mathbf{v}} + (\nabla \dot{\mathbf{v}})^{\intercal}\right\} + \lambda \left(\nabla \cdot \dot{\mathbf{v}}\right) \mathbf{I}\right] d\mathbf{x} \\
&+ \int_{\Omega_{\text{PML}}} \nabla \mathbf{w} : \left(\ddot{\mathbf{S}}^{\intercal} \boldsymbol{\Lambda}_e + \dot{\mathbf{S}}^{\intercal} \boldsymbol{\Lambda}_p + \mathbf{S}^{\intercal} \boldsymbol{\Lambda}_w\right) d\mathbf{x} \\
&+ \int_{\Omega_{\text{PML}}} \mathbf{w} \cdot \left(\mathsf{a}\ddot{\mathbf{v}} + \mathsf{b}\ddot{\mathbf{v}} + \mathsf{c}\dot{\mathbf{v}} + \mathsf{d}\mathbf{v}\right) d\mathbf{x} = \mathbf{0},
\end{aligned} \tag{4.5}$$

and:

$$\begin{aligned}
&\int_{\Omega_{\text{PML}}} \mathbf{T} : \left(\mathsf{a}\dddot{\mathbf{S}} + \mathsf{b}\ddot{\mathbf{S}} + \mathsf{c}\dot{\mathbf{S}} + \mathsf{d}\mathbf{S}\right) d\mathbf{x} \\
&= \int_{\Omega_{\text{PML}}} \mathbf{T} : \mu \begin{pmatrix} \left(\nabla \ddot{\mathbf{v}}\right) \boldsymbol{\Lambda}_e + \boldsymbol{\Lambda}_e \left(\nabla \ddot{\mathbf{v}}\right)^{\intercal} \\ + \left(\nabla \dot{\mathbf{v}}\right) \boldsymbol{\Lambda}_p + \boldsymbol{\Lambda}_p \left(\nabla \dot{\mathbf{v}}\right)^{\intercal} \\ + \left(\nabla \mathbf{v}\right) \boldsymbol{\Lambda}_w + \boldsymbol{\Lambda}_w \left(\nabla \mathbf{v}\right)^{\intercal} \end{pmatrix} d\mathbf{x} \\
&+ \int_{\Omega_{\text{PML}}} \mathbf{T} : \lambda \left[\nabla \cdot \left(\boldsymbol{\Lambda}_e \ddot{\mathbf{v}}\right) + \nabla \cdot \left(\boldsymbol{\Lambda}_p \dot{\mathbf{v}}\right) + \nabla \cdot \left(\boldsymbol{\Lambda}_w \mathbf{v}\right)\right] \mathbf{I}\, d\mathbf{x}.
\end{aligned} \tag{4.6}$$

After the introduction of approximants for the trial functions $\mathbf{v}$, $\mathbf{S}$, and the test functions $\mathbf{w}$, $\mathbf{T}$ to $\mathbf{w}_h$, there results the following semi-discrete form:

$$\mathbf{M}\dddot{\mathbf{d}} + \mathbf{C}\ddot{\mathbf{d}} + \mathbf{K}\dot{\mathbf{d}} + \mathbf{G}\mathbf{d} = \mathbf{0}, \tag{4.7}$$

where $\mathbf{d}$ is the vector that contains nodal displacements everywhere, and nodal stresses within the PML only; the definitions of matrices $\mathbf{M}$, $\mathbf{C}$, $\mathbf{K}$, and $\mathbf{G}$ are

given in Appendix A.2. We remark that the resulting semi-discrete form is third-order in time, by contrast to the second-order in time for the 2D case. Moreover, we note that, owing to the adoption of a Gauss-Lobatto quadrature scheme, the mass matrix is diagonal, and thus, trivially invertible. The latter allows us to reduce the third-order semi-discrete form to a system of first-order equations and use an explicit solver, as described in [23]. The semi-discrete form (4.7), or its first-order counterpart, is subsequently integrated in time to provide the solution for the TR step in 3D.

4.3 TR with multiple targets in 3D

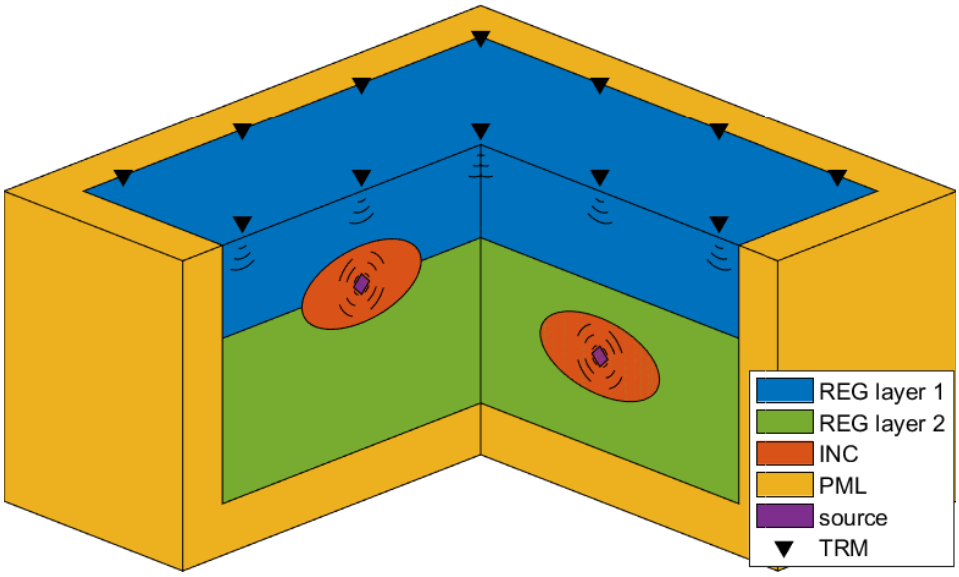

Figure 4.2: Model configuration and schematic drawing of the experiment, not in scale

In this section, we report numerical experiments involving multiple tar-

gets in 3D. We use the same model, depicted in Fig. 4.2, for all simulations. Specifically, the domain of interest is a rectangular parallelepiped 80 m $\times$ 80 m $\times$ 40 m deep, surrounded by a 6.25 m-thick PML buffer on all sides, except on the surface. The host medium consists of a 20 m deep layer on a halfspace. There are two soft, geometrically identical, spheroidal inclusions embedded within the host. One of the spheroids is centered at ($-$15 m, $-$15 m, $-$20 m), effectively intersecting the layer interface, and the other is centered at (15 m, 15 m, $-$30 m). For both spheroids, their semi-axes are (7.5 m, 7.5 m, 3.75 m). The material properties of each layer and of the inclusions are summarized in table 4.1.

Table 4.1: Material properties of each layer

	λ(MPa)	μ(MPa)	ν	ρ(kg/m^3)	c_p(m/s)	c_s(m/s)
inclusions	100	100	0.25	2000	387.2983	223.6068
layer 1	300	300	0.25	2000	670.8204	387.2983
layer 2	500	500	0.25	2000	866.0254	500

The relative softness of inclusions with respect to the surrounding layers is intended to mimic the contrast between shallow reservoirs and their host background.

The model is meshed with 27-node hexahedral spectral elements. The typical element size is 1.25 m; the time step was set to Δt=0.0006 s, and the PML parameters are chosen to be α_0=5 and β_0=866 s^{-1} [23].

Using the protype model, we conduct five numerical experiments aimed

at assessing the effect of key parameters to the focusing. Specifically, in the first three experiments we vary the density of the TR mirror (but not its aperture), in the fourth experiment we randomize the domain's properties, and in the fifth experiment we attempt to control the intensity of the focus so that both targets are similarly excited despite the difference in depth and in their surroundings.

The experiment parameters and their intended purpose are tabulated in table 4.2.

Table 4.2: List of numerical experiments

experiment ID	number of domain sources		TRM density	purpose
	inc. 1	inc. 2		
1	1	1	full	validity of TR
2	1	1	quarter	validity of TR with reduced TRM density
3	1	1	16	validity of TR with ultra low TRM density
4	1	1	full	validity of TR with arbitrary heterogeneity in material properties
5	1	2	full	intensity control for multiple targets

To generate the recordings at the TRM, we perform a forward step

computation, using a single source per target (except for Experiment 5). Based on the findings reported in section 2.2.5.4 and in [37], we prefer a Ricker-like pulse: here we use a pulse with a central frequency of 25 Hz per Fig. 4.3. Moreover, the sources embedded in the target were applied along the two

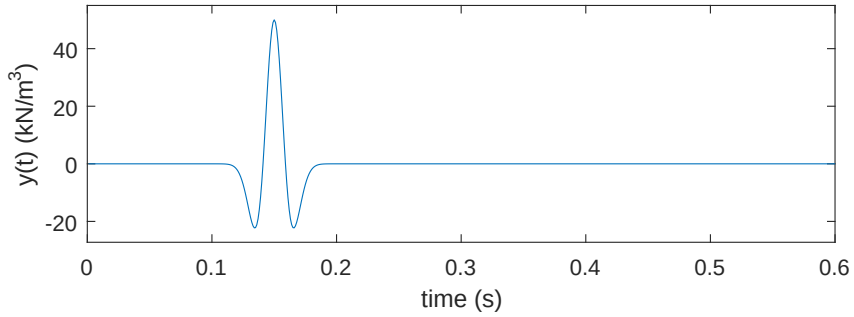

(a) Wave source Ricker-like pulse

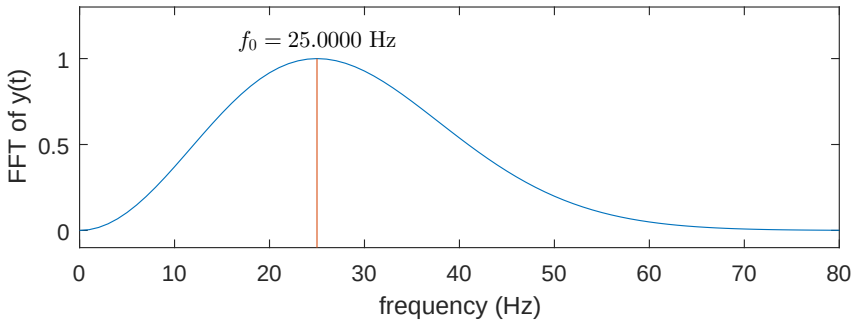

(b) Wave source frequency spectrum; normalized

Figure 4.3: Wave source characteristics

transverse directions (horizontal), again per the findings of section 2.2.3 and of [37].

Figure 4.4 depicts snapshots at two different moments in time of the forward wavefield, generated by the simultaneous triggering of two Ricker sources

embedded at the center of the inclusions.

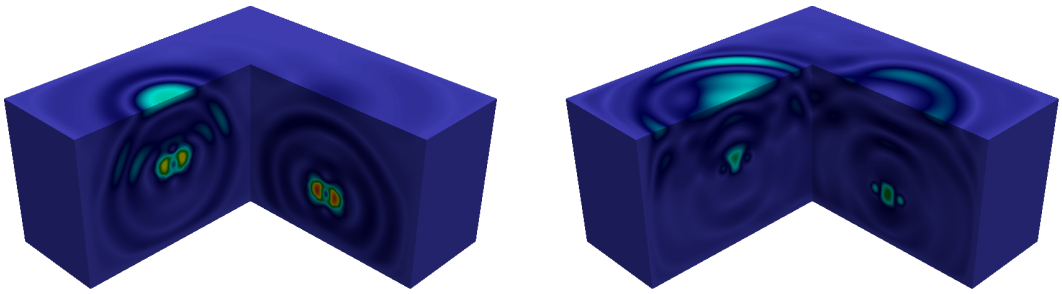

Figure 4.4: Forward step wavefield at 0.021 s (left) and at 0.024 s (right)

4.3.1 Mirror density effect (Experiments 1 to 3)

4.3.1.1 Experiment 1 – Full density TR mirror

In Experiment 1, we use the full TRM on $\Gamma_{\text{REG}}^{\text{TRM}}$, which numbers 16,129 sensors. The recorded displacement histories are time-reversed and applied as tractions, per the D-to-N discussion. The maximum amplitude of the applied tractions has been set to 1 kPa.

Figure 4.5 shows the average kinetic energy $\text{KE}^{\text{TA}}(\mathbf{x})$ during the TR step: it can be seen that the waves have refocused at the targets, and the targets have been clearly illuminated. The illumination is stronger for the left target that is located closer to the ground surface than the right target. This is as expected, due to radiation damping, which forces greater attenuation for the waves reaching the deeper target.

Naturally, it would be desirable for both targets to be equally strongly illuminated (or, possibly, be differentially illuminated based on a preset application-driven criterion). A way to achieve wavefields of similar strength at the targets,

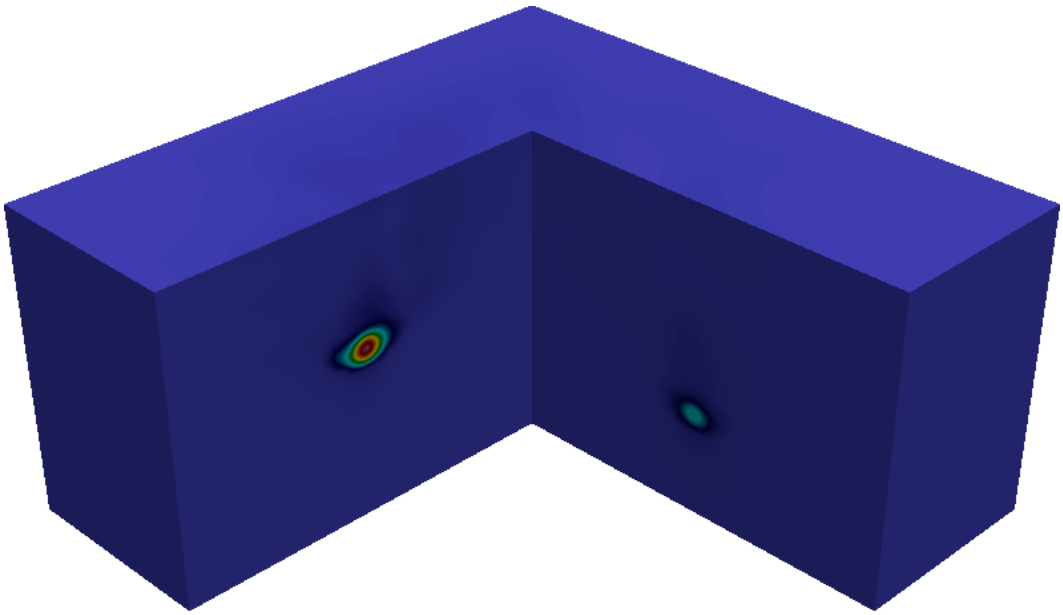

Figure 4.5: Time-averaged kinetic energy $\left(\mathrm{KE}^{\mathrm{TA}}(\mathbf{x})\right)$ with full TR mirror - Experiment 1

is by impregnating the TRM records prior to time-reversal with the desired strength. This can be accomplished, as Experiment 5 demonstrates, by modulating the strength or the number of the sources at the targets during the forward step.

The graphs of the instantaneous kinetic energies sweeping through the targets are depicted in Fig 4.6. The key difference between the two plots is in the average intensity: the deeper target's intensity is about 35% that of the shallow target's.

Figure 4.7 compares the displacement component time histories under the source in the target, between the forward and the TR steps. For example, the top left plot depicts (in blue) the x-component time history at the target

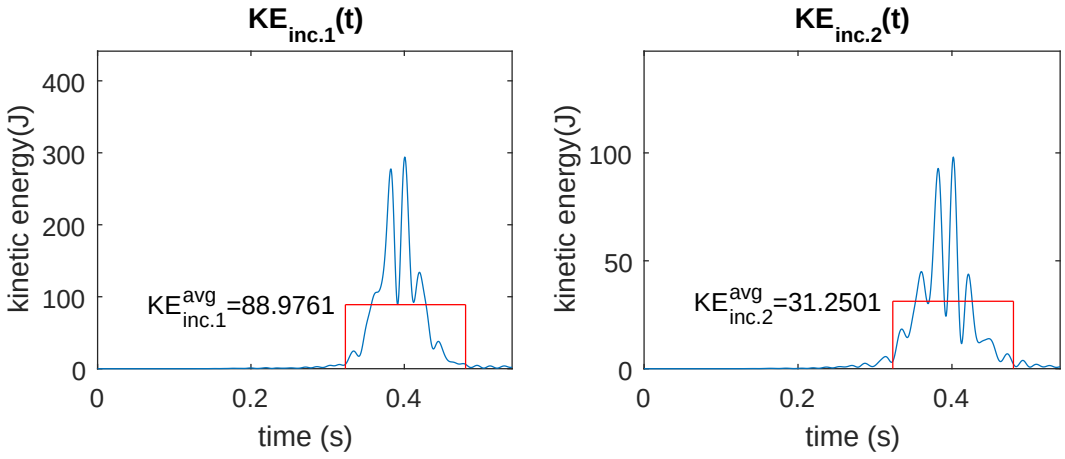

Figure 4.6: Kinetic energy inside the target: shallow target (left); deep target (right) - Experiment 1 - full TR mirror density

during the forward step: it is essentially the "displacement-under-the-load." The same plot also shows (in red) the x-component time history during the time-reversal step recorded also at the target. The similarity of the traces, modulo the time delay and the amplitude (the latter has been tuned at the TRM), is evidence of the quality of the refocusing. It can be seen that the shallower target's refocusing is of better quality than that of the deeper target's. We also remark that since the TRM applied the tractions in transverse directions, the z-component records are essentially the result of mode conversions and rather insignificant.

As limited as it may be, Experiment 1 suggests that focusing to multiple targets is possible using the TR concept, despite the presence of several hostile conditions (domain unboundness, D-to-N flipping, etc).

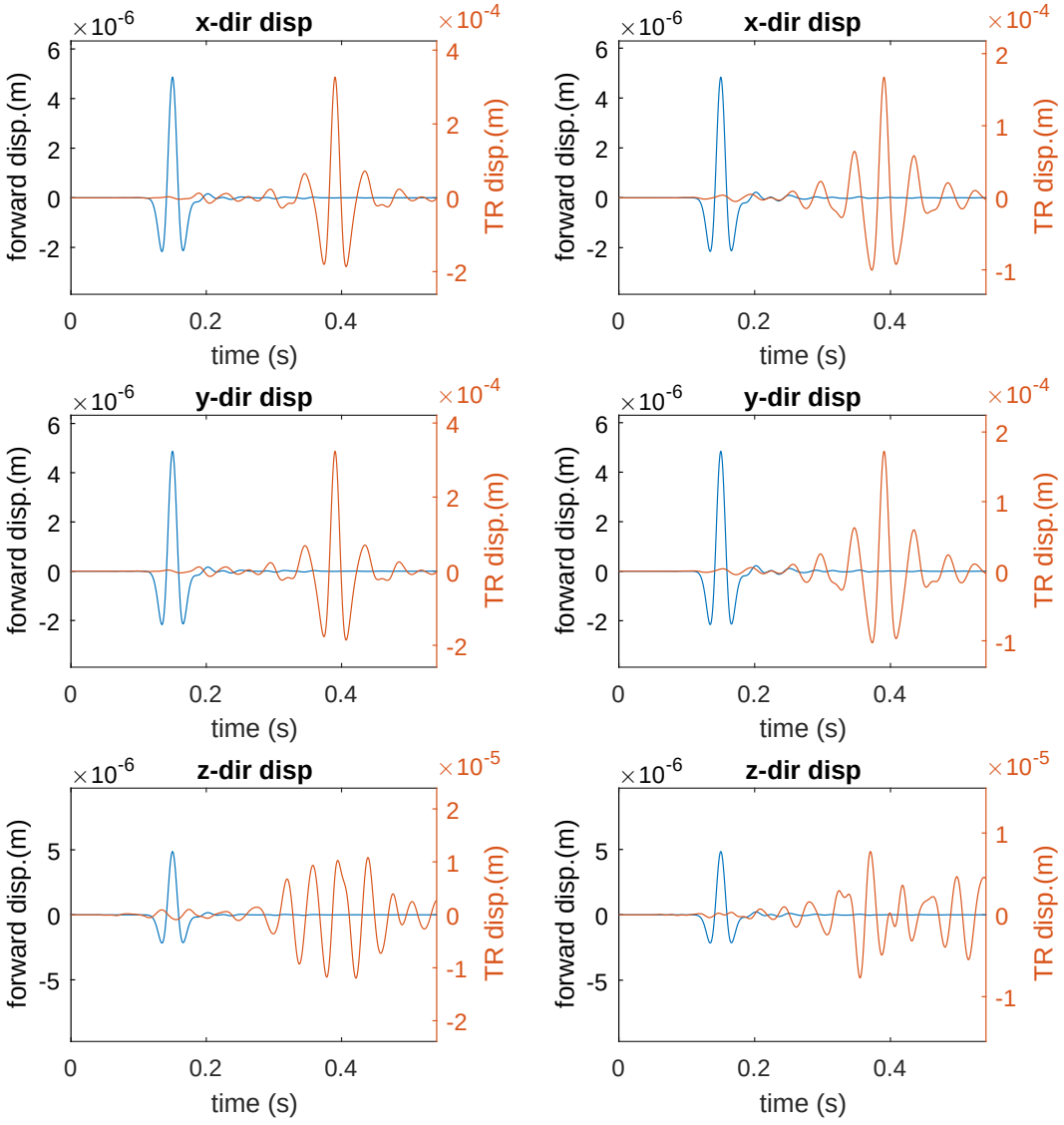

Figure 4.7: Displacement time histories at the target; shallow target (left column); deep target (right column); forward step histories in blue; TR step histories in red - Experiment 1

4.3.1.2 Experiment 2 – Quarter density TR mirror

In the previous experiment, we applied surface tractions on every computational node on the ground surface $\Gamma_{\text{REG}}^{\text{TRM}}$. Physically, such sensor/actuator deployment is infeasible, and thus, for Experiment 2, we repeat the TR step using a quarter of the TRM, or about 3,696 computational nodes where the time-reversed tractions are applied. The number of actuators is still large, and remains practically unrealizable, but the experiment will allow us to further assess the dependence of the focusing on the mirror's density. We note that the aperture remains the same, i.e, the mirror is sparsified, but its spatial extent is unaltered (Fig. 4.8).

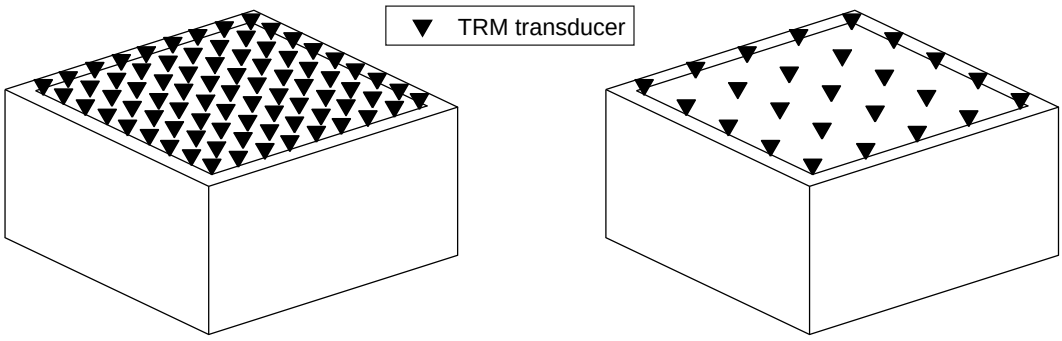

Figure 4.8: Conceptual schematic of quarter density TR mirror (right) compared to the full density TR mirror (left)

Figure 4.9 depicts again the time-averaged kinetic energy: the targets have been anew illuminated, albeit the magnitude is different owing to the reduced wave energy supplied at the TRM.

The instantaneous kinetic energy $\text{KE}_{\text{inc}}(t)$ and the TR displacement histories are shown in Fig. 4.10 and 4.11, respectively.

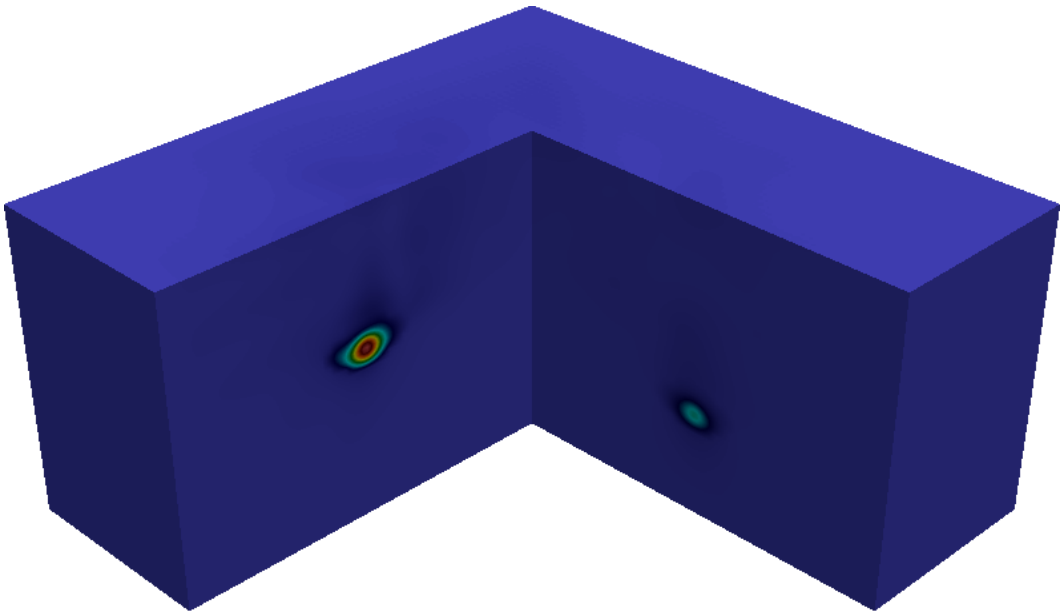

Figure 4.9: Time-averaged kinetic energy $\left(\mathrm{KE}^{\mathrm{TA}}(\mathbf{x})\right)$ with quarter density TR mirror - Experiment 2

By comparing the Experiment 2 results depicted in Figs. 4.9 and 4.11 with the corresponding Experiment 1 results depicted in Figs. 4.5 and 4.7, it can be seen that, qualitatively, the quarter TR mirror density results are very similar to the full mirror results. There are, of course, quantitative differences: the $\mathrm{KE}_{\mathrm{inc}}^{\mathrm{TA}}$ for the shallow target has been reduced from 88.9791J to 5.4626J, and for the deep target it has dropped from 31.2501J to 1.9248J. For both experiments, the energy efficiency for the shallow target is about 7.7%, and about 2.7% for the deep target. Moreover, the delivered energy to each target in Experiment 2 is about 6% of the corresponding Experiment 1 energy: this percentage is approximately equal to the square of the ratio of the actuators used between the two experiments, i.e., approximately equal to

$\left(\frac{3{,}696}{16{,}129}\right)^2$ regardless of the distance from the TRM to the targets. The square of the actuator ratio is a measure of relative energy input. The result is in good agreement with the reports in Anderson et al. [3] and in Koo et al. [37]. The comparison between the experiments is summarized in Table 4.3.

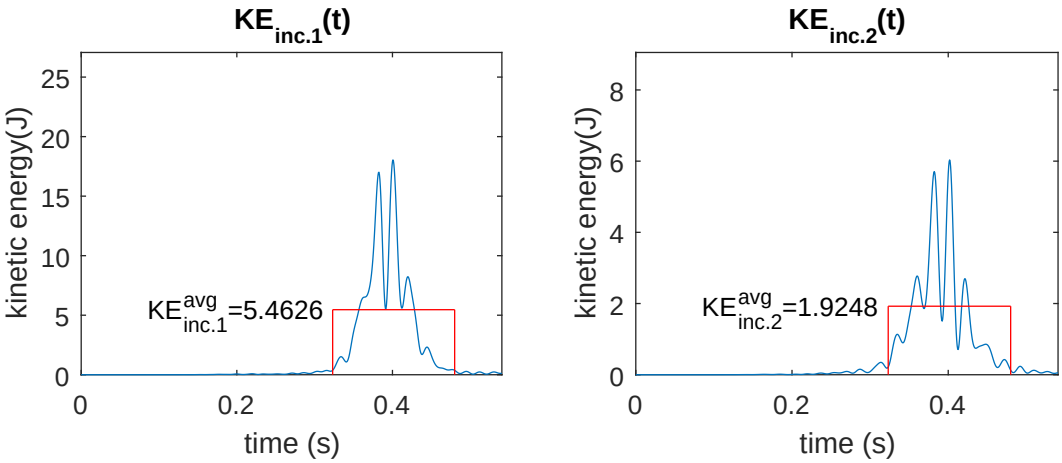

Figure 4.10: Kinetic energy inside the target: shallow target (left); deep target (right) - Experiment 2 - quarter TR mirror density

4.3.1.3 Experiment 3 – Ultra low density TR mirror

In Experiment 3 we reduce the TRM density to only 16 actuators –a number that is practically feasible, and repeat the TR simulation. Figure 4.12 depicts the time-averaged kinetic energy that has helped us before gauge the illumination. Though the targets have been again illuminated as previously in Experiments 1 and 2, the surface TRM actuators are also visible. This is due to the fact that, since the number of actuators is small, the delivered energy to each target is now comparable to the input energy at each actuator.

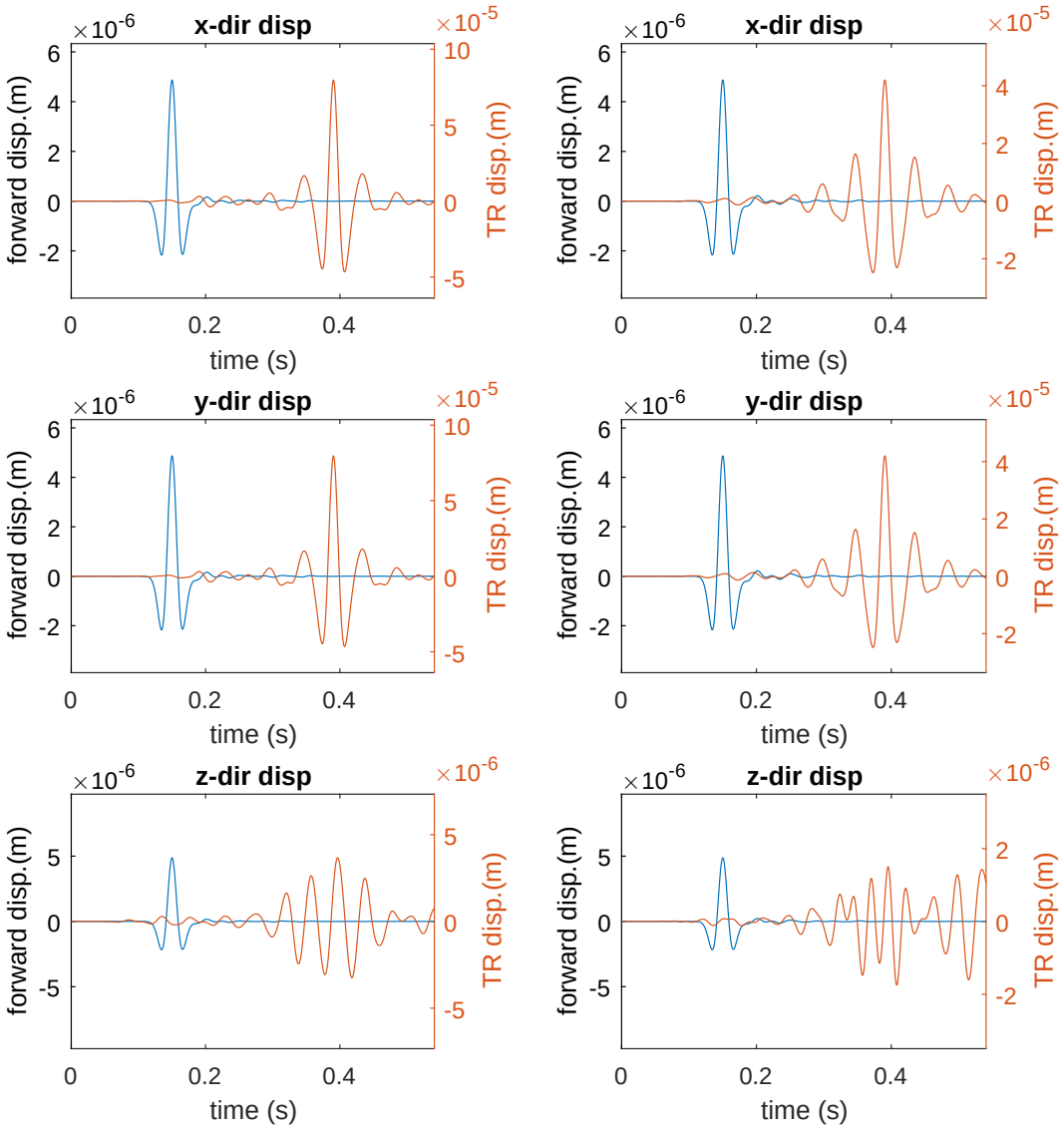

Figure 4.11: Displacement time histories at the target; shallow target (left column); deep target (right column); forward step histories in blue; TR step histories in red - Experiment 2

Nevertheless, focusing is still realized. For reference, the instantaneous kinetic energy is shown in Fig. 4.13.

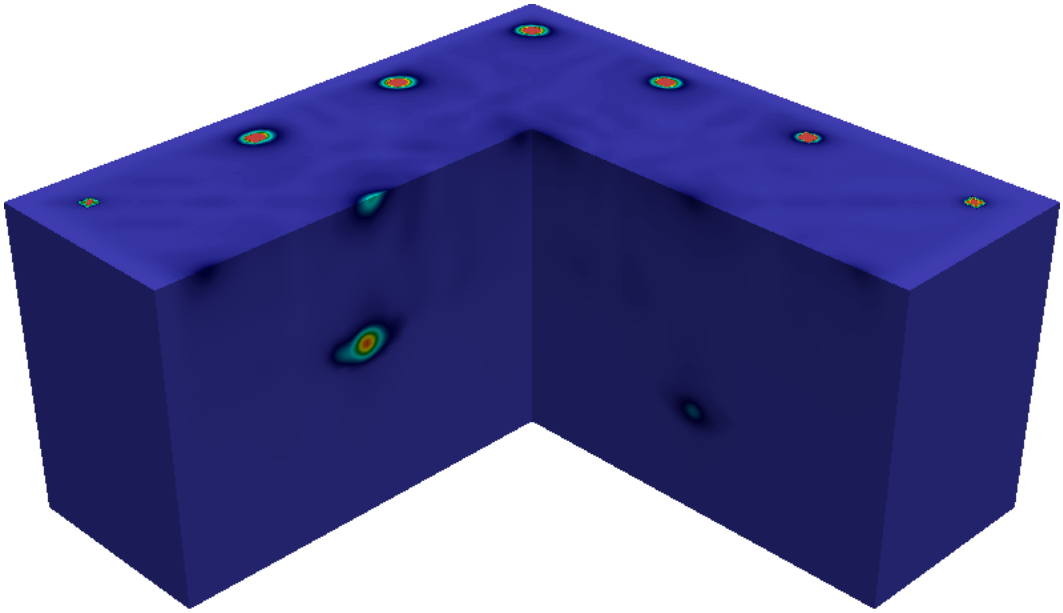

Figure 4.12: Time-averaged kinetic energy $\left(\mathrm{KE}^{\mathrm{TA}}(\mathbf{x})\right)$ with ultra low TR mirror density - Experiment 3

Here, we can confirm that there is no qualitative degradation of $\mathrm{KE}_{\mathrm{inc}}(t)$ when compared with Experiment 1 and 2. However, the values of Experiment 3 are much less than those of Experiments 1 and 2 because of the smaller number of TRM actuators. The results are tabulated in Table 4.3. Again, it can be verified that the square of the actuator ratios are consistent with the ratios of the delivered energy to the targets.

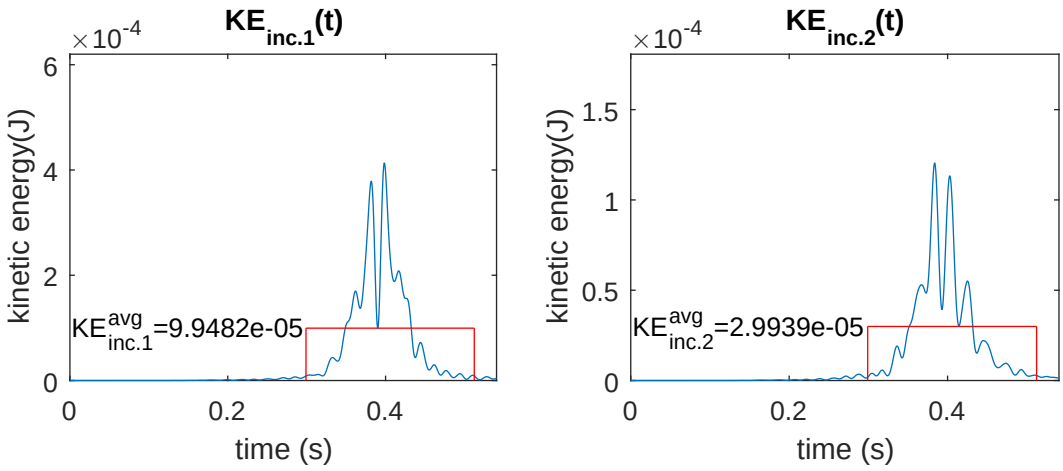

Figure 4.13: Kinetic energy inside the target: shallow target (left); deep target (right) - Experiment 3 - ultra low TR mirror density

Table 4.3: Summary of E_{input}, KE_{inc}^{TA}, and delivery efficiency of experiments 1, 2 and 3

	E_{input}(J)		KE_{inc}^{TA}(J)	KE_{inc}^{TA}/E_{input}
Experiment 1	1154.1503	target 1	88.9761	7.7092×10^{-3}
		target 2	31.2501	2.7076×10^{-3}
Experiment 2	71.3771	target 1	5.4626	7.7653×10^{-3}
		target 2	1.9248	2.6966×10^{-3}
Experiment 3	1.3214×10^{-2}	target 1	9.9482×10^{-5}	7.5290×10^{-4}
		target 2	2.9939×10^{-5}	2.2660×10^{-4}

4.3.2 Experiment 4 – Wave focusing in a medium of random heterogeneity

In this experiment, we endow the prototype model with random heterogeneity by varying the layer and inclusion properties randomly up to 33% off of their constant values shown in Table 4.1. The resulting property distribution is shown in Fig. 4.14 for the shear wave velocity.

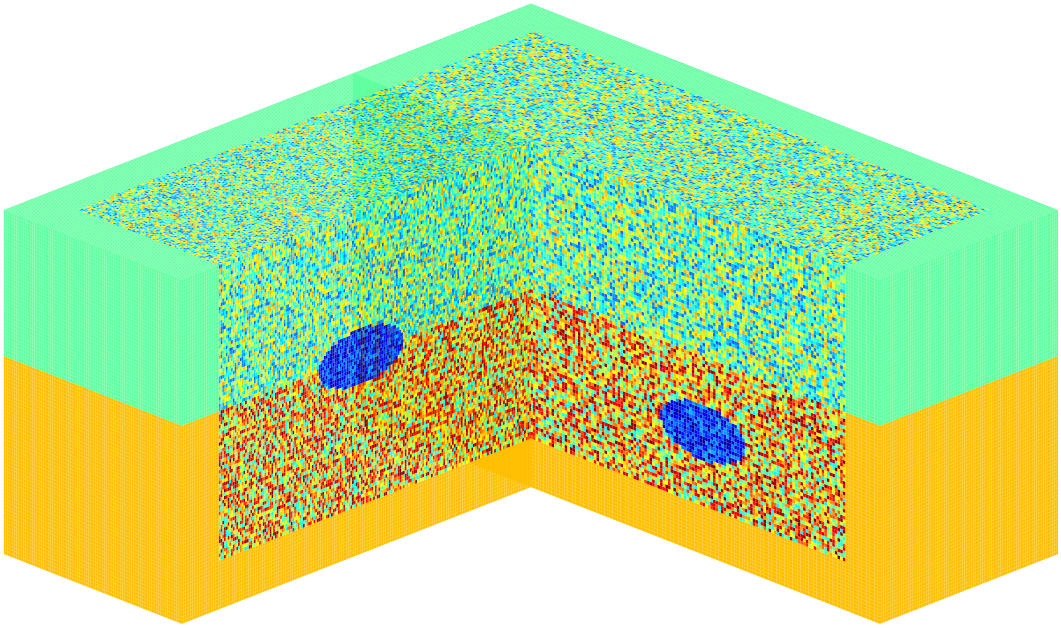

Figure 4.14: Shear wave velocity (in m/s) of randomized heterogeneous model

The full TR mirror is used anew, and the resulting time-averaged ditribution $\mathrm{KE}^{\mathrm{TA}}(\mathbf{x})$ is shown in Fig. 4.15. When we compare the latter Fig. 4.15 to the corresponding one from Experiment 1 (Fig. 4.5), there are no noticeable qualitative differences; quantitatively, the Experiment 1 energy delivered to the shallow target is 88.9761 J, whereas for Experiment 4 it is about 86.7983

J, a difference of less than 2.5%. Thus, the time-reversal approach for wave focusing appears promising even under arbitrary heterogeneity conditions.

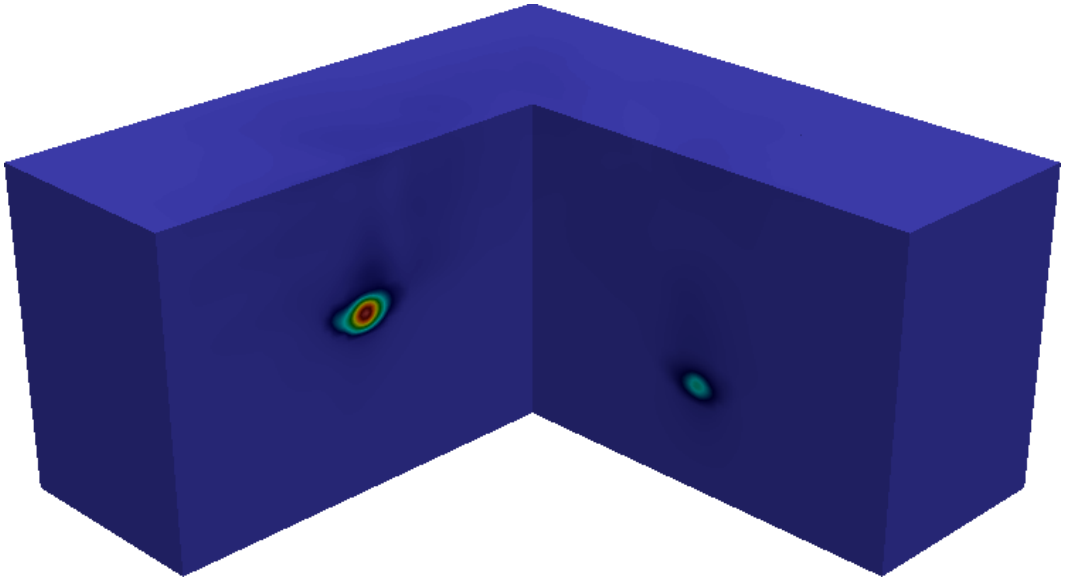

Figure 4.15: Time-averaged kinetic energy $\left(\mathrm{KE}^{\mathrm{TA}}(\mathbf{x})\right)$ in a randomized heterogeneous medium - Experiment 4

4.3.3 Experiment 5 – Focus intensity control

We observed earlier that with two subsurface targets, the strength of the time-averaged kinetic energy during the TR step was weaker for the deeper of the two targets. In this experiment, instead of driving the forward step with a single source per target, we now install two sources in the deeper target (or equivalently, the amplitude of the source at the deeper target is doubled). We use again the full TR mirror. The time-averaged kinetic energy is shown in Fig. 4.17. As it can be seen in Fig. 4.17, the deeper target has now been

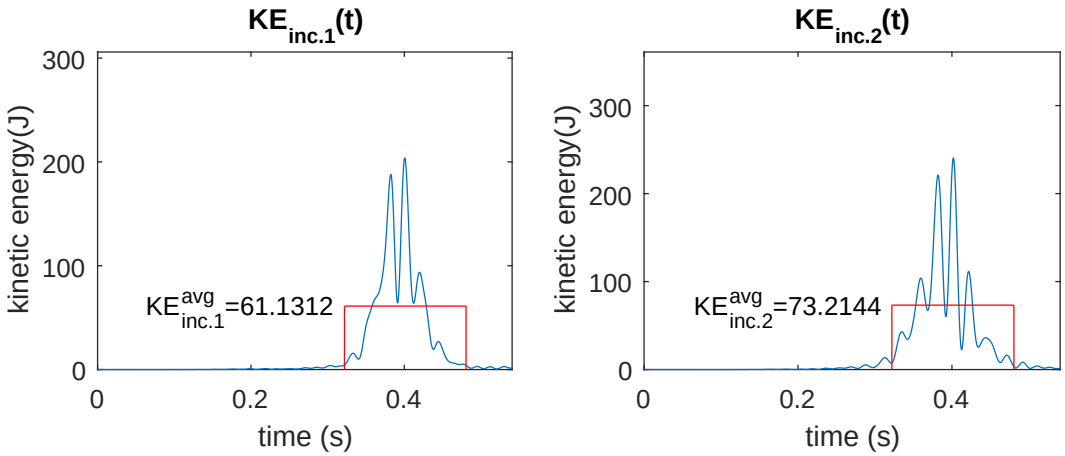

Figure 4.16: Kinetic energy inside the target: shallow target (left); deep target (right) - Experiment 4

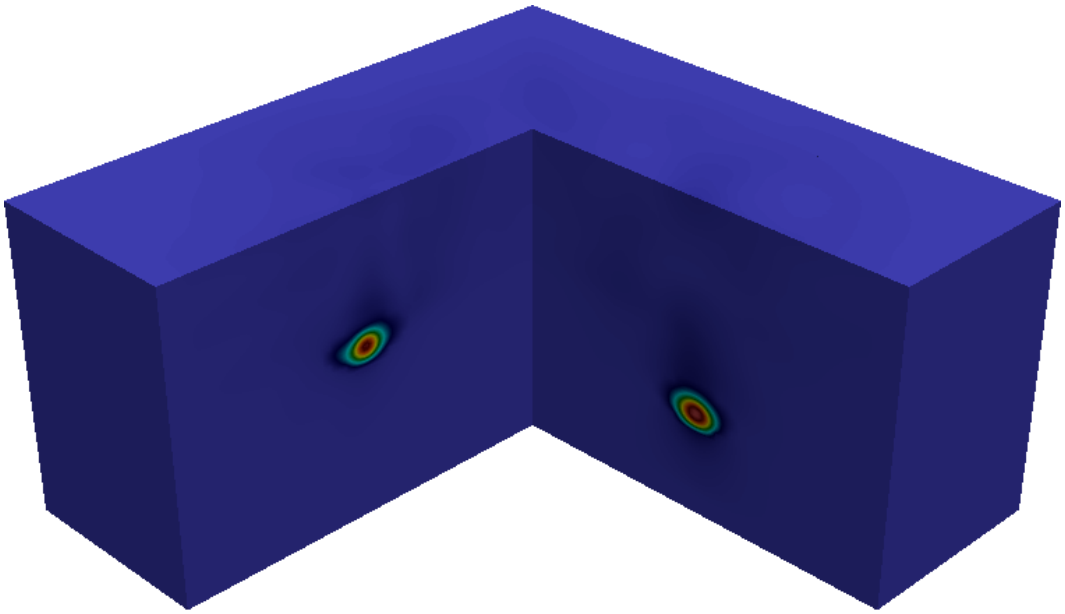

Figure 4.17: Time-averaged kinetic energy $\left(\mathrm{KE}^{\mathrm{TA}}(\mathbf{x})\right)$ - intensity control - Experiment 5

illuminated to a level comparable to the shallow target. In fact, the deeper target's energy is about 73.2144 J compared to about 61.1312 J for the shallow target, when the contrast in Experiment 1 was 31.2501 J to 88.9761 J for the two targets, respectively (also see Table 4.3). We conclude from this experiment

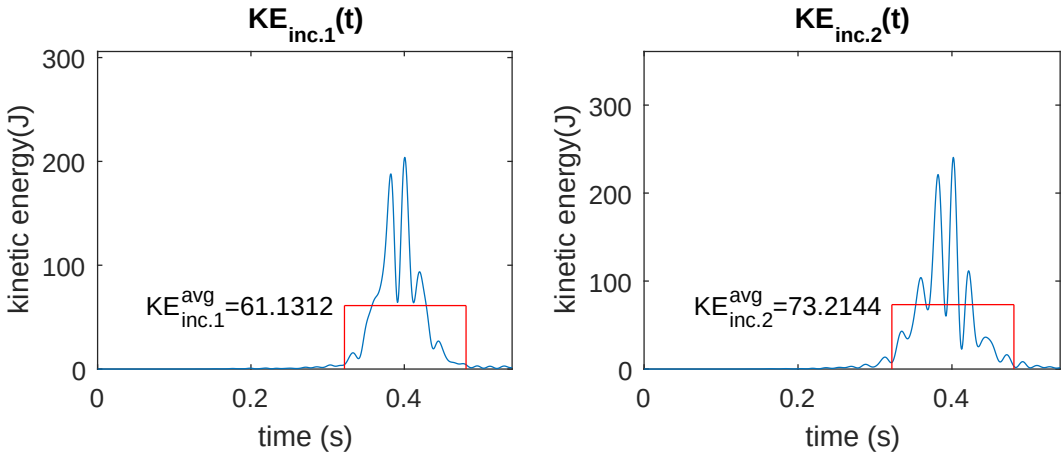

Figure 4.18: Kinetic energy inside the target: shallow target (left); deep target (right) - Experiment 5

that it is possible to control the relative energy directed to each target by modulating the sources for a desirable outcome.

4.4 Summary

In this chapter, we looked for a way to bring about desired mechanical changes, by means of kinetic energy, to multiple targets embedded in 3D elastic heterogeneous semi-infinite media. Specifically, we studied the ability of the TR approach to focus waves to multiple targets (two targets in our experiments) located at different depths and embeddded in a heterogenous host. Overall,

it appears that even under onerous field conditions, focusing is quite feasible; equally possible is the ability to control the intensity of the focused energy by modulating the probes embedded in the targets.

Chapter 5

Conclusions

5.1 Studies on time-reversal for wave focusing in elastic media

In this dissertation, through computational simulations in two- and three-dimensional domains, we sought to provide evidence of the applicability of the time-reversal concept for focusing waves to subsurface targets. Whereas, to date, there is ample evidence in the literature for applications of the TR concept in acoustics, and predominantly to closed-cavity or waveguide problems, the literature is thin on applications in elastic hosts, and more so when unbounded domains are involved.

We discussed, based on computational evidence, the effect various physically unrealizable conditions have on focusing. These included sink/source effects, heterogeneity, unboundness, initial conditions, loading directions, TRM density, and source intensity. Among all of them, the condition most critically affecting the focusing resolution is, what we termed, D-to-N flipping, namely, the need to time-reverse as Neumann data time histories that were originally recorded as Dirichlet data.

We offered mathematical evidence of the resolution deterioration for the

scalar wave case, but not for the elastic case, though we conjecture that a similar mechanism to the scalar case is responsible for the resolution deterioration in the elastic case. We designed a filter, with limited applicability, that is capable of restoring the resolution, provided it is applied prior to time-reversing the TRM data. We conjecture that filters can be developed to improve the resolution in the general elastic case.

We conclude that TR appears to be a potent method for steering wave motion to subsurface targets, provided a trigger/probe/source has already been installed at the targets. In fact, we showed focusing to targets embedded in randomized heterogeneous media, under adverse conditions. We also demonstrated the potential for EOR, and the competitiveness of the TR methodology against alternative inverse-source approaches. We recall that the latter require *a priori* knowledge of the formation's properties, whereas the TR approach does not.

5.2 Future work

1. **Chorochronic event localization**

   We have experimented, but not reported herein, with the applicability of the TR concept for chorochronic event localization, that is, using TR for localizing in time and space an event recorded at a distant TR mirror. The development will allow for defect identification, when the defect's growth results in wave motion, as is the case with cracks, seismic ruptures, etc.

2. **Improved resolution**

   We have provided evidence that upon filtering the TRM records, improved resolution can result in the D-to-N case. Extensions of these ideas to the all important elastic case are worthy of future investigations.

3. **Attenuation effects**

   Of the various ways waves are attenuated when propagating in the earth, only radiation attenuation due to expanding wave fronts was taken into account in the development presented herein. Intrinsic attenuation (material damping) and apparent attenuation (due to scattering) were not modeled. Accounting for either or both of the latter forms of attenuation would give rise to a first-order time-derivative in the mathematical model. Clearly, if the attenuation term were to be time-reversed during the time-reversal step, it would be adding energy to the system. Since the TRM records would account for attenuation, it is of interest to study the effect on focusing when attenuation is excluded from the time-reversal step.

Appendices

Appendix A

Matrix definitions

A.1 In two dimensions with PML

The equation of motion in 2D with Perfectly-Matched-Layers(PMLs) is:

$$\mathbf{M}\ddot{\mathbf{d}}(t) + \mathbf{C}\dot{\mathbf{d}}(t) + \mathbf{K}\mathbf{d}(t) = \mathbf{f}(t). \tag{2.23}$$

The structure of matrices $\mathbf{M}$, $\mathbf{C}$, and $\mathbf{K}$ is:

$$\mathbf{M} = \left[\begin{array}{c|c|c} \mathbf{M}_{\mathrm{REG}} & & \\ \hline & \mathbf{M}_{\mathsf{a}} & \\ \hline & & \mathbf{N}_{\mathsf{a}} \end{array}\right] \tag{A.1a}$$

$$\mathbf{C} = \left[\begin{array}{c|c|c} & & \\ \hline & \mathbf{M}_{\mathsf{b}} & \mathbf{A}_{eu} \\ \hline & \mathbf{A}_{el} & \mathbf{N}_{\mathsf{b}} \end{array}\right] \tag{A.1b}$$

$$\mathbf{K} = \left[\begin{array}{c|c|c} \mathbf{K}_{\mathrm{REG}} & & \\ \hline & \mathbf{M}_{\mathsf{c}} & \mathbf{A}_{pu} \\ \hline & \mathbf{A}_{pl} & \mathbf{N}_{\mathsf{c}} \end{array}\right] \tag{A.1c}$$

The definitions of each block matrix are provided next.

A.1.1 Regular domain

In the expressions given below, $\mathbf{\Phi}$ is a Lagrange interpolant, ρ is mass density, and λ and μ are the Lamé parameters.

$$\mathbf{M}_{\mathrm{REG}} = \int_{\Omega_{\mathrm{REG}}} \rho \begin{bmatrix} \mathbf{\Phi}\mathbf{\Phi}^{\mathsf{T}} & & \\ & \mathbf{\Phi}\mathbf{\Phi}^{\mathsf{T}} & \\ & & \end{bmatrix} d\mathbf{x} \tag{A.2}$$

$$\mathbf{K}_{\mathrm{REG}} = \int_{\Omega_{\mathrm{REG}}} \begin{bmatrix} \mathbf{K}_{xx} & \mathbf{K}_{xy} \\ \mathbf{K}_{yx} & \mathbf{K}_{yy} \end{bmatrix} d\mathbf{x} \tag{A.3}$$

$$\mathbf{K}_{xx} = (\lambda + 2\mu)\mathbf{\Phi}_x\mathbf{\Phi}_x^{\mathsf{T}} + \mu\ \mathbf{\Phi}_y\mathbf{\Phi}_y^{\mathsf{T}} \tag{A.4a}$$

$$\mathbf{K}_{xy} = \lambda\ \mathbf{\Phi}_x\mathbf{\Phi}_y^{\mathsf{T}} + \mu\ \mathbf{\Phi}_y\mathbf{\Phi}_x^{\mathsf{T}} \tag{A.4b}$$

$$\mathbf{K}_{yx} = \mu\ \mathbf{\Phi}_y\mathbf{\Phi}_x^{\mathsf{T}} + \lambda\ \mathbf{\Phi}_x\mathbf{\Phi}_y^{\mathsf{T}} \tag{A.4c}$$

$$\mathbf{K}_{yy} = \mu\ \mathbf{\Phi}_x\mathbf{\Phi}_x^{\mathsf{T}} + (\lambda + 2\mu)\mathbf{\Phi}_y\mathbf{\Phi}_y^{\mathsf{T}} \tag{A.4d}$$

A.1.2 Perfectly-Matched-Layers (PMLs)

$$\mathbf{M}_{\mathsf{a}} = \mathsf{a}\mathbf{M}_{\mathrm{REG}}, \qquad \mathbf{M}_{\mathsf{b}} = \mathsf{b}\mathbf{M}_{\mathrm{REG}}, \qquad \mathbf{M}_{\mathsf{c}} = \mathsf{c}\mathbf{M}_{\mathrm{REG}} \tag{A.5a}$$

$$\mathsf{a} = \alpha_x\alpha_y, \qquad \mathsf{b} = \alpha_x\beta_y + \alpha_y\beta_y, \qquad \mathsf{c} = \beta_x\beta_y \tag{A.5b}$$

$$\mathbf{N}_n = \int_{\Omega_{\mathrm{PML}}} n \begin{bmatrix} \mathbf{\Phi}\mathbf{\Phi}^{\mathsf{T}} & & \\ & \mathbf{\Phi}\mathbf{\Phi}^{\mathsf{T}} & \\ & & 2\mathbf{\Phi}\mathbf{\Phi}^{\mathsf{T}} \end{bmatrix} d\mathbf{x}, \quad n = \mathsf{a}, \mathsf{b}, \mathsf{c} \tag{A.6}$$

$$\mathbf{A}_{eu} = \int_{\Omega_{\mathrm{PML}}} \begin{bmatrix} \alpha_y\mathbf{\Phi}_x\mathbf{\Phi}^{\mathsf{T}} & & \alpha_x\mathbf{\Phi}_y\mathbf{\Phi}^{\mathsf{T}} \\ & \alpha_x\mathbf{\Phi}_y\mathbf{\Phi}^{\mathsf{T}} & \alpha_y\mathbf{\Phi}_x\mathbf{\Phi}^{\mathsf{T}} \end{bmatrix} d\mathbf{x} \tag{A.7}$$

$$\mathbf{A}_{pu} = \int_{\Omega_{\text{PML}}} \begin{bmatrix} \beta_y \mathbf{\Phi}_x \mathbf{\Phi}^\intercal & & \beta_x \mathbf{\Phi}_y \mathbf{\Phi}^\intercal \\ & \beta_x \mathbf{\Phi}_y \mathbf{\Phi}^\intercal & \beta_y \mathbf{\Phi}_x \mathbf{\Phi}^\intercal \end{bmatrix} d\mathbf{x} \tag{A.8}$$

$$\mathbf{A}_{el} = \int_{\Omega_{\text{PML}}} \begin{bmatrix} (\lambda+2\mu)\alpha_y \mathbf{\Phi}\mathbf{\Phi}_x^\intercal & \lambda\alpha_x \mathbf{\Phi}\mathbf{\Phi}_y^\intercal \\ \lambda\alpha_y \mathbf{\Phi}\mathbf{\Phi}_x^\intercal & (\lambda+2\mu)\alpha_x \mathbf{\Phi}\mathbf{\Phi}_y^\intercal \\ 2\mu\alpha_x \mathbf{\Phi}\mathbf{\Phi}_y & 2\mu\alpha_y \mathbf{\Phi}\mathbf{\Phi}_x \end{bmatrix} d\mathbf{x} \tag{A.9}$$

$$\mathbf{A}_{pl} = \int_{\Omega_{\text{PML}}} \begin{bmatrix} (\lambda+2\mu)\beta_y \mathbf{\Phi}\mathbf{\Phi}_x^\intercal & \lambda\beta_x \mathbf{\Phi}\mathbf{\Phi}_y^\intercal \\ \lambda\beta_y \mathbf{\Phi}\mathbf{\Phi}_x^\intercal & (\lambda+2\mu)\beta_x \mathbf{\Phi}\mathbf{\Phi}_y^\intercal \\ 2\mu\beta_x \mathbf{\Phi}\mathbf{\Phi}_y & 2\mu\beta_y \mathbf{\Phi}\mathbf{\Phi}_x \end{bmatrix} d\mathbf{x} \tag{A.10}$$

In the above, α_x and α_y are the stretching functions in the x and y directions, respectively, and β_x and β_y are the corresponding attenuating PML functions.

A.2 In three dimensions with PML

The equation of motion in 3D with Perfectly-Matched-Layers is:

$$\mathbf{M}\ddot{\mathbf{d}}(t) + \mathbf{C}\dot{\mathbf{d}}(t) + \mathbf{K}\mathbf{d}(t) + \mathbf{G}\bar{\mathbf{d}}(t) = \mathbf{f}(t). \tag{4.7}$$

The structure of matrices $\mathbf{M}$, $\mathbf{C}$, $\mathbf{K}$ and $\mathbf{G}$ is:

$$\mathbf{M} = \left[\begin{array}{c|c|c} \mathbf{M}_{\text{REG}} & & \\ \hline & \mathbf{M}_{\mathsf{a}} & \\ \hline & & \mathbf{N}_{\mathsf{a}} \end{array}\right] \tag{A.1a}$$

$$\mathbf{C} = \left[\begin{array}{c|c|c} & & \\ \hline & \mathbf{M}_{\mathsf{b}} & \mathbf{A}_{eu} \\ \hline & \mathbf{A}_{el} & \mathbf{N}_{\mathsf{b}} \end{array}\right] \tag{A.1b}$$

$$\mathbf{K} = \left[\begin{array}{c|c|c} \mathbf{K}_{\text{REG}} & & \\ \hline & \mathbf{M}_{\mathsf{c}} & \mathbf{A}_{pu} \\ \hline & \mathbf{A}_{pl} & \mathbf{N}_{\mathsf{c}} \end{array}\right] \tag{A.1c}$$

$$\mathbf{G} = \left[\begin{array}{c|c|c} & & \\ \hline & \mathbf{M}_{\mathsf{d}} & \mathbf{A}_{wu} \\ \hline & \mathbf{A}_{wl} & \mathbf{N}_{\mathsf{d}} \end{array}\right] \tag{A.11a}$$

The definitions of each block matrix are provided next.

A.2.1 Regular domain

$$\mathbf{M}_{\mathrm{REG}} = \int_{\Omega_{\mathrm{REG}}} \rho \begin{bmatrix} \boldsymbol{\Phi}\boldsymbol{\Phi}^{\intercal} & & \\ & \boldsymbol{\Phi}\boldsymbol{\Phi}^{\intercal} & \\ & & \boldsymbol{\Phi}\boldsymbol{\Phi}^{\intercal} \end{bmatrix} d\mathbf{x} \tag{A.12}$$

$$\mathbf{K}_{\mathrm{REG}} = \int_{\Omega_{\mathrm{REG}}} \begin{bmatrix} \mathbf{K}_{xx} & \mathbf{K}_{xy} & \mathbf{K}_{xz} \\ \mathbf{K}_{yx} & \mathbf{K}_{yy} & \mathbf{K}_{yz} \\ \mathbf{K}_{zx} & \mathbf{K}_{zy} & \mathbf{K}_{zz} \end{bmatrix} d\mathbf{x} \tag{A.13}$$

$$\mathbf{K}_{xx} = (\lambda + 2\mu)\boldsymbol{\Phi}_x\boldsymbol{\Phi}_x^{\intercal} + \mu\left(\boldsymbol{\Phi}_y\boldsymbol{\Phi}_y^{\intercal} + \boldsymbol{\Phi}_z\boldsymbol{\Phi}_z^{\intercal}\right) \tag{A.14a}$$

$$\mathbf{K}_{xy} = \lambda\boldsymbol{\Phi}_x\boldsymbol{\Phi}_y^{\intercal} + \mu\boldsymbol{\Phi}_y\boldsymbol{\Phi}_x^{\intercal} \tag{A.14b}$$

$$\mathbf{K}_{xz} = \lambda\boldsymbol{\Phi}_x\boldsymbol{\Phi}_z^{\intercal} + \mu\boldsymbol{\Phi}_z\boldsymbol{\Phi}_x^{\intercal} \tag{A.14c}$$

$$\mathbf{K}_{yx} = \lambda\boldsymbol{\Phi}_y\boldsymbol{\Phi}_x^{\intercal} + \mu\boldsymbol{\Phi}_x\boldsymbol{\Phi}_y^{\intercal} \tag{A.14d}$$

$$\mathbf{K}_{yy} = (\lambda + 2\mu)\boldsymbol{\Phi}_y\boldsymbol{\Phi}_y^{\intercal} + \mu\left(\boldsymbol{\Phi}_z\boldsymbol{\Phi}_z^{\intercal} + \boldsymbol{\Phi}_x\boldsymbol{\Phi}_x^{\intercal}\right) \tag{A.14e}$$

$$\mathbf{K}_{yz} = \lambda\boldsymbol{\Phi}_y\boldsymbol{\Phi}_z^{\intercal} + \mu\boldsymbol{\Phi}_z\boldsymbol{\Phi}_y^{\intercal} \tag{A.14f}$$

$$\mathbf{K}_{zx} = \lambda\boldsymbol{\Phi}_z\boldsymbol{\Phi}_x^{\intercal} + \mu\boldsymbol{\Phi}_x\boldsymbol{\Phi}_z^{\intercal} \tag{A.14g}$$

$$\mathbf{K}_{zy} = \lambda\boldsymbol{\Phi}_z\boldsymbol{\Phi}_y^{\intercal} + \mu\boldsymbol{\Phi}_y\boldsymbol{\Phi}_z^{\intercal} \tag{A.14h}$$

$$\mathbf{K}_{zz} = (\lambda + 2\mu)\boldsymbol{\Phi}_z\boldsymbol{\Phi}_z^{\intercal} + \mu\left(\boldsymbol{\Phi}_x\boldsymbol{\Phi}_x^{\intercal} + \boldsymbol{\Phi}_y\boldsymbol{\Phi}_y^{\intercal}\right) \tag{A.14i}$$

A.2.2 Perfectly-Matched-Layers (PMLs)

$$\mathbf{M}_{\mathsf{a}} = \mathsf{a}\mathbf{M}_{\mathrm{REG}}, \quad \mathbf{M}_{\mathsf{b}} = \mathsf{b}\mathbf{M}_{\mathrm{REG}}, \quad \mathbf{M}_{\mathsf{c}} = \mathsf{c}\mathbf{M}_{\mathrm{REG}}, \quad \mathbf{M}_{\mathsf{d}} = \mathsf{d}\mathbf{M}_{\mathrm{REG}} \tag{A.15}$$

$$\mathsf{a} = \alpha_x\alpha_y\alpha_z \tag{A.16a}$$

$$\mathsf{b} = \alpha_x\alpha_y\beta_z + \alpha_x\beta_y\alpha_z + \beta_x\alpha_y\alpha_z \tag{A.16b}$$

$$\mathsf{c} = \alpha_x\beta_y\beta_z + \beta_x\alpha_y\beta_z + \beta_x\beta_y\alpha_z \tag{A.16c}$$

$$\mathsf{d} = \beta_x\beta_y\beta_z \tag{A.16d}$$

$$\mathbf{N}_n = \int_{\Omega_{\mathrm{PML}}} n \begin{bmatrix} \boldsymbol{\Phi}\boldsymbol{\Phi}^{\mathsf{T}} & & & & & & \\ & \boldsymbol{\Phi}\boldsymbol{\Phi}^{\mathsf{T}} & & & & & \\ & & \boldsymbol{\Phi}\boldsymbol{\Phi}^{\mathsf{T}} & & & & \\ & & & 2\boldsymbol{\Phi}\boldsymbol{\Phi}^{\mathsf{T}} & & & \\ & & & & 2\boldsymbol{\Phi}\boldsymbol{\Phi}^{\mathsf{T}} & & \\ & & & & & 2\boldsymbol{\Phi}\boldsymbol{\Phi}^{\mathsf{T}} & \end{bmatrix} d\mathbf{x}, \quad n = \mathsf{a}, \mathsf{b}, \mathsf{c}, \mathsf{d} \tag{A.17}$$

$$\mathbf{A}_{nu} = \int_{\Omega_{\mathrm{PML}}} \begin{bmatrix} \gamma^n_{yz}\boldsymbol{\Phi}_x\boldsymbol{\Phi}^{\mathsf{T}} & & & \gamma^n_{zx}\boldsymbol{\Phi}_y\boldsymbol{\Phi}^{\mathsf{T}} & & \gamma^n_{xy}\boldsymbol{\Phi}_z\boldsymbol{\Phi}^{\mathsf{T}} \\ & \gamma^n_{zx}\boldsymbol{\Phi}_y\boldsymbol{\Phi}^{\mathsf{T}} & & \gamma^n_{yz}\boldsymbol{\Phi}_x\boldsymbol{\Phi}^{\mathsf{T}} & \gamma^n_{xy}\boldsymbol{\Phi}_z\boldsymbol{\Phi}^{\mathsf{T}} & \\ & & \gamma^n_{xy}\boldsymbol{\Phi}_z\boldsymbol{\Phi}^{\mathsf{T}} & & \gamma^n_{zx}\boldsymbol{\Phi}_y\boldsymbol{\Phi}^{\mathsf{T}} & \gamma^n_{yz}\boldsymbol{\Phi}_x\boldsymbol{\Phi}^{\mathsf{T}} \end{bmatrix} d\mathbf{x} \tag{A.18}$$

$$n = e, p, w, \quad \gamma^e_{ij} = \alpha_i\alpha_j, \quad \gamma^p_{ij} = \alpha_i\beta_j + \beta_i\alpha_j, \quad \gamma^w_{ij} = \beta_i\beta_j, \quad i, j = x, y, z$$

$$\mathbf{A}_{nl} = \int_{\Omega_{\mathrm{PML}}} \begin{bmatrix} \mathbf{A}_{x1} & \mathbf{A}_{y1} & \mathbf{A}_{z1} \\ \mathbf{A}_{x2} & \mathbf{A}_{y2} & \mathbf{A}_{z2} \\ \mathbf{A}_{x3} & \mathbf{A}_{y3} & \mathbf{A}_{z3} \\ \mathbf{A}_{x4} & \mathbf{A}_{y4} & \\ & \mathbf{A}_{y5} & \mathbf{A}_{z5} \\ \mathbf{A}_{x6} & & \mathbf{A}_{z6} \end{bmatrix} d\mathbf{x} \tag{A.19}$$

$$\mathbf{A}_{x1} = \gamma_{yz}^{n}(\lambda + 2\mu)\mathbf{\Phi}\mathbf{\Phi}_{x}^{\intercal}, \quad \mathbf{A}_{y1} = \gamma_{zx}^{n}\lambda\mathbf{\Phi}\mathbf{\Phi}_{y}^{\intercal}, \quad \mathbf{A}_{z1} = \gamma_{xy}^{n}\lambda\mathbf{\Phi}\mathbf{\Phi}_{z}^{\intercal} \tag{A.20a}$$

$$\mathbf{A}_{x2} = \gamma_{yz}^{n}\lambda\mathbf{\Phi}\mathbf{\Phi}_{x}^{\intercal}, \quad \mathbf{A}_{y2} = \gamma_{zx}^{n}(\lambda + 2\mu)\mathbf{\Phi}\mathbf{\Phi}_{y}^{\intercal}, \quad \mathbf{A}_{z1} = \gamma_{xy}^{n}\lambda\mathbf{\Phi}\mathbf{\Phi}_{z}^{\intercal} \tag{A.20b}$$

$$\mathbf{A}_{x3} = \gamma_{yz}^{n}\lambda\mathbf{\Phi}\mathbf{\Phi}_{x}^{\intercal}, \quad \mathbf{A}_{y3} = \gamma_{zx}^{n}\lambda\mathbf{\Phi}\mathbf{\Phi}_{y}^{\intercal}, \quad \mathbf{A}_{z3} = \gamma_{xy}^{n}(\lambda + 2\mu)\mathbf{\Phi}\mathbf{\Phi}_{z}^{\intercal} \tag{A.20c}$$

$$\mathbf{A}_{x4} = \gamma_{zx}^{n}2\mu\mathbf{\Phi}\mathbf{\Phi}_{y}^{\intercal}, \quad \mathbf{A}_{y4} = \gamma_{yz}^{n}2\mu\mathbf{\Phi}\mathbf{\Phi}_{x}^{\intercal}, \quad \mathbf{A}_{z5} = \gamma_{zx}^{n}2\mu\mathbf{\Phi}\mathbf{\Phi}_{y}^{\intercal} \tag{A.20d}$$

$$\mathbf{A}_{x6} = \gamma_{xy}^{n}2\mu\mathbf{\Phi}\mathbf{\Phi}_{z}^{\intercal}, \quad \mathbf{A}_{y5} = \gamma_{xy}^{n}2\mu\mathbf{\Phi}\mathbf{\Phi}_{z}^{\intercal}, \quad \mathbf{A}_{z6} = \gamma_{yz}^{n}2\mu\mathbf{\Phi}\mathbf{\Phi}_{x}^{\intercal} \tag{A.20e}$$

$$n = e, p, w, \quad \gamma_{ij}^{e} = \alpha_i\alpha_j, \quad \gamma_{ij}^{p} = \alpha_i\beta_j + \beta_i\alpha_j, \quad \gamma_{ij}^{w} = \beta_i\beta_j, \quad i, j = x, y, z$$

Appendix B

Explicit fourth-order Runge-Kutta method

B.1 In two dimensions with PML

For the equation of motion:

$$\mathbf{M}\ddot{\mathbf{d}}(t) + \mathbf{C}\dot{\mathbf{d}}(t) + \mathbf{K}\mathbf{d}(t) = \mathbf{f}(t), \tag{2.23}$$

we introduce auxiliary variables $\mathbf{x}_1(t)$ and $\mathbf{x}_2(t)$ defined as:

$$\mathbf{x}_1(t) = \mathbf{d}(t), \quad \mathbf{x}_2(t) = \dot{\mathbf{d}}(t). \tag{B.1}$$

Then,

$$\dot{\mathbf{x}}_1(t) = \dot{\mathbf{d}}(t) = \mathbf{x}_2(t) \tag{B.2a}$$

$$\begin{aligned} \dot{\mathbf{x}}_2(t) = \ddot{\mathbf{d}}(t) &= -\mathbf{M}^{-1}\mathbf{K}\mathbf{d}(t) - \mathbf{M}^{-1}\mathbf{C}\dot{\mathbf{d}}(t) + \mathbf{M}^{-1}\mathbf{f}(t) \\ &= -\mathbf{M}^{-1}\mathbf{K}\mathbf{x}_1(t) - \mathbf{M}^{-1}\mathbf{C}\mathbf{x}_2(t) + \mathbf{M}^{-1}\mathbf{f}(t). \end{aligned} \tag{B.2b}$$

We define:

$$\hat{\mathbf{K}} = -\mathbf{M}^{-1}\mathbf{K}, \qquad \hat{\mathbf{C}} = -\mathbf{M}^{-1}\mathbf{C}, \qquad \hat{\mathbf{f}} = \mathbf{M}^{-1}\mathbf{f}$$

Then equations (B.2) are rewritten as:

$$\dot{\mathbf{x}}_1(t) = \mathbf{x}_2(t) \tag{B.3a}$$

$$\dot{\mathbf{x}}_2(t) = \hat{\mathbf{K}}\mathbf{x}_1(t) + \hat{\mathbf{C}}\mathbf{x}_2(t) + \mathbf{M}^{-1}\mathbf{f}(t) \tag{B.3b}$$

or, in matrix form:

$$\begin{bmatrix} \dot{\mathbf{x}}_1(t) \\ \dot{\mathbf{x}}_2(t) \end{bmatrix} = \begin{bmatrix} \mathbf{0} & \mathbf{I} \\ \hat{\mathbf{K}} & \hat{\mathbf{C}} \end{bmatrix} \begin{bmatrix} \mathbf{x}_1(t) \\ \mathbf{x}_2(t) \end{bmatrix} + \begin{bmatrix} \mathbf{0} \\ \hat{\mathbf{f}}(t) \end{bmatrix}. \tag{B.4}$$

The fourth-order Runge-Kutta is implemented as follows. First, for n-th time step, compute:

$$\begin{aligned}
\mathbf{k}_{11} &= \mathbf{x}_2^n \\
\mathbf{k}_{12} &= \hat{\mathbf{K}}\mathbf{x}_1^n + \hat{\mathbf{C}}\mathbf{x}_2^n + \hat{\mathbf{f}}^n \\
\\
\mathbf{k}_{21} &= \mathbf{x}_2^n + \frac{\Delta t}{2}\mathbf{k}_{12} \\
\mathbf{k}_{22} &= \hat{\mathbf{K}}\left(\mathbf{x}_1^n + \frac{\Delta t}{2}\mathbf{k}_{11}\right) + \hat{\mathbf{C}}\mathbf{k}_{21} + \hat{\mathbf{f}}^{n+\frac{1}{2}} \\
\\
\mathbf{k}_{31} &= \mathbf{x}_2^n + \frac{\Delta t}{2}\mathbf{k}_{22} \\
\mathbf{k}_{32} &= \hat{\mathbf{K}}\left(\mathbf{x}_1^n + \frac{\Delta t}{2}\mathbf{k}_{21}\right) + \hat{\mathbf{C}}\mathbf{k}_{31} + \hat{\mathbf{f}}^{n+\frac{1}{2}} \\
\\
\mathbf{k}_{41} &= \mathbf{x}_2^n + \Delta t\mathbf{k}_{32} \\
\mathbf{k}_{42} &= \hat{\mathbf{K}}\left(\mathbf{x}_1^n + \Delta t\mathbf{k}_{31}\right) + \hat{\mathbf{C}}\mathbf{k}_{41} + \hat{\mathbf{f}}^{n+1}.
\end{aligned}$$

Then the solution vectors $\mathbf{x}_1$ and $\mathbf{x}_2$ of the $(n+1)$-th time step are computed as:

$$\begin{aligned}
\mathbf{x}_1^{n+1} &= \frac{\Delta t}{6}\left(\mathbf{k}_{11} + \mathbf{k}_{21} + \mathbf{k}_{31} + \mathbf{k}_{41}\right), \\
\mathbf{x}_2^{n+1} &= \frac{\Delta t}{6}\left(\mathbf{k}_{12} + \mathbf{k}_{22} + \mathbf{k}_{32} + \mathbf{k}_{42}\right).
\end{aligned} \tag{B.5}$$

B.2 In three dimensions with PML

The equation of motion (4.7) can be first integrated in time to yield:

$$\mathbf{M}\ddot{\mathbf{d}}(t) + \mathbf{C}\dot{\mathbf{d}}(t) + \mathbf{K}\mathbf{d}(t) + \mathbf{G}\bar{\mathbf{d}}(t) = \mathbf{0} \tag{B.6}$$

where the *displacement history* $\bar{\mathbf{d}}$ is defined as:

$$\bar{\mathbf{d}}(t) = \int_0^t \mathbf{d}(\tau)\, d\tau. \tag{B.7}$$

We introduce auxiliary variables $\mathbf{x}_0(t)$, $\mathbf{x}_1(t)$ and $\mathbf{x}_2(t)$, defined as:

$$\mathbf{x}_0(t) = \bar{\mathbf{d}}(t), \quad \mathbf{x}_1(t) = \mathbf{d}(t), \quad \mathbf{x}_2(t) = \dot{\mathbf{d}}(t). \tag{B.8}$$

Then,

$$\dot{\mathbf{x}}_0(t) = \dot{\bar{\mathbf{d}}}(t) = \mathbf{d}(t) = \mathbf{x}_1(t) \tag{B.9a}$$

$$\dot{\mathbf{x}}_1(t) = \dot{\mathbf{d}}(t) = \mathbf{x}_2(t) \tag{B.9b}$$

$$\begin{aligned}\dot{\mathbf{x}}_2(t) = \ddot{\mathbf{d}}(t) &= -\mathbf{M}^{-1}\mathbf{K}\mathbf{d}(t) - \mathbf{M}^{-1}\mathbf{C}\dot{\mathbf{d}}(t) + \mathbf{M}^{-1}\mathbf{f}(t) \\ &= -\mathbf{M}^{-1}\mathbf{G}\mathbf{x}_0(t) - \mathbf{M}^{-1}\mathbf{K}\mathbf{x}_1(t) - \mathbf{M}^{-1}\mathbf{C}\mathbf{x}_2(t) + \mathbf{M}^{-1}\mathbf{f}(t).\end{aligned} \tag{B.9c}$$

We define:

$$\hat{\mathbf{G}} = -\mathbf{M}^{-1}\mathbf{G}, \quad \hat{\mathbf{K}} = -\mathbf{M}^{-1}\mathbf{K}, \quad \hat{\mathbf{C}} = -\mathbf{M}^{-1}\mathbf{C}, \quad \hat{\mathbf{f}} = \mathbf{M}^{-1}\mathbf{f}$$

Then equations (B.9) are rewritten as:

$$\dot{\mathbf{x}}_0(t) = \mathbf{x}_1(t) \tag{B.10a}$$

$$\dot{\mathbf{x}}_1(t) = \mathbf{x}_2(t) \tag{B.10b}$$

$$\dot{\mathbf{x}}_2(t) = \hat{\mathbf{G}}\mathbf{x}_0(t)\hat{\mathbf{K}}\mathbf{x}_1(t) + \hat{\mathbf{C}}\mathbf{x}_2(t) + \mathbf{M}^{-1}\mathbf{f}(t) \tag{B.10c}$$

or, in matrix form:

$$\begin{bmatrix} \dot{\mathbf{x}}_0(t) \\ \dot{\mathbf{x}}_1(t) \\ \dot{\mathbf{x}}_2(t) \end{bmatrix} = \begin{bmatrix} \mathbf{0} & \mathbf{I} & \mathbf{0} \\ \mathbf{0} & \mathbf{0} & \mathbf{I} \\ \hat{\mathbf{G}} & \hat{\mathbf{K}} & \hat{\mathbf{C}} \end{bmatrix} \begin{bmatrix} \mathbf{x}_0(t) \\ \mathbf{x}_1(t) \\ \mathbf{x}_2(t) \end{bmatrix} + \begin{bmatrix} \mathbf{0} \\ \mathbf{0} \\ \hat{\mathbf{f}}(t) \end{bmatrix}. \tag{B.11}$$

Then, the fourth-order Runge-Kutta is implemented by computing the following vectors:

$$\begin{aligned}
\mathbf{k}_{10} &= \mathbf{x}_1^n \\
\mathbf{k}_{11} &= \mathbf{x}_2^n \\
\mathbf{k}_{12} &= \hat{\mathbf{G}}\mathbf{x}_0^n + \hat{\mathbf{K}}\mathbf{x}_1^n + \hat{\mathbf{C}}\mathbf{x}_2^n + \hat{\mathbf{f}}^n \\
\\
\mathbf{k}_{20} &= \mathbf{x}_1^n + \frac{\Delta t}{2}\mathbf{k}_{11} \\
\mathbf{k}_{21} &= \mathbf{x}_2^n + \frac{\Delta t}{2}\mathbf{k}_{12} \\
\mathbf{k}_{22} &= \hat{\mathbf{G}}\left(\mathbf{x}_0^n + \frac{\Delta t}{2}\mathbf{k}_{10}\right) + \hat{\mathbf{K}}\mathbf{k}_{20} + \hat{\mathbf{C}}\mathbf{k}_{21} + \hat{\mathbf{f}}^{n+\frac{1}{2}} \\
\\
\mathbf{k}_{30} &= \mathbf{x}_1^n + \frac{\Delta t}{2}\mathbf{k}_{21} \\
\mathbf{k}_{31} &= \mathbf{x}_2^n + \frac{\Delta t}{2}\mathbf{k}_{22} \\
\mathbf{k}_{32} &= \hat{\mathbf{G}}\left(\mathbf{x}_0^n + \frac{\Delta t}{2}\mathbf{k}_{20}\right) + \hat{\mathbf{K}}\mathbf{k}_{30} + \hat{\mathbf{C}}\mathbf{k}_{31} + \hat{\mathbf{f}}^{n+\frac{1}{2}} \\
\\
\mathbf{k}_{40} &= \mathbf{x}_1^n + \Delta t\mathbf{k}_{31} \\
\mathbf{k}_{41} &= \mathbf{x}_2^n + \Delta t\mathbf{k}_{32} \\
\mathbf{k}_{42} &= \hat{\mathbf{G}}\left(\mathbf{x}_0^n + \Delta t\mathbf{k}_{30}\right) + \hat{\mathbf{K}}\mathbf{k}_{40} + \hat{\mathbf{C}}\mathbf{k}_{41} + \hat{\mathbf{f}}^n
\end{aligned}$$

The solution vectors at the $(n+1)$-th time step are then updated as follows.

$$\begin{aligned}
\mathbf{x}_0^{n+1} &= \mathbf{x}_0^n + \frac{\Delta t}{6}\left(\mathbf{k}_{10} + \mathbf{k}_{20} + \mathbf{k}_{30} + \mathbf{k}_{40}\right) \\
\mathbf{x}_1^{n+1} &= \mathbf{x}_1^n + \frac{\Delta t}{6}\left(\mathbf{k}_{11} + \mathbf{k}_{21} + \mathbf{k}_{31} + \mathbf{k}_{41}\right) \\
\mathbf{x}_2^{n+1} &= \mathbf{x}_2^n + \frac{\Delta t}{6}\left(\mathbf{k}_{12} + \mathbf{k}_{22} + \mathbf{k}_{32} + \mathbf{k}_{42}\right).
\end{aligned} \tag{B.12}$$

Bibliography

[1] E. Amitt, D. Givoli, and E. Turkel. Time reversal for crack identification. *Computational Mechanics*, 54(2):443–459, 2014.

[2] B. Anderson, M. Griffa, C. Larmat, T. Ulrich, and P. Johnson. Time reversal. *Acoustics Today*, 4(1):5–16, 2008.

[3] B. Anderson, R. Guyer, T. Ulrich, and P. Johnson. Time reversal of continuous-wave, steady-state signals in elastic media. *Applied Physics Letters*, 94(11):111908, 2009.

[4] S. Balay, S. Abhyankar, M. Adams, J. Brown, P. Brune, K. Buschelman, L. Dalcin, V. Eijkhout, W. Gropp, D. Kaushik, M. Knepley, L. McInnes, K. Rupp, B. Smith, S. Zampini, H. Zhang, and H. Zhang. PETSc users manual. Technical Report ANL-95/11 - Revision 3.7, Argonne National Laboratory, 2016.

[5] S. Balay, S. Abhyankar, M. Adams, J. Brown, P. Brune, K. Buschelman, L. Dalcin, V. Eijkhout, W. Gropp, D. Kaushik, M. Knepley, L. McInnes, K. Rupp, B. Smith, S. Zampini, H. Zhang, and H. Zhang. PETSc Web page. `http://www.mcs.anl.gov/petsc`, 2016.

[6] S. Balay, W. Gropp, L. McInnes, and B. Smith. Efficient management of parallelism in object oriented numerical software libraries. In E. Arge A.

M. Bruaset H. P. Langtangen, editor, *Modern Software Tools in Scientific Computing*, pages 163–202. Birkhäuser Press, 1997.

[7] A. Bateman Manuscript Project, Erdélyi and H. Bateman. *Tables of Integral Transforms: Based in Part on Notes Left by Harry Bateman Compiled by the Staff of the Bateman Manuscript Project*. McGraw-Hill, 1954.

[8] J-P. Bérenger. A perfectly matched layer for the absorption of electromagnetic waves. *Journal of computational physics*, 114(2):185–200, 1994.

[9] I. Beresnev, W. Gaul, and R. Vigil. Direct pore-level observation of permeability increase in two-phase flow by shaking. *Geophysical Research Letters*, 38(20), 2011.

[10] I. Beresnev and P. Johnson. Elastic-wave stimulation of oil production: A review of methods results. *Geophysics*, 59(6):1000–1017, 1994.

[11] M. Braun and M. Golubitsky. *Differential equations their applications*, volume 4. Springer, 1983.

[12] F. Brezzi. A survey of mixed finite element methods. In *Finite elements*, pages 34–49. Springer, 1988.

[13] D. Cassereau and M. Fink. Time-reversal of ultrasonic fields. iii. theory of the closed time-reversal cavity. *IEEE transactions on ultrasonics, ferroelectrics, frequency control*, 39(5):579–592, 1992.

[14] D. Cassereau and M. Fink. Focusing with plane time-reversal mirrors: An efficient alternative to closed cavities. *The Journal of the Acoustical Society of America*, 94(4):2373–2386, 1993.

[15] D. Cassereau and D. Guyomar. Reflection of an impulse spherical wave at a plane interface separating two fluids. *The Journal of the Acoustical Society of America*, 92(3):1706–1720, 1992.

[16] S. Chapman. *Fortran for scientist engineers*. McGraw-Hill, 2008.

[17] J. de Rosny and M. Fink. Focusing properties of near-field time reversal. *Physical Review A*, 76(6):065801, 2007.

[18] C. Draeger and M. Fink. One-channel time reversal of elastic waves in a chaotic 2D-silicon cavity. *Physical Review Letters*, 79(3):407, 1997.

[19] A. Fannjiang. On time reversal mirrors. *Inverse Problems*, 25(9):095010, 2009.

[20] S. Farlow. *Partial differential equations for scientists engineers*. Courier Corporation, 1993.

[21] A. Fathi, L.F. Kallivokas, and B. Poursartip. Full-waveform inversion in three-dimensional PML-truncated elastic media. *Computer Methods in Applied Mechanics and Engineering*, 296:39 – 72, 2015.

[22] A. Fathi, B. Poursartip, K. H. Stokoe II, and L. F. Kallivokas. Three-dimensional P- and S-wave velocity profiling of geotechnical sites using

full-waveform inversion driven by field data. *Soil Dynamics and Earthquake Engineering*, 87:63 – 81, 2016.

[23] A. Fathi, B. Poursartip, and L. Kallivokas. Time-domain hybrid formulations for wave simulations in three-dimensional PML-truncated heterogeneous media. *International Journal for Numerical Methods in Engineering*, 101(3):165–198, 2015.

[24] M. Fink. Time reversal of ultrasonic fields. i. basic principles. *IEEE transactions on ultrasonics, ferroelectrics, frequency control*, 39(5):555–566, 1992.

[25] M. Fink. Time-reversed acoustics. *Scientific American*, 281(5):91–97, 1999.

[26] M. Fink, C. Prada, F. Wu, and D. Cassereau. Self focusing with time reversal mirror in inhomogeneous media. In *Proc. IEEE Ultrason. Symp*, volume 2, pages 681–686, 1989.

[27] H. Goh, S. Koo, and L. Kallivokas. Resolution control in half-space time-reversal wave focusing. The 13th International Conference on Mathematical and Numerical Aspects of Wave Propagation, Twin Cities, MN, May 2017.

[28] M. Greenberg. *Applications of Green's functions in science engineering*. Courier Dover Publications, 2015.

[29] C. Jeong and L. Kallivokas. An inverse-source problem for maximization of pore-fluid oscillation within poroelastic formations. *Inverse Problems in Science Engineering*, 25(6):832–863, 2017.

[30] C. Jeong, L. Kallivokas, S. Kucukcoban, W. Deng, and A. Fathi. Maximization of wave motion within a hydrocarbon reservoir for wave-based enhanced oil recovery. *Journal of Petroleum Science Engineering*, 129:205–220, 2015.

[31] P. Karve, A. Fathi, B. Poursartip, and L. Kallivokas. Source parameter inversion for wave energy focusing to a target inclusion embedded in a three-dimensional heterogeneous halfspace. *International Journal for Numerical Analytical Methods in Geomechanics*, 2016.

[32] P. Karve and L. Kallivokas. Wave energy focusing to subsurface poroelastic formations to promote oil mobilization. *Geophysical Journal International*, 202(1):119–141, 2015.

[33] P. Karve, S. Kucukcoban, and L. Kallivokas. On an inverse source problem for enhanced oil recovery by wave motion maximization in reservoirs. *Computational Geosciences*, 19(1):233–256, 2015.

[34] P. M. Karve. *Inverse source problems for focusing wave energy to targeted subsurface formations: theory and numerical experiments*. Doctoral dissertation, The University of Texas at Austin, 2016.

[35] P. M. Karve, L. F. Kallivokas, and L. Manuel. A framework for assessing the uncertainty in wave energy delivery to targeted subsurface formations. *Journal of applied geophysics*, 125:26–36, February 2016.

[36] S. Koo and L. Kallivokas. Wave energy delivery to multiple subsurface targets using time-reversal method. The 13th International Conference on Mathematical and Numerical Aspects of Wave Propagation, Twin Cities, MN, May 2017.

[37] S. Koo, P. Karve, and L. Kallivokas. A comparison of time-reversal inverse-source methods for the optimal delivery of wave energy to subsurface targets. *Wave Motion*, 67:121–140, 2016.

[38] D. Kopriva. *Implementing spectral methods for partial differential equations: Algorithms for scientists engineers*. Springer Science & Business Media, 2009.

[39] S. Kucukcoban and L. Kallivokas. Mixed perfectly-matched-layers for direct transient analysis in 2D elastic heterogeneous media. *Computer Methods in Applied Mechanics Engineering*, 200(1):57–76, 2011.

[40] S. Kucukcoban and L. Kallivokas. A symmetric hybrid formulation for transient wave simulations in pml-truncated heterogeneous media. *Wave Motion*, 50(1):57–79, 2013.

[41] P. L'ecuyer. Efficient portable combined random number generators. *Communications of the ACM*, 31(6):742–751, 1988.

[42] J. Maynard, E. Williams, and Y. Lee. Nearfield acoustic holography: I. theory of generalized holography the development of nah. *The Journal of the Acoustical Society of America*, 78(4):1395–1413, 1985.

[43] T. Myint-U and L. Debnath. *Linear partial differential equations for scientists engineers*. Springer Science & Business Media, 2007.

[44] P. Norville and W. Scott Jr. Time-reversal focusing of elastic surface waves. *The Journal of the Acoustical Society of America*, 118(2):735–744, 2005.

[45] A. Parvulescu and C. Clay. Reproducibility of signal transmissions in the ocean. *Radio Electronic Engineer*, 29(4):223–228, 1965.

[46] B. Poursartip. *Topographic amplification of seismic motion*. Doctoral dissertation, The University of Texas at Austin, 2017.

[47] B. Poursartip, A. Fathi, and L. F. Kallivokas. Seismic wave amplification by topographic features: A parametric study. *Soil Dynamics and Earthquake Engineering*, 92:503 – 527, 2017.

[48] B. Poursartip and L. F. Kallivokas. An Integrated Approach for the Large-Scale Simulation of Sedimentary Basins to Study Seismic Wave Amplification. In *AGU Fall Meeting Abstracts*, Decemeber 2015.

[49] B. Poursartip and V. Lotfi. Modal analysis of concrete arch dams in time domain including dam-reservoir interaction. In *The 14th world conference on Earthquake Engineering*, pages 12–17, October 2008.

[50] S. Pride, E. Flekkøy, and O. Aursjø. Seismic stimulation for enhanced oil recovery. *Geophysics*, 73(5):O23–O35, 2008.

[51] P. Roberts, I. Esipov, and E. Majer. Elastic wave stimulation of oil reservoirs: Promising eor technology? *The Leading Edge*, 22(5):448–453, 2003.

[52] A. Sutin, J. TenCate, and P. Johnson. Single-channel time reversal in elastic solids. *The Journal of the Acoustical Society of America*, 116(5):2779–2784, 2004.

[53] A. Ugural and S. Fenster. *Advanced strength applied elasticity*. Pearson Education, 2003.

[54] B. Wichmann and I. Hill. Algorithm as 183: An efficient portable pseudo-random number generator. *Journal of the Royal Statistical Society. Series C (Applied Statistics)*, 31(2):188–190, 1982.

[55] L. Wilcox, G. Stadler, C. Burstedde, and O. Ghattas. A high-order discontinuous galerkin method for wave propagation through coupled elastic–acoustic media. *Journal of Computational Physics*, 229(24):9373–9396, 2010.

[56] F. Wu, J-L. Thomas, and M. Fink. Time reversal of ultrasonic fields. il. experimental results. *IEEE transactions on ultrasonics, ferroelectrics, frequency control*, 39(5):567–578, 1992.

[57] A. Yon, M. Tanter, and M. Fink. Sound focusing in rooms: The time-reversal approach. *The Journal of the Acoustical Society of America*, 113(3):1533–1543, 2003.

Vita

Seungbum Koo entered Seoul National University in 2003. He enlisted in the Republic of Korea Marine Corps in 2004 and served in the Marine 1st Division for two years. After he completed his military service, he returned to the Seoul National University and graduated in 2009 with a Bachelor of Science degree in Civil Engineering *cum laude*. After his graduation, he worked at the Samsung Construction and Trading Corporation, and the United Nations Global Compact for a few months as an intern. He started graduate studies at the University of California, Berkeley in 2009. He received a Master of Science degree in Civil and Environmental Engineering in the Spring 2010 from the University of California at Berkeley, and in August 2010 joined the doctoral program in the Department of Civil, Architectural and Environmental Engineering of The University of Texas at Austin.

Permanent address: seungbum.koo@utexas.edu

This dissertation was typeset with LaTeX[†] by the author.

[†]LaTeX is a document preparation system developed by Leslie Lamport as a special version of Donald Knuth's TeX Program.